Doctoral Thesis

Spatiotemporal patterns and correlations in active matter featuring alignment interactions

（配向相互作用を持つアクティブマターにおける時空パターンと相関）

Yutaka Kinoshita

2024 （令和６年）

Abstract

The collective motion of active matter, in which individual constituent elements continuously inject energy into the system, has garnered significant attention over the past few decades. Active matter constitutes a class of nonequilibrium systems exhibiting unique dynamical behaviors that are absent in equilibrium systems. A unified understanding of the mechanisms governing these dynamics is critical for unraveling pattern formations and fluctuation properties in active matter. This thesis focuses on active matter systems where constituents align their directions of motion via mutual interactions, analyzing two representative cases: the pattern formation in active nematic liquid crystals under external fields and the fluctuation properties of active solids featuring alignment interactions. The key studies are summarized as follows:

Active nematics: Active nematics are nematic liquid crystals where each molecule creates hydrodynamic stress along its alignment axis. We begin with an overview of active nematic liquid crystals, including experimental systems such as microtubule-kinesin suspensions, bacterial colonies, and cellular tissues. We introduce the theoretical framework based on extensions of equations for passive nematic liquid crystals, incorporating an activity term. We review key phenomena such as chaotic active turbulence, the characteristic dynamics of topological defects, and the influence of external controls on these behaviors. We numerically investigate the influence of an electric field on the flow patterns and defect dynamics of two-dimensional active nematic liquid crystals (Chap. 2). Our findings show that field-induced reorientation of the director leads to three distinct regimes: (1) active turbulence with chaotic defect motion, (2) a laning state, stripe-like alternating laminar flows, and (3) a uniformly aligned state without flow. The boundary between (2) and (3) is estimated with linear stability analysis of the uniform state. The average flow speed and anisotropy reach their peaks at the laning state that appears in intermediate field strength. Localized vortices are created and disappear leading to periodic oscillation of the states between the active turbulence and laning state in the intermediate regime. In this regime, an undulation instability of the lanes forms localized vortices inside them. They collapse to create two pairs of topological defects, which recombine and annihilate to restore the laning state. Next, we explore the influence of random fields on two-dimensional active nematic liquid crystals (Chap. 3). In biological systems, internal or external cellular environments often contain structural heterogeneities that disrupt the alignment of liquid crystals. We model these effects by a quenched random field imposed on the nematic liquid crystals. Our simulations show that the system undergoes a transition from the active turbulence to a frozen state in which the alignment pattern is arrested with a strong random field. In this frozen state, the nematic director locally aligns with the random field. We found short-range orientational correlations similar to random passive nematics, while the flow velocity retains long-range correlations that decay logarithmically reflecting the form of the Green function of the Stokes equation. This phenomenon is independent of the type of active stress (extensile or contractile). The coexistence of local order and global flow is a novel feature that characterizes active nematics with quenched randomness.

Active solids: Active matter at high density often exhibits solid states that have attracted attention in recent years. We focus on active solids, elastically deformable materials composed of self-propelled particles. The self-driving of each component causes non-equilibrium fluctuations. A coupling between the orientation of each component and its velocity induces drastic changes in the nature of collective motion. An experimental realization of such systems is a network of HexBug® robots connected by springs. In this system, the alignment of the robots causes the migration of the solid. On the other hand, simulations show that the direction of self-propulsion becomes random when the rotational noise is large. The static properties of this system have been investigated in both the random and migrating states, and it is shown that the direction of self-propulsion exhibits a quasi-long-range order in the migrating state. However, the dynamic properties of this state have not been investigated. We then examine fluctuation spectra in active solids featuring polar alignment interactions (Chap. 4). The study reveals unique excitation modes arising from the coupling between activity and alignment interactions. They can be obtained by solving the linearized equations for fluctuations from a noise-free state. The fluctuations reflect the anisotropy of the elastic interaction and the direction of migration. The peaks shift to higher wavenumber and frequency as the coupling or the self-propulsion speed increases. The results of the numerical simulation and the analytical solution are in good agreement. These nonequilibrium fluctuations differ fundamentally from equilibrium fluctuations, as evidenced by the rate of entropy production that quantifies the rate of energy dissipation or irreversibility associated with the system's deviation from equilibrium, based on the probabilities of forward and reverse transitions. It is known that the rate of entropy production in a steady state is proportional to the off-diagonal components of the fluctuation spectrum matrix. In this system, only the coupling between fluctuations perpendicular to the migration direction and the self-propelling angle contributes to it.

By investigating systems where activity and alignment interactions coexist, this work uncovers qualitatively distinct dynamics, including novel pattern formations and characteristics of non-equilibrium fluctuations. These findings lay the groundwork for future studies on active matter systems with alignment interactions, offering potential applications in understanding biological collectives and designing advanced biomaterials.

Contents

List of Conventions

$\boldsymbol{A}$	vector or rank-1 tensor	(i th component is A_i)
$\underline{\boldsymbol{A}}$	rank-2 tensor	(i and j th component is A_{ij})
$\boldsymbol{A} \cdot \boldsymbol{B} = A_i B_i$	inner product	
$\underline{\boldsymbol{A}} : \underline{\boldsymbol{B}} = A_{ij} B_{ji}$	tensor contraction	
$\mathrm{Tr}(\underline{\boldsymbol{A}}) = A_{ii}$	trace	

Chapter 1

Introduction

1.1 Active matter

1.1.1 Basic concept of active matter

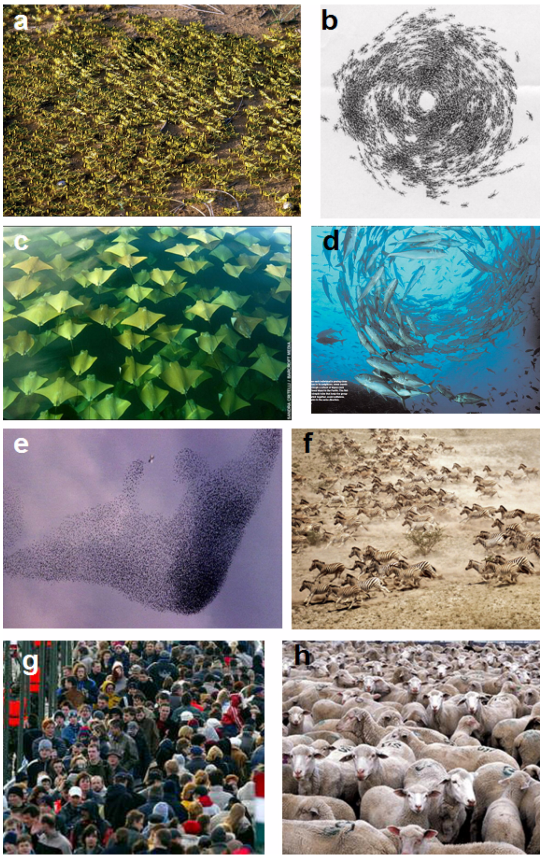

Figure 1.1: A gallery of images related to collective behavior. Among others, it illustrates the possible existence of very general behavioral patterns. (a) Wingless Locusts marching in the field. (b) A rotating colony of army ants. (c) A three-dimensional array of golden rays. (d) Fish are known to produce such vortices. (e) Before roosting, thousands of starlings producing a fascinating aerial display. They are also trying to avoid a predator bird close to the central, finger-like structure. (f) A herd of zebra. (g) People spontaneously ordered into "traffic lanes" as they cross a pedestrian bridge in large numbers. (h) Although sheep are known to move very coherently, just as the corresponding theory predicts, when simply hanging around (no motion), well developed orientational patterns cannot emerge.
The figure and the above caption are reprinted from [1] (T. Vicsek, *et al.*, "Collective motion", Phys. Rep. **517**, 71–140 (2012)), © (2012), with permission from Elsevier.

Active matter refers to systems in which biological or physical components consume energy to move or deform, resulting in unique collective physical and dynamic behaviors [1–5]. This field draws inspiration from biological phenomena (Fig. 1.1), such as bird flocks [6], fish schools [7], cell movements [8–12], and bacterial colony formations [13, 14], aiming to understand their collective dynamics and pattern formation. Recently, active matter, with its wide applications, has attracted significant attention [15]. Due to its nature as a non-equilibrium system, active matter exhibits complex dynamic patterns that cannot be explained by equilibrium thermodynamics or statistical mechanics [16]. For example, vortex structures [17] and true long-range orientational order [18] emerge from interactions among active elements.

Furthermore, individual elements and particles often interact either locally or non-locally with other elements to coordinate their movements. There are many types of interactions, such as short-range interactions like the excluded volume effect and long-range interactions like hydrodynamic interactions. Among these, alignment interactions that change the orientation of self-propulsion of particles are key to collective order and pattern formation. These interactions are crucial in modeling phenomena such as bird flocks [6].

1.1.2 Classification

Active matter can be classified into several classes based on the directionality of self-propulsion and the symmetry of interactions [3]. Firstly, regarding the direction of self-propulsion, particles may move either (i) along their specific directionality towards the head direction or (ii) move randomly in forward and backward directions with equal probability. Secondly, there are different types of interactions that align the orientation of particles: (i) polar interactions where particles align their direction of motion with each other, (ii) nematic interactions where particles align along an axis without polarity, so they orient at an angle of either 0 degrees or 180 degrees from each other, and (iii) no aligning interactions where the direction of self-propulsion is determined individually.

Furthermore, the presence or absence of long-range interactions is also an important factor. For instance, in systems referred to as dry systems [19], only short-range interactions such as excluded volume effects are present. In contrast, in systems known as wet systems [17], hydrodynamic interactions play a significant role. Similarly, as discussed below, elastic interactions are a key factor in active solids [20, 21]. The hydrodynamic and elastic interactions are long-ranged in bulk systems without boundaries. This thesis focuses exclusively on systems with long-range hydrodynamic or elastic interactions.

1.1.3 Dry active matter

Here, I introduce the representative models of dry active matter, Vicsek-style models in two dimensions: Vicsek model, self-propelled-rods, and dry active nematics [19]. All of them have short-range metric interaction, an interaction between particles that depends on the physical distance between them.

Firstly, the Vicsek model [22, 23] is one of the models of matter exhibiting polar motion and polar short-range interactions. The Vicsek model is a minimal framework to study collective motion in systems of self-propelled particles. In this model, particles move at a constant speed in a two-dimensional space, and their orientation aligns with the average direction of their neighbors within a certain radius, subject to noise. In the context of physics, the model is a two-dimensional XY model with particle flow. In terms of the model equations, at each time step t, the position $\boldsymbol{r}_i$ and velocity $v_0\boldsymbol{e}(\theta_i)$ of particle i are updated as follows:

$$\boldsymbol{r}_i(t+\Delta t) = \boldsymbol{r}_i(t) + v_0\boldsymbol{e}(\theta_i)\Delta t, \tag{1.1a}$$

$$\theta_i(t+\Delta t) = \arg\left[\sum_{j\in\mathcal{N}_i} \mathrm{e}^{i\theta_j}\right] + \eta_i(t), \tag{1.1b}$$

where $\mathcal{N}_i$ represents the set of neighbors within a fixed interaction radius r_0 including i itself, and $\eta_i(t)$ is a random noise term uniformly distributed within $[-\eta/2, \eta/2]$. There are four parameters: particle density ρ, interaction radius r_0, particle velocity v_0, and noise intensity η. Here, the velocity must be slow enough for the interaction to occur. By normalizing the interaction radius to 1, two qualitatively important parameters remain: particle density ρ and noise intensity η.

There are two states in this system: an ordered state where the self-propulsion directions of the particles are aligned in a single direction and a random state. Interestingly, the ordered state has a true long-range orientational order of a polar order $P = |\langle \boldsymbol{e}(\theta_i)\rangle|$ [19]. In the two-dimensional XY model with fixed particles, it is known that there is no long-range order due to the spontaneous breaking of continuum symmetry (Mermin–Wagner theorem [24]). Instead, a quasi-long-range order is realized in which the orientation correlation function should decay in a power-law manner. However, in the Vicsek model, the orientation of particles has a true long-range order in which the orientation correlation function remains finite in the long-range limit. Since the ordered phase is a state in which orientation symmetry is broken, the transition between the two states is a discontinuous transition with spontaneous symmetry breaking from a random state to an aligned state [25, 26]. Near the transition point, a two-state coexistence state is realized, where the ordered and disordered states propagate in bands called Vicsek bands. Another notable feature of this system is the anomalous fluctuation of the number of particles. In general, the particle fluctuation $\langle (N - \langle N\rangle)^2\rangle^{\frac{1}{2}}$ behaves in a power-law fashion with respect to the mean value $\langle N\rangle$ where $\langle\cdots\rangle$ is the particle average over a certain region. Let the exponent be α: $\langle (N - \langle N\rangle)^2\rangle^{\frac{1}{2}} \propto \langle N\rangle^{\alpha}$. In the equilibrium system, $\alpha = 0.5$ according to the central limit theorem. Even in the disordered state of the Vicsek model, α takes the same value as the above one. On the other hand, in the ordered state, the exponent becomes $\alpha \sim 0.8$. This larger-than-usual particle number fluctuation is called giant number fluctuation.

Next, self-propelled rods have polar motion and nematic interaction. The time-evolutions of the position $\boldsymbol{r}_i$ and velocity $v_0\boldsymbol{e}(\theta_i)$ of particle i are as follows:

$$\boldsymbol{r}_i(t+\Delta t) = \boldsymbol{r}_i(t) + v_0\boldsymbol{e}(\theta_i)\Delta t, \tag{1.2a}$$

$$\theta_i(t+\Delta t) = \arg\left[\sum_{j\in\mathcal{N}_i} \operatorname{sign}\left[\cos\left(\theta_j - \theta_i\right)\right] \mathrm{e}^{i\theta_j}\right] + \eta_i(t), \tag{1.2b}$$

where the meanings of the variables are the same as the Vicsek ones. The large-scale properties of this system have been reported in the paper by Ginelli *et al.* [27]. Unlike the Vicsek model, this system shows four states as the noise is increased: from small noise (i) homogeneous nematic order, (ii) stable nematic bands, (iii) unstable nematic bands, and (iv) spatially homogeneous disordered. In particular, the nematic order parameter $S = |\langle \exp(i2\theta_i) \rangle|$ takes a non-zero value in the large-system-size limit in the state (i). This suggests that true nematic long-range order appears in the system. When we look at the distribution of polar orientation, we can see that there are two peaks of the same magnitude at the directions of the nematic order $+\theta_0$ and $-\theta_0$, indicating that there is migration of the same scale in the positive and negative directions. Like the Vicsek model, giant number fluctuation is observed with the exponent $\alpha \sim 0.8$.

Finally, dry active nematics have apolar motion and nematic interaction. The time-evolutions of the position $\boldsymbol{r}_i$ and velocity $v_0 \boldsymbol{e}(\theta_i)$ of particle i are as follows:

$$\boldsymbol{r}_i(t + \Delta t) = \boldsymbol{r}_i(t) \pm v_0 \boldsymbol{e}(\theta_i) \Delta t, \tag{1.3a}$$

$$\theta_i(t + \Delta t) = \arg \left[\sum_{j \in \mathcal{N}_i} \mathrm{sign} \left[\cos \left(\theta_j - \theta_i \right) \right] \mathrm{e}^{i\theta_j} \right] + \eta_i(t), \tag{1.3b}$$

where the particles move forward or backward with equal probabilities. The properties have been reported in Ref. [28]. The system has a state transition from an orientationally disordered state to an ordered state at critical noise strength σ_c. Unlike the two systems above, this system does not have polar or nematic long-range order in the aligned state that appears when the noise is small. Instead, it has a quasi-long-range order with respect to the nematic order S which is reminiscent of the Kosterlitz–Thouless transition. Indeed, the nematic order parameter $S(N)$ as a function of the number of particles in this state scales as $S(N) \sim N^{-\zeta}$ where$\zeta \sim 1/16$ at the critical point σ_c, in good agreement with the scaling exponent $\zeta = 1/16$ for the Kosterlitz–Thouless transition. The giant number fluctuation with the exponent $\alpha \sim 0.8$ has also been reported [29].

1.2 Passive nematic liquid crystals

In this section, we overview the theoretical model of passive nematic liquid crystals. Nematic liquid crystals are a material composed of molecules that align their long axes in the same direction on average with disordered positions of the center-of-mass, while still flowing like a liquid. Since we are interested in macro-scale dynamics, we use the continuum model to describe nematic liquid crystals. The physical quantities that need to be considered are the molecular alignment of liquid crystals and the flow velocity. The theoretical model of nematic liquid crystals is well described by a second-rank tensor that represents the orientation and degree of alignment [30]. Many textbooks, such as Refs. [30–33], have been published on the theory of nematic liquid crystals. Most of this subsection is essentially covered in these textbooks. Before going through the detailed theory, some assumptions should be made to clarify our target system.

- Uniaxial molecules, in other words, rod-like molecules are considered.

- Molecular density is significantly high and constant over the system [1] [30, 32].
- The fluid containing the molecules (in other words, under the above condition, the mixture of the molecules and surrounding fluid) is incompressible.

The equations consist of the following two main equations:

1. The dynamic equation for a second-rank tensor that represents molecular alignment
2. The equation of fluid motion (an extended Navier–Stokes equation)

1.2.1 Alignment tensor (Q-tensor)

Consider a small region containing a statistically large number of molecules. The orientation of the i-th molecule within this region is represented by a unit vector $\boldsymbol{a}_i$. If the orientation of the molecule is distinguishable along the rotation axis, $\boldsymbol{a}_i$ is uniquely defined. On the other hand, for molecules without head-tail distinction, $\boldsymbol{a}_i$ can be determined randomly. Now, let the α-axis represent the average orientation of the molecules in the small volume. The degree of alignment of the molecules along the α-axis is described by the order parameter $S = S(\boldsymbol{r})$, which is conveniently defined as follows:

$$S = \frac{d}{d-1}\left(\langle a_{i,\alpha}^2\rangle - \frac{1}{d}\right) \tag{1.4}$$

where $\langle\cdots\rangle$ denotes the local average of molecules and d is the dimension of the vector $\boldsymbol{a}_i$. If the molecules are oriented completely randomly, then $\langle a_1^2\rangle = \langle a_2^2\rangle = \cdots = \langle a_d^2\rangle$ and $\langle a_1^2\rangle + \langle a_2^2\rangle + \cdots + \langle a_d^2\rangle = 1$, leading to $\langle a_\alpha^2\rangle = \frac{1}{d}$ for arbitrary axis and thus $S = 0$. On the other hand, if the molecules are perfectly aligned along the α-axis, then $\langle a_\alpha^2\rangle = 1$, resulting in $S = 1$.

It is possible to handle the degree and the direction of alignment by considering the second-rank tensor $\langle a_i a_j\rangle$ $(i, j = 1, 2, \cdots, d)$. The order parameter defined in Eq. (1.4) can be generalized to the second-order tensor $Q_{ij} = Q_{ij}(\boldsymbol{r})$ called the Q-tensor by combining the scalar order parameter S and the unit vector $\boldsymbol{n}$ called director as the direction of alignment as:

$$Q_{ij} = \frac{d}{d-1}\left(\langle a_i a_j\rangle - \frac{1}{d}\delta_{ij}\right), \tag{1.5}$$

or equivalently,

$$\underline{\boldsymbol{Q}} = S\left(\boldsymbol{n}\otimes\boldsymbol{n} - \frac{\boldsymbol{I}}{d}\right). \tag{1.6}$$

By definition, $\underline{\boldsymbol{Q}}$ is a symmetric tensor ($Q_{ij} = Q_{ji}$) and traceless ($\mathrm{Tr}\,\underline{\boldsymbol{Q}} = 0$).

1.2.2 Phenomenological free energy

A phenomenological free energy F is defined as follows:

$$F = \int \left(f_{\mathrm{LdG}}(\mathbf{Q}) + f_{\mathrm{elastic}}(\nabla\mathbf{Q})\right)\, dV, \tag{1.7}$$

---

[1] There are two important reference densities: $\nu_1 = 1/L^3$, below which the molecules are able to rotate freely without interference by other ones and $\nu_2 = 1/(bL^2)$, below which the effect of excluded volume is shown to be in the order of ν_2. Here L is the length and b is the diameter of a molecule. We consider the situation such that the density of molecules ν satisfies $\nu_1 \ll \nu_2 \lesssim \nu$.

with respect to $\underline{\boldsymbol{Q}}$. The homogeneous part $f_{\mathrm{LdG}}(\mathbf{Q})$ called the Landau–de Gennes free energy is the power series expansion of free energy [30],

$$f_{\mathrm{LdG}}(\underline{\boldsymbol{Q}}) = \frac{A}{2}\underline{\boldsymbol{Q}} : \underline{\boldsymbol{Q}} + \frac{B}{3}\mathrm{Tr}(\underline{\boldsymbol{Q}} \cdot \underline{\boldsymbol{Q}} \cdot \underline{\boldsymbol{Q}}) + \frac{C}{4}\left(\underline{\boldsymbol{Q}} : \underline{\boldsymbol{Q}}\right)^2 . \tag{1.8}$$

Here, A is generally an increasing function of the temperature, approximated as $A = a(T - T_0)$ with a constant $a > 0$ in the vicinity of the transition point T_0. The system exhibits a continuous transition when $B = 0$ and a first-order transition when $B < 0$. C is always positive to ensure thermodynamic stability.

The contribution from the spatial disorder of orientation can be written using the director as follows

$$f_d = \frac{1}{2}K_1\left(\nabla \cdot \boldsymbol{n}\right)^2 + \frac{1}{2}K_2\left(\boldsymbol{n} \cdot (\nabla \times \boldsymbol{n})\right)^2 + \frac{1}{2}K_3\left(\boldsymbol{n} \times (\nabla \times \boldsymbol{n})\right)^2 . \tag{1.9}$$

These terms follow naturally from the symmetry of nematic liquid crystals. Here, the first term represents splay deformation, the second one is twist deformation, and the third one is bend deformation. This elastic distortion energy is referred to as Frank elastic energy.

On the other hand, for the deformation energy using the Q-tensor, only the following two terms remain from the symmetry:

$$f_{\mathrm{elastic}} = \frac{L_1}{2}\frac{\partial Q_{jk}}{\partial x_i}\frac{\partial Q_{jk}}{\partial x_i} + \frac{L_2}{2}\frac{\partial Q_{ik}}{\partial x_i}\frac{\partial Q_{kj}}{\partial x_j} . \tag{1.10}$$

By substituting the definition of $\mathbf{Q}$, Eq. (1.6), into this expression, we obtain:

$$\begin{aligned} f = {} & \frac{1}{3}\left(L_1 + \frac{1}{6}L_2\right)(\nabla S)^2 + \frac{1}{6}L_2\left(\boldsymbol{n} \cdot \nabla S\right)^2 \\ & + S^2\left\{\left(L_1 + \frac{1}{2}L_2\right)(\nabla \cdot \boldsymbol{n})^2 + L_1\left(\boldsymbol{n} \cdot \nabla \times \boldsymbol{n}\right)^2 + \left(L_1 + \frac{1}{2}L_2\right)\left(\boldsymbol{n} \times \nabla \times \boldsymbol{n}\right)^2\right\} \\ & + \frac{2}{3}L_2 S\left(\nabla \cdot \boldsymbol{n}\right)\left(\boldsymbol{n} \cdot \nabla S\right) + \frac{1}{3}L_2 S\left(\boldsymbol{n} \times \nabla \times \boldsymbol{n}\right) \cdot \nabla S . \end{aligned} \tag{1.11}$$

Here, assuming that the spatial variation of the scalar order parameter S is small, and dropping the term involving the derivative of it, we obtain the following relationship from the comparison of Eq. (1.9) and Eq. (1.10)

$$\begin{aligned} K_1 &= K_3 = 2S^2\left(L_1 + \frac{1}{2}L_2\right), \\ K_2 &= 2S^2 L_1 . \end{aligned} \tag{1.12}$$

For simplicity, assuming $K_1 = K_2 = K_3$ called one-constant approximation, we get $L_2 = 0$. The free energy for distortion then becomes:

$$f_{\mathrm{elastic}} = \frac{L_1}{2}\frac{\partial Q_{jk}}{\partial x_i}\frac{\partial Q_{jk}}{\partial x_i} \equiv \frac{L_1}{2}\left(\nabla \underline{\boldsymbol{Q}}\right)^2 . \tag{1.13}$$

1.2.3 Time-evolution equations

The evolution of the Q-tensor is given by the following equation:

$$\frac{\partial \underline{\boldsymbol{Q}}}{\partial t} + \boldsymbol{v} \cdot \boldsymbol{\nabla} \underline{\boldsymbol{Q}} = \lambda S \underline{\boldsymbol{u}} + \underline{\boldsymbol{Q}} \cdot \underline{\boldsymbol{\omega}} - \underline{\boldsymbol{\omega}} \cdot \underline{\boldsymbol{Q}} + \frac{1}{\gamma} \underline{\boldsymbol{H}}, \tag{1.14}$$

where $\boldsymbol{v}$ is the fluid velocity, share rate $\underline{\boldsymbol{u}} = [\boldsymbol{\nabla} \otimes \boldsymbol{v} + (\boldsymbol{\nabla} \otimes \boldsymbol{v})^T]/2$ and vorticity $\underline{\boldsymbol{\omega}} = [\boldsymbol{\nabla} \otimes \boldsymbol{v} - (\boldsymbol{\nabla} \otimes \boldsymbol{v})^T]/2$ are the symmetric and anti-symmetric parts of the velocity gradient tensor, respectively. $\boldsymbol{v} \cdot \boldsymbol{\nabla} \underline{\boldsymbol{Q}}$ is the advection term for the Q-tensor. $\underline{\boldsymbol{Q}} \cdot \underline{\boldsymbol{\omega}} - \underline{\boldsymbol{\omega}} \cdot \underline{\boldsymbol{Q}}$ describes rigid-body rotation of the direction of alignment due to the vorticity $\underline{\boldsymbol{\omega}}$. $\lambda S \underline{\boldsymbol{u}}$ is a coupling term between the shear deformation gradient tensor $\underline{\boldsymbol{u}}$ and the Q-tensor where λ is called the flow-alignment parameter [2] . $|\lambda| < 1$ corresponds to a flow-tumbling regime, where the director continuously tumbles under shear flow. Conversely, $|\lambda| > 1$ corresponds to a flow-aligning regime, where the director remains stationary at a fixed angle relative to the shear flow. $\underline{\boldsymbol{H}} = -\frac{\delta F}{\delta \underline{\boldsymbol{Q}}}$ is the variation of free energy, driving the Q-tensor toward an energetically stable state with the coefficient γ.

The time evolution equation for the flow field $\boldsymbol{v}$ is an extension of the Navier–Stokes equation, adding a stress term due to the Q-tensor:

$$\rho \left(\frac{\partial \boldsymbol{v}}{\partial t} + \boldsymbol{v} \cdot \boldsymbol{\nabla} \boldsymbol{v} \right) = -\boldsymbol{\nabla} p + \nabla \cdot \underline{\boldsymbol{\sigma}}, \ \boldsymbol{\nabla} \cdot \boldsymbol{v} = 0, \tag{1.15}$$

where ρ is the density of the fluid, and p is the pressure. The stress tensor $\underline{\boldsymbol{\sigma}}$ is separated into two parts: $\underline{\boldsymbol{\sigma}} = \underline{\boldsymbol{\sigma}}_{\text{viscosity}} + \underline{\boldsymbol{\sigma}}_{\text{passive}}$. The viscous stress arises from the velocity gradient and is given by $\underline{\boldsymbol{\sigma}}_{\text{viscous}} = 2\eta \underline{\boldsymbol{u}}$ where η is the shear viscosity. The passive stress is related to the alignment tensor $\mathbf{Q}$ and the thermodynamic driving force $\underline{\boldsymbol{H}}$ and given by $\underline{\boldsymbol{\sigma}}_{\text{passive}} = -\lambda S \underline{\boldsymbol{H}} + \underline{\boldsymbol{Q}} \cdot \underline{\boldsymbol{H}} - \underline{\boldsymbol{H}} \cdot \underline{\boldsymbol{Q}}$. The first term of $\underline{\boldsymbol{\sigma}}_{\text{passive}}$ is understood from Onsager's reciprocal theorem, and the latter terms come from the coefficients of $\delta \underline{\boldsymbol{Q}}$ of the variation of the free energy under the law of conservation of angular momentum.

1.2.4 Topological defects

A topological defect is a singularity of the orientational field. When the alignment is restricted to the xy-plane, the alignment vector can be expressed as $\boldsymbol{n}(\boldsymbol{r}) = (\cos\theta, \sin\theta, 0)$ using an angle $\theta(\boldsymbol{r})$. In this case, the winding number s of the alignment is defined as the line integral of the orientation angle along a closed loop C around the singularity, as follows:

$$\oint_C \mathrm{d}\boldsymbol{r} \theta\,(\boldsymbol{r}) = 2\pi s \tag{1.16}$$

Due to the head-to-tail symmetry of $\boldsymbol{n}$ (where $\boldsymbol{n}$ and $-\boldsymbol{n}$, or θ and $\theta + \pi$ are equivalent), s takes half-integer values ($s = 0, \pm\frac{1}{2}, \pm 1, \pm\frac{3}{2}, \cdots$). The winding number is invariant under continuous deformations of the path that does not cross the singularity and is thus referred to as a topological

---

[2] In general, the coupling between the Q-tensor and the shear deformation gradient is written with the rank-four coefficient C_{ijkl} like $C_{ijlk} u_{kl}$. Various research groups have proposed ways to determine this coefficient [34]. We adopted the simplest model [35] of them all, in which the fourth-order tensor is considered $C_{ijkl} = C \delta_{ik} \delta_{jl}$.

invariant. The higher the winding number around a singularity is, the greater the energy cost for creating a defect becomes. In nematic liquid crystals, defects with $s = \pm 1/2$ which have the lowest elastic energy, are predominant. The $+1/2$ defect has a comet-like shape while the $-1/2$ defect has a star-like shape with three-fold symmetry (Fig. 1.2). A pair of topological defects with winding numbers $\pm\frac{1}{2}$ attract each other to reduce the free energy and annihilate upon collision.

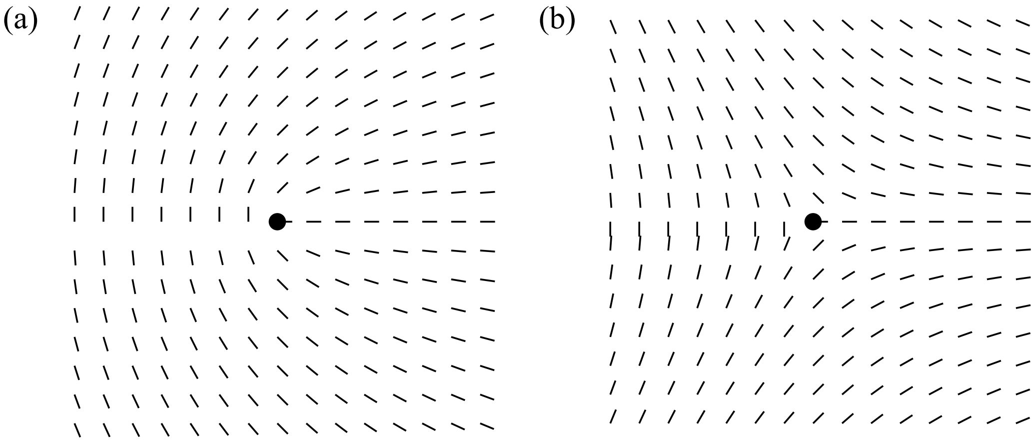

Figure 1.2: Schematic pictures of (a) $s = +1/2$ defect and (b) $s = -1/2$ defect, respectively. Black lines show the director field.

1.3 Active nematic liquid crystals

In this section, we briefly go through previous work about active nematic liquid crystals. Hereafter, we will call the suspension of elongated particles that produce hydrodynamic stress along the molecular axis due to their internal activity the active nematics.

1.3.1 Examples of experimental systems

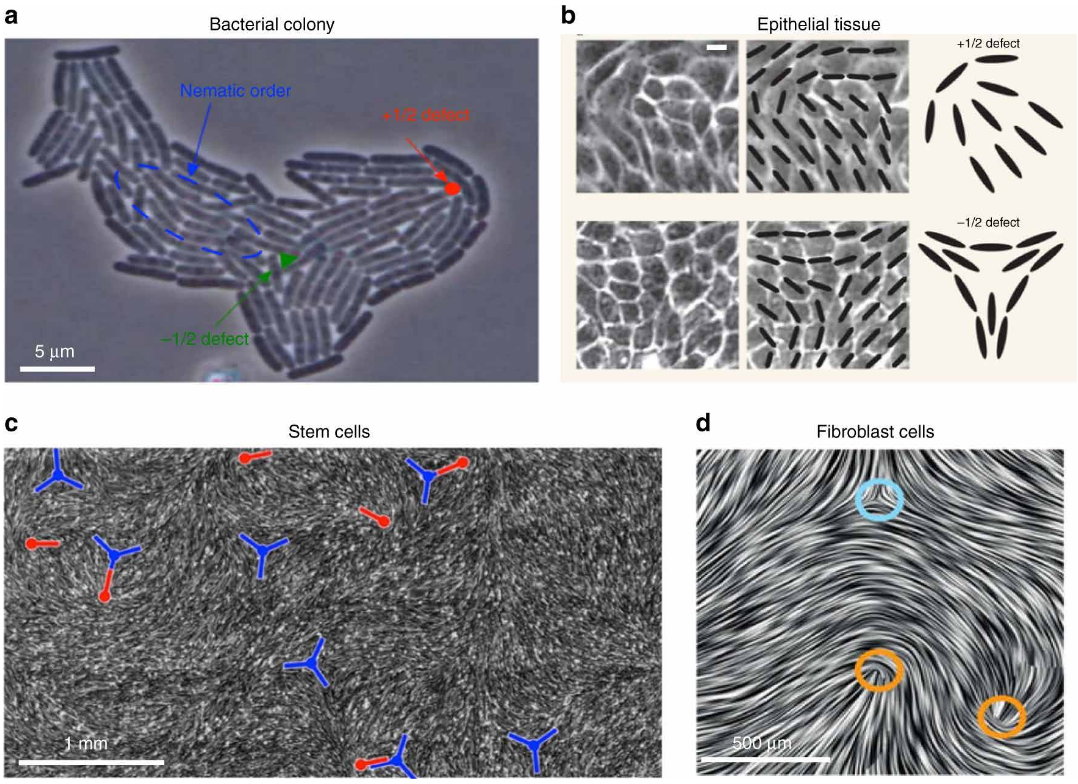

Figure 1.3: Active nematic defects in biological systems. **a** Growing colony of *E. coli* bacteria [36]. The motion of $+1/2$ defects towards the growing interface can lead to shape changes of the colony. **b** Epithelial tissue of Madine-Darby canine kidney (MDCK) cells. Scale bar is 10 µm [8]. Strong correlations between the position of $+1/2$ defects and cell death and extrusion have been reported. **c** Monolayer of neural progenitor stem cells [9]. Cells are depleted from -1/2 defects (blue, trefoil symbols) and accumulate at $+1/2$ ones (red, comet-like symbols). **d** Dense monolayer of mouse fibroblast cells [10] showing $-1/2$ and $+1/2$ topological defects marked by blue and orange circles, respectively.
The figure and caption are reused from [17] (A. Doostmohammadi, *et al.*, "Active nematics", Nat. Commun. **9**, 1–13 (2018)) under Creative Commons CC BY 4.0. Reprinted **a** with permission from [36] (A. Doostmohammadi, *et al.*, "Defect-mediated morphologies in growing cell colonies", Phys. Rev. Lett. **117**, 048102 (2016)) © (2016) by the American Physical Society. Reprinted **b** with permission from [8] (T. B. Saw, *et al.*, "Topological defects in epithelia govern cell death and extrusion", Nature **544**, 212–216 (2017)) © (2017) by Macmillan Publishers Limited, part of Springer Nature. Reprinted **c** with permission from [9] (K. Kawaguchi, *et al.*, "Topological defects control collective dynamics in neural progenitor cell cultures", Nature **545**, 327–331 (2017)) © (2017) by Macmillan Publishers Limited, part of Springer Nature. Reprinted **d** with permission from [10] (G. Duclos, *et al.*, "Topological defects in confined populations of spindle-shaped cells", Nat. Phys. **13**, 58–62 (2017)) © (2016) by Macmillan Publishers Limited, part of Springer Nature.

Before introducing the model equations, explaining experimental systems would be helpful. Examples include bacterial colonies [36], assembly of cells [8], and cytoskeletal filaments [37] (See also Fig. 1.3). The population of *E. coli* that exhibits cell division shows a nematic state, as shown in the area surrounded by the blue line in Fig. 1.3(a). In addition, topological defects with a charge of $+1/2$ and $-1/2$, as indicated by the red and green dots, appear. In this system, cell division is the source of active stress. Figure 1.3(b) represents topological defects in MDCK cells which are an example of extensile active nematic liquid crystals. It is known that the stress around the $+1/2$ defect enhances cell apoptosis and extrusion. In the case of a monolayer of neural progenitor stem cells (Fig. 1.3(c)), an example of two-dimensional active nematic liquid crystals, cell depletion around $-1/2$ defects, and accumulation around $+1/2$ defects have been reported. Figure 1.3(d) shows $+1/2$ defects (orange circles) and a $-1/2$ defect (blue circle) in a dense monolayer of mouse fibroblast cells.

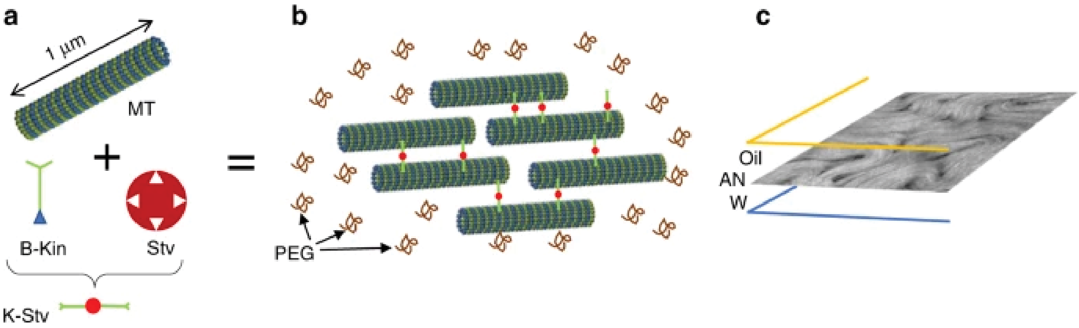

Figure 1.4: An experimental system that has been very important for developing the understanding of active nematics is a mixture of microtubules and two-headed molecular motors. **a** Fluorescently tagged microtubules from polymerised tubulin are brought together by the depleting action of Polyethylene Glycol(PEG), and are cross-linked by clusters of biotinylated kinesin and Streptavidin, resulting in active extensile microtubules bundles in an aqueous suspension (**b**). As the motors walk along the microtubules the bundles extend, are pushed apart, and re-form. **c** The active nematic self-assembles at the water/oil interface and gives rise to active turbulence for as long as there is sufficient ATP to fuel the motors.
The figure is reused, and the caption is adapted from [17] (A. Doostmohammadi, *et al.*, “Active nematics”, Nat. Commun. **9**, 1–13 (2018)) under Creative Commons CC BY 4.0.

Next, I will explain the properties of the microtubule-kinesin suspension. It was reported by Sanchez *et al.* that spontaneous flow occurs in microtubule-kinesin suspension [38], and it has attracted much attention in terms of an example of active nematics. Microtubules are cylindrical macromolecules with a diameter of approximately 25 nm and a length of several micrometers. They have a structure in which protofilaments, which are linear chains of dimers of proteins called α-tubulin and β-tubulin, are arranged in a cylindrical shape. The exposed end of the β-tubulin is called the plus end, and the one of the α-tubulin is called the minus end. Kinesin is one of the motor proteins that can stick to a microtubule and move unidirectionally, mostly from minus to plus ends, on a protofilament by consuming the energy obtained from adenosine triphosphate (ATP) hydrolysis. By tying multiple kinesins with Streptavidin, it is possible to create a cluster that has two docking points. The bundle of microtubules is formed through cross-linking mediated by kinesin motor clusters (Fig. 1.4(a)(b)). If the microtubules are arranged antiparallelly, sliding between the microtubules occurs because the cluster walks on each microtubule, while a pair of parallel microtubules does not show relative motion. The sliding results in the net extension of bundles.

By adding polyethylene glycol (PEG) to the suspension, microtubules are brought closer together due to the depletion force driven by the entropy of conformations of PEGs (Fig. 1.4(b)). The two-dimensional system is realized at the oil-water interface stabilized by surfactants (Fig. 1.4(c)). When a dense suspension is formed, a nematic state appears. The flow pattern is regulated in various ways such as changing the density of each component of suspension.

The emerging pattern is shown in Fig. 1.5(a) and the corresponding simulation result in Fig. 1.5(b). This pattern is called active turbulence or active nematic turbulence and will be explained in Subsec. 1.3.4. The highly curved regions highlighted with yellow lines in Fig. 1.5 are recognized as topological defects. Typically, $\pm 1/2$ defects appear in nematics.

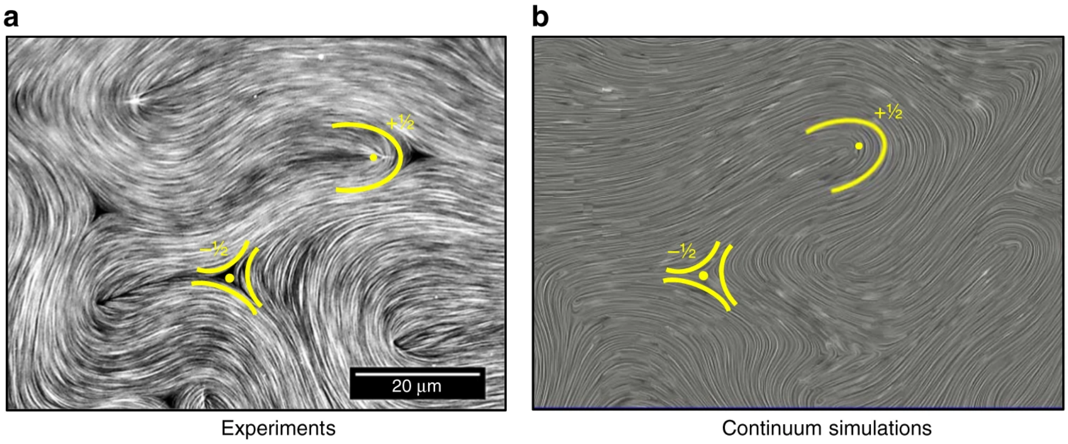

Figure 1.5: Active nematic turbulence. **a** Fluorescence confocal microscopy micrograph of the active nematic in contact with an oil of 0.05 Pa s. **b** Snapshot of the time evolution from solving the continuum equations of motion, showing active turbulence. A comet-like, +1/2, and a trefoil-like, -1/2 defect are highlighted in each case.
The figure and caption are reused from [17] (A. Doostmohammadi, *et al.*, “Active nematics”, Nat. Commun. **9**, 1–13 (2018)) under Creative Commons CC BY 4.0.

1.3.2 Theoretical description

The time evolution equations for active nematic liquid crystals are a form that adds active stress to the equation for passive liquid crystals [17, 39]. There are various types of equations for passive liquid crystals, but in this thesis, we will formulate them using a tensor-type alignment field as introduced in Sec. 1.2. The equations are written as follows:

$$\frac{\partial \underline{\boldsymbol{Q}}}{\partial t} + \boldsymbol{v} \cdot \boldsymbol{\nabla} \underline{\boldsymbol{Q}} = \lambda S \underline{\boldsymbol{u}} + \underline{\boldsymbol{Q}} \cdot \underline{\boldsymbol{\omega}} - \underline{\boldsymbol{\omega}} \cdot \underline{\boldsymbol{Q}} + \frac{1}{\gamma} \underline{\boldsymbol{H}}, \tag{1.17}$$

$$\rho \left(\frac{\partial \boldsymbol{v}}{\partial t} + \boldsymbol{v} \cdot \boldsymbol{\nabla} \boldsymbol{v} \right) = -\boldsymbol{\nabla} p + \nabla \cdot \underline{\boldsymbol{\sigma}}. \tag{1.18}$$

Here, a new term derived from the activity $\underline{\boldsymbol{\sigma}}_{\text{active}}$ is added to the stress tensor: $\underline{\boldsymbol{\sigma}} = \underline{\boldsymbol{\sigma}}_{\text{viscosity}} + \underline{\boldsymbol{\sigma}}_{\text{passive}} + \underline{\boldsymbol{\sigma}}_{\text{active}}$. Active stress is given by the lowest-order term of the Q-tensor that can be considered from symmetry,

$$\underline{\boldsymbol{\sigma}}_{\text{active}} = -\alpha \underline{\boldsymbol{Q}}. \tag{1.19}$$

Here the sign of coefficient α determines the type of active stress. In the case that $\alpha > 0$, referred to as extensile systems, particles generate forces that push the solvent outward along their axis, resulting in the stretching or elongation of the material (Fig. 1.6(a)). This behavior is commonly observed in systems such as microtubule-kinesin networks or human bronchial epithelial cells [40]. Conversely, in the case that $\alpha < 0$, referred to as contractile systems, particles generate forces that pull inward along their axis, causing contraction of the material (Fig. 1.6(b)). This is characteristic of actomyosin networks or fibroblast cells [11].

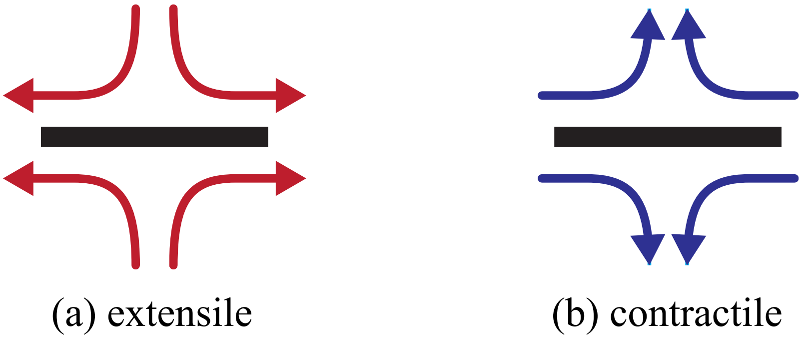

Figure 1.6: Schematic pictures of (a) extensible stress and (b) contractile stress. The black line shows the director field, and the arrows are the directions of the flow field.

1.3.3 Hydrodynamic instabilities and topological defects

While the equilibrium state in the bulk system of passive nematic liquid crystals is a uniformly aligned configuration, the alignment of active nematic liquid crystals is destabilized by active stress. It has been reported that active stress contributes to the destabilization of modes [39, 41]. Thampi *et al.* [42] investigated the destabilization dynamics from the uniformly aligned state. Since this destabilization differs between the extensile and contractile cases, we will first discuss the extensile case. Firstly, the most unstable mode, which is parallel to the director field, grows, and bend deformation arises. The director deformation creates a flow field as can be seen from Eq. (1.19), which in turn sharpens the bend deformation. This banded region of bend deformation is called the “wall” region. Wall generation is intuitively understood as the competition between two effects: destabilization by active stress α and stabilization by Frank elasticity K. In fact, the width of the wall region is scaled by the characteristic length $\sqrt{K/\alpha}$. When the director tilts significantly, at some point the “wall” region splits into a pair of topological defects. The creation of defects is explained by the destabilization of the bend deformation region with respect to the splay deformation. It should be noted that active stress plays an important role in this destabilization, unlike passive nematic liquid crystals. The generated topological defects are transported by elastic forces and flow fields. In particular, $+1/2$ defects self-propels due to their asymmetric nature [43, 44]. When two topological defects with the same magnitude of topological charge and opposite signs approach each other, they disappear by collision. As a result, a uniform region appears again.

In the case of contractile systems, on the other hand, the destabilizing pattern is the opposite of the extensile case. That is, in contrast to the appearance of many bend regions in the extensile case, splay deformation regions appear. There is bend deformation between the different splay deformation regions. As time goes on, the bend deformation becomes more pronounced, and a pair of topological defects is generated at a certain point.

1.3.4 Active turbulence

In the steady state of the bulk system, the process of (i) destabilization of the aligned region, (ii) generation of topological defects, and (iii) the re-alignment of the orientation field, which is explained in the previous section, occurs repeatedly. Consequently, both the orientation field and flow field become chaotic in space and time. This state is called the active turbulence state[3] [17]. We will now look at the characteristics of this state. Here, there is a point to note: the properties of active turbulence differ depending on the system being considered (polar or nematic), and the following explains the properties of wet active nematic liquid crystals in particular.

The characteristics of the flow field are qualitatively different from the properties of turbulent states in inertial fluids. For example, the energy spectrum of the flow $\boldsymbol{v}^2/2$ is different from the Kolmogorov law ($\sim k^{-\frac{5}{3}}$) for inertial fluids. In a microtubule-kinesin suspension, it has been reported that the spectrum is $\sim k^1$, $\sim k^{-1}$, and $\sim k^{-4}$ in the order of wavenumber from low to high [46]. The scaling of $\sim k^{-1}$ and $\sim k^{-4}$ can be derived using the mean field theory [47]. This suggests that, unlike inertial turbulence, there are characteristic length scales in the system. They change depending on the magnitude of the active stress.

Active turbulence is not limited to active nematics; for example, it also appears in polar systems. However, its flow characteristics differ. This is summarized in the review paper Ref. [48].

1.3.5 Effect of boundary walls

It is known that the dynamics of active nematic liquid crystals can be controlled by applying external constraints, such as introducing friction or confining them to a geometric shape. In this section, we will look at systems with confinement in a channel region and with friction.

Confinement in channel geometry

First, in active nematic liquid crystals confined within a two-dimensional channel, several patterns are observed. Here, I specifically focus on extensile system with strong homeotropic anchoring and no-slip boundary[4]. There are two factors that need to be considered for describing the state diagram:(i) competition between the channel width and the characteristic length scale created by the active stress and (ii) the self-motility speed of the +1/2 defects[5] [50]. The model length scale created by active stress can be determined from the balance between the magnitude of active stress α, and the Frank elasticity K, as

$$l_a = \sqrt{\frac{K}{\alpha}}. \tag{1.20}$$

It is important to note that the emergent characteristic lengths in active turbulence states are scaled using l_a [51]. In a channel geometry, four states are roughly observed:(1) uniformly aligned without

---

[3] In three dimensional system, the line-type topological singularities appear instead of point defects, and the system also exhibits chaotic patterns [45].

[4] The patterns are affected by boundary conditions. For example, in Ref. [49], results are shown for the case where one side is homeotropic and the other is planar.

[5] This is a value scaled from the parameters of the model equations, not the actual speed of the defects.

flow (2) unidirectional flow, (3) vortex lattice, and (4) active turbulence, in order from systems with relatively weak active stress [50].

If the activity is weak enough and the speed of the +1/2 defect is slow enough, a uniformly aligned state appears where there is no flow. As the two parameter values become larger, unidirectional flow occurs. With further activity and an increase in self-propulsion speed, the unidirectional flow state transits to a vortex lattice state where vortices can exist at equal intervals within the channel. When the activity further increases, in other words, the length scale decreases, part of the vortex lattice breaks down and the flow becomes turbulent locally. By further increasing the activity, the turbulent-state region becomes dominant, and finally, a uniform active turbulent state is formed. It has been found that the critical exponent for the transition from the vortex lattice to active turbulence belongs to the same universality class as the directed percolation phenomenon.

Friction with substrate

Friction with the substrate causes momentum damping. Theoretically, the effect of momentum damping is represented by adding a drag term proportional to velocity on the left-hand side of the equation of motion of the fluid Eq. (1.18) [52–58]. Here the coefficient is a second-rank tensor and determines the symmetry of the friction. In active nematic liquid crystals with density changes of active particles, the introduction of friction has been reported to cause the appearance of alternating laminar flow called laning flow and vortex lattice states [52, 56, 59].

On the other hand, in active nematic liquid crystals with anisotropic friction, the appearance of a laning state without density change has also been confirmed experimentally [60] and theoretically [53], respectively. Experimentally, two-dimensional active nematic liquid crystals are realized at the interface between solution and oil, stabilized by a surfactant. In this experiment, octyl-cyanobiphenyl (8CB), which exhibits a smectic liquid crystal phase when a magnetic field is applied, is used as the oil. In the absence of a magnetic field, i.e., when 8CB exhibits a random phase, the friction with the oil at the interface is isotropic. However, when a magnetic field is applied, 8CB exhibits a smectic liquid crystal phase, a layered state of two-dimensional nematic order. In this case, the friction with the oil differs in magnitude in the direction perpendicular to the layer and in the direction parallel to the layer. This anisotropic friction causes laning flow.

1.4 Active Solids featuring alignment interaction

In this section, we briefly review previous studies on active solids. Hereafter, I term active solids as elastically deformable states composed of active matter.

1.4.1 An example of experimental system

In this subsection, I introduce the experimental system as an example of active solids featuring alignment interaction.

An example of self-propelled particles with alignment interactions is HexBug Nano®, hereafter simply referred to as HexBug®. HexBug® is a small robot that resembles an insect and is sold by

Spin Master Ltd. The mass of a single unit is about 7g, and the size is about $4.4 \times 1.3 \times 1.9\text{cm}^3$. It has a vibration motor in its body, and when the power is turned on, it generates minute vibrations. It also has six pairs of bent legs on each side of its body, and the vibrations of its body generate forward propulsion. From this, we can see that the HexBug® is an active matter with polar self-propulsion, as introduced in the previous section.

It is also known that the HexBug® has a self-aligning interaction that aligns its self-propulsion in the direction of its own speed [61, 62]. This is presumably because the frictional force between the floor and the HexBug®'s head is non-uniform in the direction from the HexBug®'s head to its tail[6].

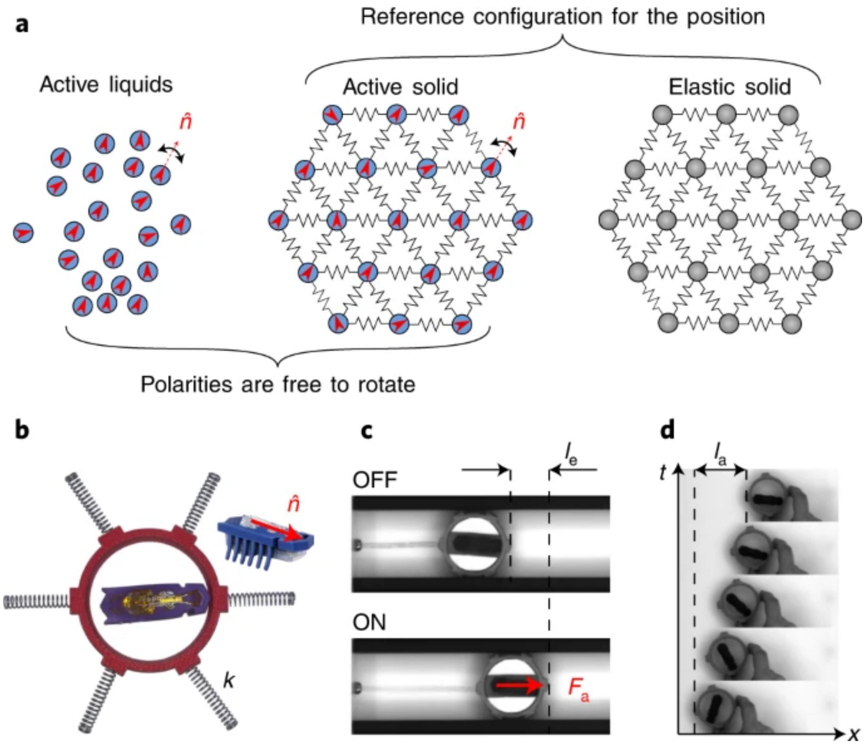

Figure 1.7: **a**, Active solids have positional degrees of freedom with a reference state and a free-to-rotate polarity vector in the direction of the active force. **b**, Active unit: a HexBug® is trapped in a three-dimensionally printed cylinder. **c**, The active component, confined here in a linear track and attached to a spring of stiffness k, produces an active force of amplitude F_0 in the direction of polarity $\hat{\boldsymbol{n}}$ and elongates the spring by length $l_e = F_0/k$. **d**, Mechanical design of the HexBug®–mass distribution and shape of the legs–is responsible for its alignment towards its displacement, here imposed manually, of the cylinder.
The figure is reproduced, and the caption is adapted from [61] (P. Baconnier, *et al.*, "Selective and collective actuation in active solids", Nat. Phys. **18**, 1234–1239 (2022)) with permission from Springer Nature.

Baconnier *et al.* trapped each HexBug® in a cylinder and connected them with springs to create a solid state [61, 63–65], as shown in Fig. 1.7. The cylinders move when pushed by the HexBugs®

---

[6] Let me consider a rod of uniform density ρ and length L. It is moving in the direction of the $+y$-axis with velocity v. Let the coefficient of friction at each position be $\gamma(r)$. Suppose the coordinate of the buttock is $(-L/2, 0)$, and the one of the head is $(L/2, 0)$. At this time, the center of gravity is at the origin. The frictional torque acting on the entire bar is given by

$$N = -\int_{-L/2}^{L/2} dx\rho v\gamma(x)x = -\int_{-L/2}^{0} dx\rho v\gamma(x)x - \int_{0}^{L/2} dx\rho v\gamma(x)x \tag{1.21}$$

If the friction is uniform, the torque is zero. However, if the friction on the $+x$-side is stronger than the other side, the torque is positive and the bar rotates counterclockwise.

inside them. In this case, the cylinder containing the HexBug® is regarded as an active particle, not the HexBug® itself. Different particles interact through the springs.

It has been reported that solids made up of HexBugs® can be in a migrating state, moving in one direction [65]. It has also been studied that spontaneous deformation can occur within solids by pinning the solid and restricting the movement of the center of gravity [61, 63, 64].

1.4.2 Order-disorder transition

The research by Ferrante *et al.* focuses on the systems where self-propelled particles are connected by linear springs [20, 21]. Here are the equations they introduced for the position $\boldsymbol{r}_i$ and orientation θ_i of the i-th particle,

$$\dot{\boldsymbol{r}}_i = v_0 \boldsymbol{n}_i + \alpha \left[\left(\boldsymbol{F}_i + D_r \boldsymbol{\xi}_r \right) \cdot \boldsymbol{n}_i \right] \boldsymbol{n}_i, \tag{1.22}$$

$$\dot{\theta}_i = \beta \left[\left(\boldsymbol{F}_i + D_r \boldsymbol{\xi}_r \right) \cdot \boldsymbol{n}_i^{\perp} \right] + D_\theta \xi_\theta, \tag{1.23}$$

where the i-th particle self-propels in the direction of $\boldsymbol{n}_i$ vector with the speed v_0, and $\boldsymbol{n}_i^{\perp}$ is the unit vector perpendicular to the direction of self-propulsion. The parameters α and β are the inverse of translational and rotational damping coefficients, respectively. The elastic force exerted on the i-th particle is given by $\boldsymbol{F}_i = \sum_{j \in S_i} (-k/l_{ij})(\boldsymbol{r}_{ij} - l_{ij}) \boldsymbol{r}_{ij}/l_{ij}$ with $\boldsymbol{r}_{ij} = \boldsymbol{r}_i - \boldsymbol{r}_j$, a sum of spring forces with natural lengths l_{ij} and spring constants k/l_{ij}. Each set S_i contains all particles interacting with the i-th particle and is fixed throughout the simulation. In these systems, collective motion emerges spontaneously through elastic interactions between particles, without the need for explicit alignment rules. For example, if the particles are initially configurated in a hexagonal lattice with random orientation (Fig. 1.8(A1)), coherent regions gradually develop (Fig. 1.8(A2)), and finally, the globally rotating and translating state appears (Fig. 1.8(A3)). The elastic rod with randomly oriented particles (Fig. 1.8(B1)) also undergoes coherent deformation (Fig. 1.8(B2)), and collectively moving state emerges (Fig. 1.8(B3)). In column C in Fig. 1.8(C1), the particles are initially distributed randomly around two holes. Particles within a radius $r = 1$ are permanently connected by the springs. Over time, coherent regions expand (Fig. 1.8(C2)), leading to the globally collective motion (Fig. 1.8(C3)).

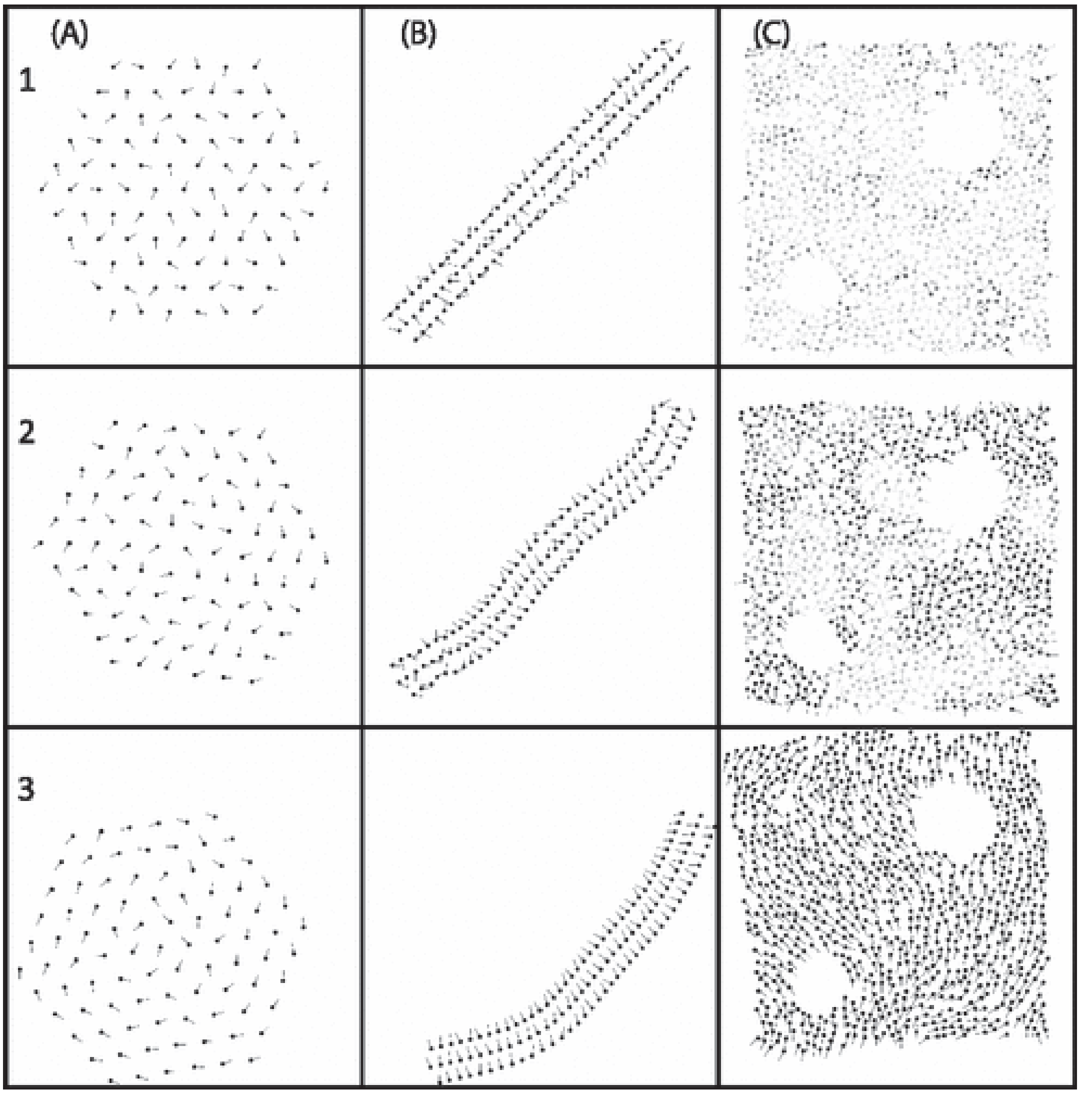

Figure 1.8: Active elastic sheet simulations of Eqs.(1.22) and (1.23). (A) Hexagonal active crystal at $t = 0$ (A1), 240 (A2), and 1700 (A3). (B) Rodlike active crystal at $t = 0$ (B1), 400 (B2), and 1700 (B3). (C) Active solid at same times as column B; darker agents symbolize higher local alignment. The figure and caption are reprinted with permission from [21] (E. Ferrante, *et al.*, "Elasticity-based mechanism for the collective motion of self-propelled particles with springlike interactions: a model system for natural and artificial swarms", Phys. Rev. Lett. **111**, 268302 (2013)) © (2013) by the American Physical Society.

Particularly, system Fig. 1.8(A) exhibits discontinuous transition with respect to the polar order parameter $\psi = \left|\sum_{i=1}^{N} \boldsymbol{n}_i\right|$ as translations or rotational noise is increased.

1.4.3 Long-range order in active solids

Long-range order in active solids has been investigated by Huang *et al.* [66]. They calculated the correlation function of active particle systems where particles are eternally connected with springs in a triangular lattice and investigated the presence or absence of long-range order. They have analyzed the system in general dimensions, but here we focus on two-dimensional crystals. They also compare two cases, i.e. Vicsek-like interactions and self-alignment interactions, but in this thesis, only the self-alignment case is discussed.

We note here that ordinary passive crystals do not have true long-range order in two dimensions. This is a consequence of the Mermin–Wagner theorem. Specifically, correlations of particle positions have quasi-long-range order, while bond orders have long-range order.

The equations they used are as follows,

$$\gamma_p \dot{\boldsymbol{r}}_i(t) = b_p \boldsymbol{n}(\theta_i) + \boldsymbol{F}_i(t) + \gamma_p \sqrt{2D_p}\xi_i(t), \tag{1.24}$$

$$\boldsymbol{F}_i = \sum_{j \text{ n.n. } i} \kappa \left(|\boldsymbol{r}_i - \boldsymbol{r}_j| - a_0\right) \frac{\boldsymbol{r}_i - \boldsymbol{r}_j}{|\boldsymbol{r}_i - \boldsymbol{r}_j|}, \tag{1.25}$$

$$\theta_i(t) = c_p(\boldsymbol{n}(\theta_i) \times \boldsymbol{F}_i) \cdot \hat{z} + \sqrt{2D_p^\theta}\eta_i(t), \tag{1.26}$$

where γ_p is the friction coefficient, and $b_p \boldsymbol{n}(\theta_i)$ is the active force with identical magnitude b_p for all i and director $\boldsymbol{n}(\theta_i)$. In the second equation, κ is the elastic constant, and a_0 is the natural length of the springs. In the third equation, c_p is the alignment strength, and D_p^θ is the rotational diffusion constant. Additionally, a unit vector $\hat{z}$, which is perpendicular to the plane, is temporally introduced for the calculation of the cross product. θ_i is the angle of the vector $\boldsymbol{n}(\theta_i)$ measured from the x-axis, and thus $\boldsymbol{n}(\theta_i) = (\cos\theta_i, \sin\theta_i)$. The summation $\sum_{j \text{ n.n. } i}$ is taken over six nearest neighbors of the i-th particle. The system undergoes a transition between ordered, in other words, migrating, and disordered states with respect to the polar order parameter, similar to the model described in the previous chapter. Although further analysis needs to be conducted, their analysis suggests that this transition is a second-order transition. The important point is that the presence or absence of long-range order changes between these two states. First, in the disordered state, the order of crystalline is found to be similar to that of the passive system. This is confirmed by the fact that the displacement correlations as functions of wavenumber k decay with k^{-2}. It should be noted, however, that, unlike normal passive solids, there is a characteristic fluctuation proportional to k^{-4} in the intermediate range. This is also confirmed for active solids without alignment interaction [67].

On the other hand, in the migrating state, the order becomes short-range in the direction perpendicular to the migrating. This is due to the effect of activity and alignment interactions, which results in a lower critical dimension, under which long-range order cannot emerge, of 4.

1.5 Scope of this work

The basic properties of active nematic liquid crystals are well understood. There are also many papers on the control of pattern formations using boundary conditions such as geometric confinement and friction with the substrate. On the other hand, there is still room for development in the direct control of the alignment of liquid crystals by external fields. This is in contrast to the active research that has been carried out on the application of external fields to passive liquid crystals. Also, active nematics in heterogeneous environments have not attracted much attention yet, despite their potential importance in cellular and subcellular systems. In this study, we will clarify the effects of external fields and the influence of the surrounding heterogeneous obstacles that directly affect the orientation field. In addition, since the history of research on active solids is relatively short compared to that of active fluid systems, there is still space for investigating the basic properties of bulk systems. Therefore, we will focus on active solids that move in one direction and discuss the structure of the internal fluctuations.

1.5.1 Effect of a uniform field on active nematics (Chap. 2)

The content of this subsection is adapted from Ref. [68] (Y. Kinoshita and N. Uchida, "Flow patterns and defect dynamics of active nematic liquid crystals under an electric field", Phys. Rev. E **108**, 014605 (2023)) © (2023) American Physical Society.

The effects of an electric field on active nematics are relatively unexplored. An individual microtubule is reoriented parallel to a DC [69–72] and an AC [73] electric field, which is explained by the negative net charge and dielectric polarizability of microtubules, respectively. However, an experimental study on collective motion of microtubule-kinesin suspensions under an electric field is lacking. Theoretically, a model of an active pump using a Fredericks twisted cell is proposed [74]. A three-dimensional simulation of active nematics under an electric field finds a smooth decrease of the defect density with increased field strength and a transition to a uniformly aligned state [45].

In the present thesis, we numerically study the effects of an electric field on two-dimensional active nematics, focusing on the flow pattern and defect dynamics. We assume alignment of the nematic director along the electric field due to dielectric anisotropy, neglecting electrophoretic or electroosmotic effects. We find that the flow is enhanced in the directions perpendicular to the electric field. The average flow speed and its anisotropy change non-monotonically with the field strength. We obtained a laning state at a larger field strength near the transition to a uniformly aligned state, and periodic oscillations between the laning state and anisotropic turbulence. Topological defects are localized in a single vortex region and show simultaneous creation and recombination of two pairs of defects.

1.5.2 Effect of a random field on active nematics (Chap. 3)

The content of this subsection is adapted from Ref. [75] (Y. Kinoshita and N. Uchida, "Active nematic liquid crystals under a quenched random field", arXiv:2404.08524.).

Recently, attention has extended to couplings of active nematics with non-uniform fields, such as friction by micropatterned surfaces [58], curvature of epithelial tissues [76], spatially varying activity [77, 78] and composition [79]. However, the behavior of active nematics in a randomly heterogeneous environment is an open issue. Cells in tissues are in contact with extracellular matrix that contains fibrous material such as cellulose of collagen. Collagen fibers form anisotropic networks that guide migration of cells [80]. Plant cellulose is also used as a scaffold for in vitro culture of neural stem cells [81]. Microtubules in cells are entangled with other components of cytoskeletal networks such as actins and intermediate filaments, which hinder alignment. The cytoplasm also contains a number of proteins that cyclically change their shapes and generate random hydrodynamic forces. They not only enhance diffusion in the cell [82] but also may contribute to disorientation of active cytoskeletal filaments. To elucidate the effects of heterogeneous anisotropic environments on active nematic flows, we address the effects of quenched random fields in this paper. The effect of a quenched random field on nematic liquid crystals has been studied in a model of nematic elastomers [83]. The numerical study showed that the orientational correlation function decays exponentially as a function of the distance and that the correlation length also decays exponentially with the disorder strength. Recently, the effects of a random field on dry and wet active nematics have been addressed in Refs. [84, 85]. In both cases, the quenched disorder slows the dynamics of topological defects. The orientational correlation follows a crossover from algebraic to exponential decay for dry active nematics, while a slow coarsening behavior is observed for wet active nematics. However, flow property in active nematics with quenched randomness remains unexplored, despite its potential importance in cytoskeletal dynamics and collective migration of cell colonies. In the present thesis, we focus on the flow property and show that its response to the quenched randomness is in marked contrast with that of the orientational order. We also vary the strength of randomness over a wide range and find a transition from the weak to strong disorder regimes for wet active nematics.

1.5.3 Fluctuation in active solid featuring alignment interaction (Chap. 4)

The content of this subsection is adapted from [86] (Y. Kinoshita, N. Uchida, and A. M. Menzel, "Collective excitations in active solids featuring alignment interactions", The Journal of Chemical Physics 162, 054906 (2025)), with the permission of AIP Publishing. © (2025) AIP Publishing.

Here, we focus on active solids that introduce aligning torques. They reorient the directions of self-propulsion of each elastically coupled object towards the current direction of the elastic force acting on this object. There are two obvious states in a bulk system that should be considered: orientationally disordered states concerning the directions of self-propulsion of each object and states of a certain degree of global alignment of these directions [20, 21, 66]. Depending on the strengths of the alignment interactions, globally aligned states are conceivable, at least in finite-sized systems. Such global alignment is also observed for fluid systems featuring elastic collisions [87]. Conversely, strong rotational diffusion may still destabilize the orientational order and lead to a disordered state [21]. Confinements can favor additional modes of collective motions such as chiral oscillations [61, 63]. They result from restrictions that the confinement imposes on collective motion.

While the static properties of active solids with alignment interaction have been studied [66], the dynamical ones are still under development. Previous works focused on finite-sized systems [61, 63, 64]. In addition, it is reported that oscillations accompanied by entropy production arise when a solid state is formed by the accumulation of active Brownian particles [67, 88, 89]. Since solid states are formed by a variety of active particles [90, 91], a general analysis is desirable.

In our work, we analytically evaluate the dynamical properties of bulk systems in an orientationally ordered, collectively migrating state. To this end, the spectra of fluctuations are calculated analytically. In addition, we analytically evaluate an expression for the rate of entropy production that follows from the conventional path-integral theory [92]. In this context, continuous energy dissipation is one of the prominent characteristics of active matter, accompanied by a positive rate of entropy production [16, 93]. The rate of entropy production is useful for quantifying how far away from the equilibrium the states are. It appears that the coupling between self-propulsion and self-alignment of the migrating, elastically coupled objects introduces additional excitations that are absent in a corresponding passive system and accompanied by additional entropy production. Numerical simulations are performed for verification.

1.6 Structure of the thesis

In this study, we investigate active nematic liquid crystals and active solids.

For active nematic liquid crystals, we examine the effects of a uniform electric field (Chap. 2) and a quenched random field (Chap. 3) through numerical simulations.

For active solids, we focus on a dynamically steady state where the directions of self-propulsion of all constitutive particles are aligned in one direction, causing the solid to undergo translational motion (Chap. 4). The properties of this state are characterized by fluctuation spectra and the rate of entropy production.

Finally, in Chap. 5, we provide a summary of the study.

Chapter 2

Active nematics under an electric field

The content of this chapter is adapted from Ref. [68] (Y. Kinoshita and N. Uchida, “Flow patterns and defect dynamics of active nematic liquid crystals under an electric field”, Phys. Rev. E **108**, 014605 (2023)) © (2023) American Physical Society.

The effects of an electric field on the flow patterns and defect dynamics of two-dimensional active nematic liquid crystals are numerically investigated. We found that field-induced director reorientation causes anisotropic active turbulence characterized by enhanced flow perpendicular to the electric field. The average flow speed and its anisotropy are maximized at an intermediate field strength. Topological defects in the anisotropic active turbulence are localized and show characteristic dynamics with simultaneous creation of two pairs of defects. A laning state characterized by stripe domains with alternating flow directions is found at a larger field strength near the transition to the uniformly aligned state. We obtained periodic oscillations between the laning state and active turbulence, which resembles an experimental observation of active nematics subject to anisotropic friction.

The rest of this chapter is structured as follows. In Sec. 2.1, we present the theoretical models and conduct the linear stability analysis of a uniformly aligned state. In Sec. 2.2, numerical results are presented, and emergent patterns are distinguished with several aspects. In Sec. 2.3, we discuss the remarks and compare the parameters with the experiment of a microtubule-kinesin suspension.

2.1 Model

2.1.1 Equations

We consider a uniaxial active nematic liquid crystal in two dimensions. The orientational order is described by the symmetric and traceless tensor $Q_{ij} = S\left(n_i n_j - \frac{1}{2}\delta_{ij}\right)$, where S is the scalar order parameter and $\boldsymbol{n} = (\cos\theta, \sin\theta)$ is the director. The dynamical equations are written in the dimensionless form [17]

$$(\partial_t + \boldsymbol{v}\cdot\boldsymbol{\nabla})\,\boldsymbol{v} = \frac{1}{\mathrm{Re}}\nabla^2\boldsymbol{v} - \boldsymbol{\nabla}p + \boldsymbol{\nabla}\cdot\underline{\boldsymbol{\sigma}}, \tag{2.1}$$

$$\boldsymbol{\nabla}\cdot\boldsymbol{v} = 0, \tag{2.2}$$

$$(\partial_t + \boldsymbol{v}\cdot\boldsymbol{\nabla})\,\underline{\boldsymbol{Q}} = \lambda S\underline{\boldsymbol{u}} + \underline{\boldsymbol{Q}}\cdot\underline{\boldsymbol{\omega}} - \underline{\boldsymbol{\omega}}\cdot\underline{\boldsymbol{Q}} + \gamma^{-1}\underline{\boldsymbol{H}}. \tag{2.3}$$

Here, $\boldsymbol{v}$ is the normalized flow velocity, p is the pressure and $\underline{\boldsymbol{\sigma}}$ is the stress tensor. The flow properties are characterized by the Reynolds number Re, the flow alignment parameter λ, and the rotational viscosity γ, and $u_{ij} = (\partial_i v_j + \partial_j v_i)/2$ and $\omega_{ij} = (\partial_i v_j - \partial_j v_i)/2$ are the symmetric and antisymmetric parts of velocity gradient tensor, respectively. Hereafter we call $\omega := \omega_{xy}$ the vorticity. We assume $0 < \lambda < 1$; a positive value of λ corresponds to rod-like or filamentous material and $|\lambda| < 1$ means that there is no stable director orientation in a uniform shear flow (flow-tumbling regime) [30, 41]. The molecular field H_{ij} is defined as the symmetric and traceless part of $-\delta F/\delta Q_{ij}$, and is obtained from the Landau-de Gennes free energy [30]

$$F = \int f \mathrm{d}^2 r, \tag{2.4}$$

$$f = \frac{A}{2}\mathrm{Tr}\left(\underline{\boldsymbol{Q}} : \underline{\boldsymbol{Q}}\right) + \frac{C}{4}\left(\mathrm{Tr}\left(\underline{\boldsymbol{Q}} : \underline{\boldsymbol{Q}}\right)\right)^2 + \frac{K}{2}\left(\nabla \underline{\boldsymbol{Q}}\right)^2 - \frac{\varepsilon_a}{2}\boldsymbol{E} \cdot \underline{\boldsymbol{Q}} \cdot \boldsymbol{E}. \tag{2.5}$$

The first two terms of the free energy density control the magnitude of the scalar order parameter S, the third term is the Frank elastic energy under the one-constant approximation, and the fourth term describes the coupling to the electric field. Here, we dropped the term proportional to $\mathrm{Tr}\,\underline{\boldsymbol{Q}}^3$ contained in the standard expression of the Landau de Gennes free energy, because it identically vanishes for the two-dimensional nematic order parameter. We assume positive dielectric anisotropy ($\varepsilon_a > 0$) so that the director tends to align parallel to the electric field, mimicking the response of an individual microtubule [71, 73]. The molecular field is obtained as

$$H_{xx} = -\left(2A + CS^2\right) Q_{xx} + 2K\nabla^2 Q_{xx} + \frac{\varepsilon_a}{2}\left(E_x^2 - E_y^2\right). \tag{2.6}$$

$$H_{xy} = -\left(2A + CS^2\right) Q_{xy} + 2K\nabla^2 Q_{xy} + \varepsilon_a E_x E_y. \tag{2.7}$$

The stress tensor is the sum of the passive stress

$$\underline{\boldsymbol{\sigma}}^{\mathrm{e}} = -\lambda S \underline{\boldsymbol{H}} + \underline{\boldsymbol{Q}} \cdot \underline{\boldsymbol{H}} - \underline{\boldsymbol{H}} \cdot \underline{\boldsymbol{Q}}, \tag{2.8}$$

and the active stress

$$\underline{\boldsymbol{\sigma}}^{\mathrm{a}} = -\alpha \underline{\boldsymbol{Q}}. \tag{2.9}$$

We assume that the activity parameter α is positive, which corresponds to an extensile system.

2.1.2 Linear stability analysis

In the absence of an electric field, the model exhibits macroscopically isotropic active turbulence. Because we assumed positive dielectric anisotropy, the electric field is expected to align the director and stabilize a uniform ordered state if the field is sufficiently strong. We conducted a linear stability analysis of the uniformly aligned state to find the threshold electric field and analyzed the onset of instability. We assume a uniform electric field along the x-axis ($\boldsymbol{E} = E\boldsymbol{e}_x$). We also assume that the system is far from the nematic-isotropic transition point and that the scalar order parameter is given by the equilibrium value S_0, which satisfies

$$-S_0\left(A + \frac{C}{2}S_0^2\right) + \frac{\varepsilon_a}{2}E^2 = 0. \tag{2.10}$$

In the unperturbed quiescent state, the director is aligned along the x-axis so that

$$\boldsymbol{v}_0 = \boldsymbol{0}, \quad Q_{xx,0} = \frac{S_0}{2}, \quad Q_{xy,0} = 0, \tag{2.11}$$

where the subscript 0 means the unperturbed state. We consider perturbations to the flow velocity $\delta\boldsymbol{v}$ and the director angle $\delta\theta$, which gives the variations of the order parameter

$$\delta Q_{xx} = \frac{S_0}{2}[\cos(2\delta\theta) - 1] \simeq 0, \tag{2.12}$$

$$\delta Q_{xy} = \frac{S_0}{2}\sin(2\delta\theta) \simeq S_0\delta\theta. \tag{2.13}$$

Assuming the time dependence proportional to $\mathrm{e}^{-\mathrm{i}\omega t}$, where ω is the complex frequency, we expand the director angle and flow velocity in the Fourier modes as

$$\theta(\boldsymbol{r}, t) = \frac{1}{(2\pi)^2}\int \mathrm{d}^2k\, \delta\theta^{\boldsymbol{k}} e^{\mathrm{i}(\boldsymbol{k}\cdot\boldsymbol{r} - \omega t)}, \tag{2.14}$$

$$\boldsymbol{v}(\boldsymbol{r}, t) = \frac{1}{(2\pi)^2}\int \mathrm{d}^2k\, \delta\boldsymbol{v}^{\boldsymbol{k}} e^{\mathrm{i}(\boldsymbol{k}\cdot\boldsymbol{r} - \omega t)}, \tag{2.15}$$

where $\boldsymbol{k} = (k_x, k_y) = (k\cos\phi, k\sin\phi)$ is the wavevector. Because $\theta = 0$ and $\boldsymbol{v} = 0$ in the unperturbed state, we consider only the modes with nonzero wavevectors. Similarly, we expand Q_{ij}, H_{ij}, σ_{ij} and p in the Fourier space and then to the first order of $\delta\theta^{\boldsymbol{k}}$ and $\delta\boldsymbol{v}^{\boldsymbol{k}}$. From Eqs.(2.12,2.13), we have $\delta Q^{\boldsymbol{k}}_{xx} \simeq 0$ and $\delta Q^{\boldsymbol{k}}_{xy} \simeq S_0\delta\theta^{\boldsymbol{k}}$. The molecular field vanishes in the unperturbed state: $H_{ij,0} = 0$. Its variations are read from Eqs.(2.6,2.7) as $\delta H^{\boldsymbol{k}}_{xx} \propto \delta Q^{\boldsymbol{k}}_{xx} \simeq 0$ and

$$\delta H^{\boldsymbol{k}}_{xy} \simeq \left[-\left(2A + CS_0^2\right) - Kk^2\right]\delta Q^{\boldsymbol{k}}_{xy} \simeq -D\delta\theta^{\boldsymbol{k}}, \tag{2.16}$$

where we introduced the abbreviation

$$D = D(k) \equiv \varepsilon_a E^2 + 2KS_0k^2 \tag{2.17}$$

and used Eq.(2.10). For the stress tensor, we readily obtain $\delta\sigma_{xx} = -\delta\sigma_{yy} \simeq -\lambda S_0\delta H_{xx} - \alpha\delta Q_{xx} \simeq 0$,

$$\begin{aligned}\delta\sigma^{\boldsymbol{k}}_{xy} &\simeq (1-\lambda)S_0\delta H^{\boldsymbol{k}}_{xy} - \alpha\delta Q^{\boldsymbol{k}}_{xy} \\ &\simeq [(\lambda - 1)D - \alpha]\, S_0\delta\theta^{\boldsymbol{k}},\end{aligned} \tag{2.18}$$

and

$$\begin{aligned}\delta\sigma^{\boldsymbol{k}}_{yx} &\simeq -(1+\lambda)S_0\delta H^{\boldsymbol{k}}_{xy} - \alpha\delta Q^{\boldsymbol{k}}_{xy} \\ &\simeq [(\lambda + 1)D - \alpha]\, S_0\delta\theta^{\boldsymbol{k}}.\end{aligned} \tag{2.19}$$

The equation of motion (2.1) is linearized as

$$-\mathrm{i}\omega\delta v^{\boldsymbol{k}}_i = -\frac{k^2}{\mathrm{Re}}\delta v^{\boldsymbol{k}}_i - \mathrm{i}k_i\delta p^{\boldsymbol{k}} + \mathrm{i}k_j\delta\sigma^{\boldsymbol{k}}_{ij}. \tag{2.20}$$

Summation over repeated indices ($i, j = x, y$) is assumed here and hereafter. The pressure in (2.20) is determined by the incompressibility condition (2.2), or equivalently $\boldsymbol{k} \cdot \delta \boldsymbol{v}^{\boldsymbol{k}} = 0$, as

$$\delta p^{\boldsymbol{k}} = \hat{k}_i \hat{k}_j \delta \sigma_{ij}^{\boldsymbol{k}}, \tag{2.21}$$

where we introduced $\hat{\boldsymbol{k}} = \boldsymbol{k}/|\boldsymbol{k}| = (\hat{k}_x, \hat{k}_y) = (\cos\phi, \sin\phi)$. The incompressibility condition allows us to express the velocity by the perpendicular component

$$\delta v_{\perp}^{\boldsymbol{k}} = -\hat{k}_y \delta v_x^{\boldsymbol{k}} + \hat{k}_x \delta v_y^{\boldsymbol{k}} \tag{2.22}$$

as

$$\delta \boldsymbol{v}^{\boldsymbol{k}} = (\delta v_x^{\boldsymbol{k}}, \delta v_y^{\boldsymbol{k}}) = \delta v_{\perp}^{\boldsymbol{k}} (-\hat{k}_y, \hat{k}_x). \tag{2.23}$$

Rewriting (2.20) in terms of $\delta v_{\perp}^{\boldsymbol{k}}$ and substituting (2.18,2.19), we get

$$\begin{aligned} -\mathrm{i}\omega \delta v_{\perp}^{k} &= -\frac{k^2}{\mathrm{Re}} \delta v_{\perp}^{k} - \mathrm{i}k \left(\hat{k}_y^2 \delta \sigma_{xy}^{k} - \hat{k}_x^2 \delta \sigma_{yx}^{k} \right) \\ &= -\frac{k^2}{\mathrm{Re}} \delta v_{\perp}^{k} - \mathrm{i}k \left[\left(\hat{k}_y^2 - \hat{k}_x^2 \right) (\lambda D - \alpha) - D \right] S_0 \delta \theta^{k}. \end{aligned} \tag{2.24}$$

On the other hand, the dynamical equation (2.3) for the order parameter is linearized as

$$\begin{aligned} -\mathrm{i}\omega S_0 \delta \theta^{k} &= S_0 \left(\frac{\lambda + 1}{2} \mathrm{i}k_x \delta v_y^{k} + \frac{\lambda - 1}{2} \mathrm{i}k_y \delta v_x^{k} \right) - \frac{1}{\gamma} D \delta \theta^{k} \\ &= \mathrm{i}k S_0 \left(\frac{\lambda + 1}{2} \hat{k}_x^2 - \frac{\lambda - 1}{2} \hat{k}_y^2 \right) \delta v_{\perp}^{k} - \frac{1}{\gamma} D \delta \theta^{k} \end{aligned} \tag{2.25}$$

with the aid of Eqs.(2.13,2.16,2.17,2.23). Eqs.(2.24,2.25) are written in the matrix form

$$-\mathrm{i}\omega \begin{pmatrix} \delta v_{\perp}^{\boldsymbol{k}} \\ \delta \theta^{\boldsymbol{k}} \end{pmatrix} = \mathcal{M} \begin{pmatrix} \delta v_{\perp}^{\boldsymbol{k}} \\ \delta \theta^{\boldsymbol{k}} \end{pmatrix} \tag{2.26}$$

with

$$\mathcal{M} = \begin{pmatrix} -\frac{k^2}{\mathrm{Re}} & \mathrm{i}k S_0 \left[(\lambda \cos 2\phi + 1) D - \alpha \cos 2\phi \right] \\ \mathrm{i}k \frac{\lambda \cos 2\phi + 1}{2} & -\frac{D}{\gamma S_0} \end{pmatrix}. \tag{2.27}$$

A straightforward calculation gives the eigenvalues $-\mathrm{i}\omega_{\pm}^{\boldsymbol{k}}$ of $\mathcal{M}$, and the stability condition is obtained as $\mathrm{Im}\,\omega_{\pm}^{\boldsymbol{k}} \leq 0$ for any $\boldsymbol{k}$; see Appendix A for details. We identified the most unstable mode that maximizes the linear growth rate $\mathrm{Im}\,\omega^{\boldsymbol{k},j}$ ($j = 1, 2$) for given α and E. For a given angle ϕ of the wavevector, the mode in the long-wavelength limit ($k \to 0$) is most unstable, which is trivial since Frank elasticity suppresses deformation. For a given wavenumber k, the mode with the $\phi = 0$ is most unstable in the range $0 < \lambda < 1$ assumed in this paper. This is in accordance with the general observation on extensile (or "pusher"-type) active matter that the active stress induces bend deformation of the axis of alignment [39, 94], which is interpreted as a buckling instability of the filaments [95]. The stability condition is given by

$$\alpha < \alpha_c = \left(\lambda + 1 + \frac{B}{\lambda + 1} \right) \varepsilon_a E^2, \quad B = \frac{2}{\gamma S_0^2 \mathrm{Re}}. \tag{2.28}$$

Note that B weakly depends on E via the cubic equation (2.10) for S_0, and the analytical expression of $\alpha_c = \alpha_c(E)$ becomes voluminous. For numerical analysis, we choose the parameter values

$$A = -0.15,\ C = 0.4,\ K = 0.5,\ \varepsilon_a = 1, \tag{2.29}$$

$$\lambda = 0.1,\ \mathrm{Re} = 0.1,\ \gamma = 10. \tag{2.30}$$

We varied the field strength in the range $0 \leq E \leq 0.3$. The stability threshold is given by $\alpha_c = 0.1$ for $E \simeq 0.175$ and $\alpha_c = 0.2$ for $E \simeq 0.255$, for example.

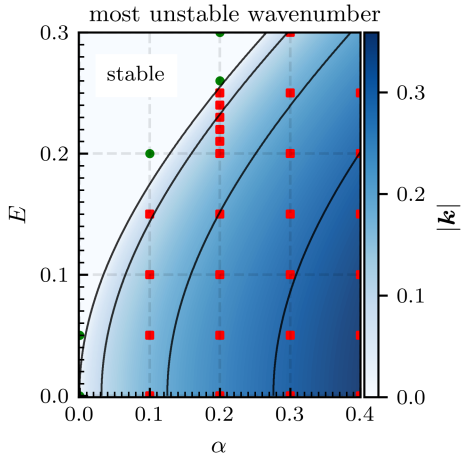

Figure 2.1: Results of the linear stability analysis for a uniformly aligned state. Contour lines for the most unstable wavenumber $|\boldsymbol{k}| = 0, 0.1, 0.2, 0.3$ are shown in solid lines. The stability threshold coincides with the contour line for $k = 0$. For a given value of $|\boldsymbol{k}|$, the direction of the most unstable wavevector is parallel to the unperturbed director. The result of numerical simulations is shown by circles (squares) where the uniformly aligned state is stable (unstable).

In Fig.2.1, we plot the magnitude of the most unstable wavenumber as a function of α and E. The region $|\boldsymbol{k}| = 0$ is identical with the linearly stable region. The contour line for $|\boldsymbol{k}| = 0$ means the stability threshold and starts from the origin $(\alpha, E) = (0, 0)$. The most unstable wavenumber increases as α increases or E decreases.

2.2 Numerical Results

2.2.1 Method and parameters

We numerically solved the equations Eqs.(2.1,2.2,2.3) on a square lattice with the fourth-order Runge–Kutta method. The incompressibility condition is handled by the simplified MAC method on a staggered lattice [96]. The main sublattice is used for $\underline{\boldsymbol{Q}}(\boldsymbol{r}, t)$ and the auxiliary field variables p, $\underline{\boldsymbol{\sigma}}$, $\underline{\boldsymbol{u}}$, $\underline{\boldsymbol{\omega}}$ and $\underline{\boldsymbol{H}}$, and the other two are assigned to $v_x(\boldsymbol{r}, t)$ and $v_y(\boldsymbol{r}, t)$. The calculation is performed on a $N_x \times N_y$ lattice with the grid size $\Delta x = \Delta y = 2$ and the periodic boundary conditions, with the step time increment $\Delta t = 0.01$. We used the Fast Fourier Transform to solve the Laplace equation for the pressure at each time step. The parameter values used in the simulation are given in Eqs.(2.29,2.30). The system size is fixed to $N_x = N_y = 128$ so that $L = N_x \Delta x = N_y \Delta y = 256$. In a equilibrium state that minimizes the Landau-de Gennes free energy with $E = 0$, the scalar order parameter is given by $S_0 = \sqrt{2|A|/C} \simeq 0.87$ and the defect core radius is $\xi = \sqrt{K/|A|} \simeq 1.83$. We varied the activity parameter α and the electric field strength E. For the initial conditions, we set the velocity to zero and assumed small random fluctuations around zero for $\underline{\boldsymbol{Q}}(\boldsymbol{r}, 0)$, assuming a quench from the isotropic quiescent state. We observed the total kinetic energy as a function of time to confirm that the system reached dynamical steady states, typically by $t = 10000$ for active turbulence states. We calculated statistical data over the time window $t_0 < t < t_0 + 20000$ after the system reached the dynamical steady state (t_0 is varied depending on the parameter).

2.2.2 Spatiotemporal patterns and flow anisotropy

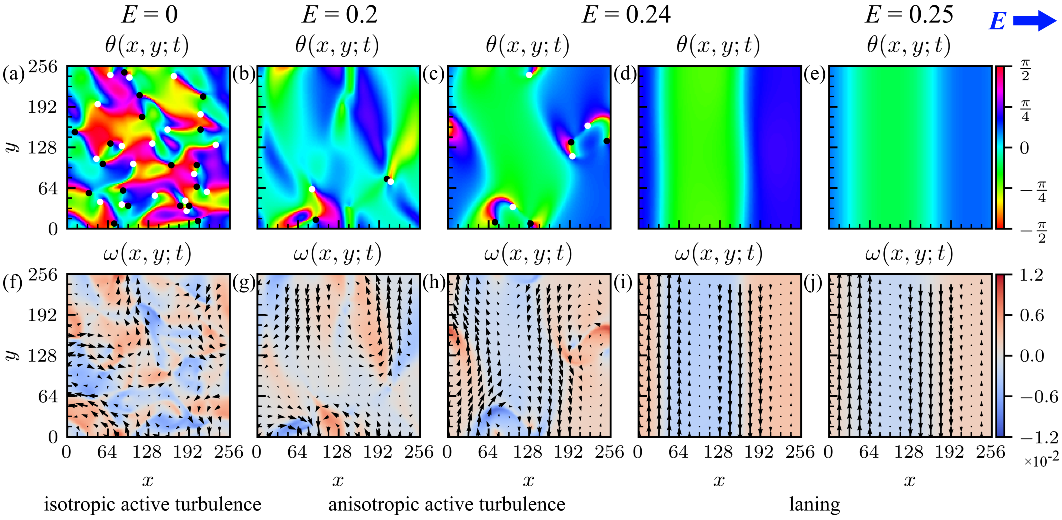

Figure 2.2: Snapshots of the director angle $\theta(x, y)$ (top row) and the vorticity $\omega(x, y)$ with the velocity field shown by arrows (bottom row) in the dynamical steady states for $\alpha = 0.2$. (a),(f) Isotropic active turbulence ($E = 0$). (b),(g) Anisotropic active turbulence ($E = 0.2$). We find a periodic switching between (c),(h) anisotropic turbulence and (d),(i) a laning state ($E = 0.24$). (e), (j) A steady laning state ($E = 0.25$).

In Fig.2.2, we show the snapshots of the director angle $\theta(\boldsymbol{r}, t)$ and the vorticity $\omega(\boldsymbol{r}, t)$ in the dynamical steady states for $\alpha = 0.2$. For $E = 0$, we obtain active turbulence containing topological defects and vortices that are macroscopicaly isotropic [Fig.2.2(a)(f)]. For $E = 0.2$, the director is tilted toward the electric field and forms anisotropic active turbulence with fewer defects and vortices compared to the zero-field case [Fig.2.2(b)(g)]. For $E = 0.24$, we observe a periodical switching between the anisotropic turbulence [Fig.2.2(c)(h)] and a laning state with bidirectional flow [Fig.2.2(d)(i)]. A steady laning state is obtained at $E = 0.25$ [Fig.2.2(e)(j)]. For $E \geq 0.26$, uniformly aligned state is obtained (not shown). In Fig.2.1, we plot the parameter sets where uniformly aligned states are stable (unstable) by circles (squares), which agree with the result of the linear stability analysis.

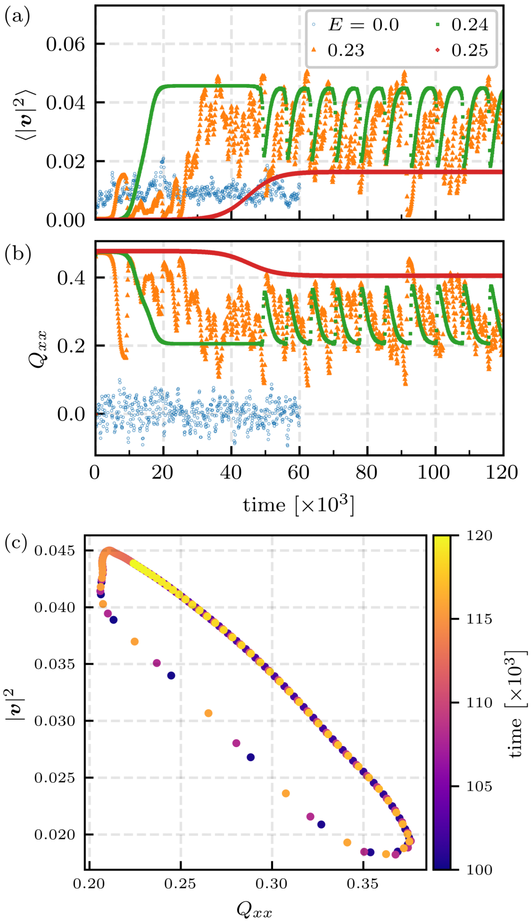

Figure 2.3: Time development of (a) the mean square velocity $\langle \boldsymbol{v}^2 \rangle$ and (b) the order parameter component $\langle Q_{xx} \rangle$. (c) Trajectory in the $\langle Q_{xx} \rangle$-$\langle \boldsymbol{v}^2 \rangle$ plane for $E = 0.24$. Time evolution takes place in the anticlockwise direction. The data are for $\alpha = 0.2$.

In Fig.2.3(a)(b), we show time evolution of the mean square velocity $\langle |\boldsymbol{v}^2| \rangle$ and the order parameter component $\langle Q_{xx} \rangle$, respectively, for a specific sample (initial condition), where the average is taken over space. Compared to the isotropic active turbulence at $E = 0$, the anisotropic turbulence at $E = 0.23$ has a longer incubation time for the velocity to grow, and has larger mean value and fluctuations in the dynamical steady state. At $E = 0.24$, we find periodic oscillations between the anisotropic turbulence and laning state. The active flow velocity reaches a plateau by $t = 50 \times 10^3$, which corresponds to the laning state. Then the velocity rapidly decreases as the lane collapses and emits multiple pairs of defects. The defects slowly annihilate, leaving a lane behind. This cycle is repeated until the end of the simulation, with the period $T \simeq 7 \times 10^3$. The laning state for $E = 0.25$ has a larger steady state value of the mean square velocity than the isotropic turbulence. Under the electric field, the degree of alignment $\langle Q_{xx} \rangle$ has negative correlation with the velocity, which is most clearly seen in the oscillations for $E = 0.24$. In Fig.2.3(c), we show time-evolution of the system in the $\langle Q_{xx} \rangle - \langle |\boldsymbol{v}^2| \rangle$ plane. The system makes an anticlockwise cycle in the plane, with the slow phase characterized by a larger velocity magnitude than the rapid phase. Because the slow phase involves straightening of lanes it is natural that it generates stronger flow than the rapid phase where flow is turbulent and slow.

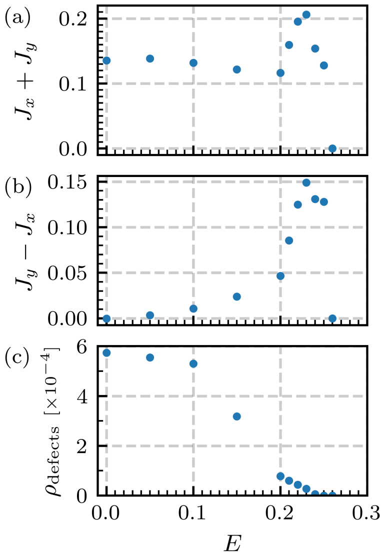

Figure 2.4: (a) Total flux $J_x + J_y$, (b) anisotropy of flux $J_x - J_y$, and (c) defect density $\rho_{\rm defect}$ versus the field strength E. The data are for $\alpha = 0.2$.

To characterize the orientation of flow, we define $J_x = \sqrt{\langle v_x^2 \rangle}$ and $J_y = \sqrt{\langle v_y^2 \rangle}$, where the average is taken over time and 10 independent samples. In Fig.2.4(a)(b), we plot the sum $J_x + J_y$ and difference $J_y - J_x$ as functions of E. As E is increased, the sum $J_x + J_y$ shows a slow decline for $E \le 0.20$ and then a sharp peak at $E = 0.23$, which corresponds to the anisotropic active turbulence. It rapidly decreases to zero as the electric field is further increased. The flow anisotropy characterized by $J_y - J_x$ increases as E is increased and also has a peak at $E = 0.23$. In Fig.2.4(c), we plot the number density of topological defects, which maintains a large value for $E \le 0.1$ and then rapidly decreases as a function of E.

2.2.3 Distributions and correlation functions

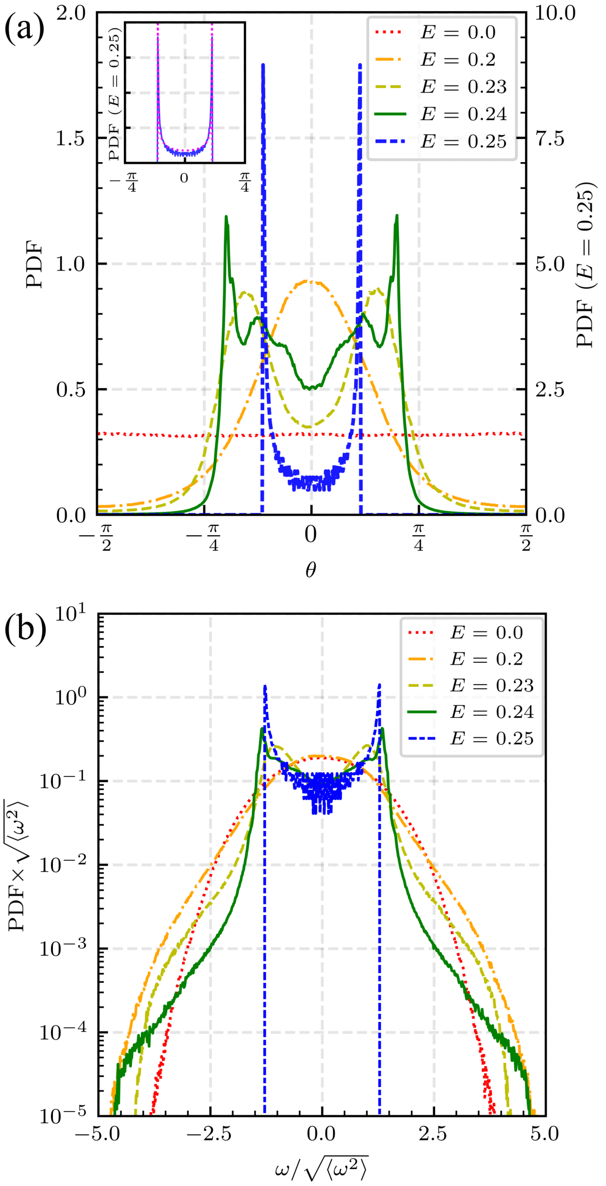

Figure 2.5: Normalized probability distribution functions of (a) the director angle θ and (b) the vorticity ω, both for $\alpha = 0.2$. In (a), the data for $E = 0.25$ are scaled by the right vertical axis. The inset of (a) shows comparison with the theoretical line for the sinusoidal undulation, $f(\theta) = 1/[\pi(\theta_0^2 - \theta^2)^{1/2}]$ ($|\theta| < \theta_0$, dotted lines).

In Fig.2.5, we show the probability distribution functions (PDFs) of the director angle and vorticity for $\alpha = 0.2$ calculated from an ensemble of 10 samples. The PDF of the director angle [Fig.2.5(a)] has a single peak at $\theta = 0$ for $0 < E \leq 0.20$, with its height increasing with E. The peak splits into two at $E = 0.23$, which is interpreted as a precursor of the laning state. At $E = 0.24$, the PDF has four peaks resulting from coexistence of narrow and wide lanes. Depending on the initial condition, we obtained either narrow lanes with the period equal to $L/2$, or wide lanes with the period equal to the system size (L). Each type of lanes sporadically collapse into a defected state and recover, but do not interchange with each other. We find narrow lanes in 4 out of the 10 samples, and wide lanes in 6 samples. The wide lanes contribute to the two higher peaks of the distribution function at larger values of $|\theta|$, and narrow lanes contribute to the lower peaks. The steady laning state at $E = 0.25$ has two sharp peaks at $|\theta| = \theta_0 \simeq \pi/8$ with no tails. The peak position is closer to $\theta = 0$ than the case $E = 0.24$, which means that the undulation is suppressed by the electric field. Note that the PDF for a sinusoidal undulation $\theta(x) = \theta_0 \sin kx$ is proportional to $|dx/d\theta| \propto (\theta_0^2 - \theta^2)^{-1/2}$ for $|\theta| < \theta_0$ and is zero for $|\theta| > \theta_0$ (see Appendix B for derivation). In the inset of Fig.2.5(a), we see that the formula gives a good approximation of the PDF for $E = 0.25$, with the minimum at $\theta = 0$ slightly lower than the theoretical value. The PDF for the vorticity [Fig.2.5(b)] is nearly Gaussian for $E = 0$, while a small deviation (fat tail) appears at $E = 0.20$ and then the peak splits into two at $E = 0.23$. The distribution gets narrower tails as E is further increased to $E = 0.25$.

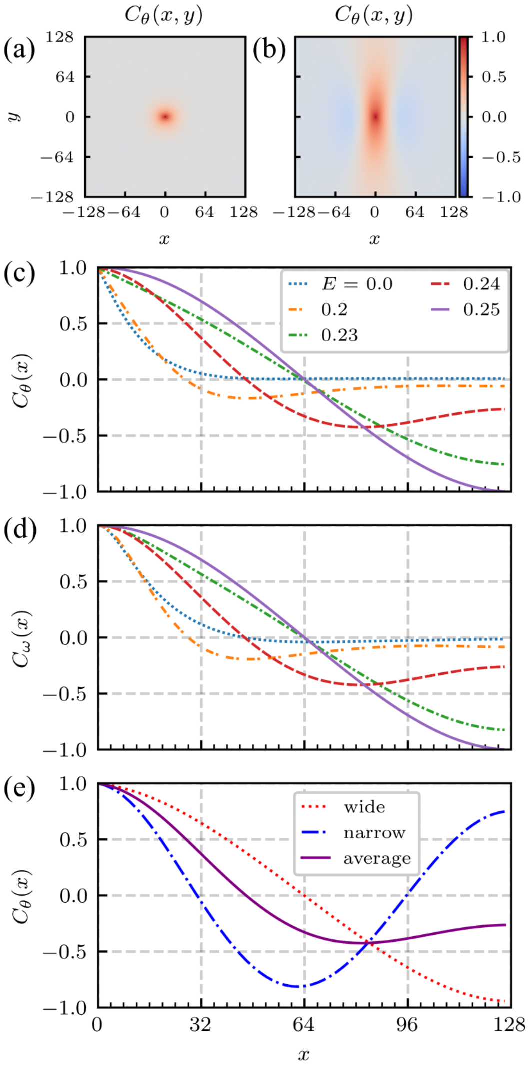

Figure 2.6: Spatial correlation functions of the director at (a) $E = 0$ and (b) $E = 0.2$, both for $\alpha = 0.2$. Spatial correlation functions along the x-axis for (c) the director angle and (d) the vorticity. (e) $C_\theta(x, 0)$ for $E = 0.24$, for narrow lanes (4 samples), wide lanes (6 samples) and the ensemble average.

In Fig.2.6, we plot the spatial correlation functions for the director angle and vorticity, which are defined by

$$C_\theta(\boldsymbol{r}) = \frac{\langle \theta(\boldsymbol{r}+\boldsymbol{r}', t)\theta(\boldsymbol{r}', t)\rangle}{\langle \theta(\boldsymbol{r}', t)^2\rangle} \tag{2.31}$$

and

$$C_\omega(\boldsymbol{r}) = \frac{\langle \omega(\boldsymbol{r}+\boldsymbol{r}', t)\omega(\boldsymbol{r}', t)\rangle}{\langle \omega(\boldsymbol{r}', t)^2\rangle}, \tag{2.32}$$

respectively, where $\langle\cdots\rangle$ indicates averages over $\boldsymbol{r}'$ and t, and 10 independent samples. The angular correlation function for $E = 0$ are isotropic as shown in Fig.2.6(a). Under an electric field ($E = 0.2$), the correlation functions develop anisotropic structures with peaks elongated in the y-direction and valleys in the x-direction, as seen in Fig.2.6(b). The correlation profiles along the line $y = 0$ are shown in Fig.2.6(c)(d). Because $C_\theta(x) = C_\theta(x, 0)$ and $C_\omega(x) = C_\omega(x, 0)$ show very similar behaviors, except that the latter shows a slightly non-monotonic decay for $E = 0$, we focus on the former. The anisotropic turbulence for $E = 0.2$ is characterized by a shallow minimum at $x \simeq 40$. For $E = 0.23$, we observe irregular temporal fluctuations between a wide lane and a turbulent state, which is reflected in the fluctuations of the velocity and order parameter [Fig. 2.3(a)(b)]. Since the correlation function for the turbulent state has a shallow minimum. the minimum of the time-averaged correlation function is dominantly determined by that of the wide lane. This explains the minimum of $C_\theta(x)$ at $x \simeq L$ for $E = 0.23$. For $E = 0.24$, the minimum of $C_\theta(x)$ is located at a shorter distance ($x \simeq 80$) compared to those for $E = 0.23$ and 0.25. This is explained by coexistence of narrow and wide lanes mentioned in the previous paragraph. In Fig.2.6(c), we show the correlation functions for the subsets of samples with narrow and wide lanes, and the ensemble average. We see that the average of the correlation functions for narrow and wide lanes gives a shallow minimum at a distance between $L/2$ and L. Finally, for $E = 0.25$, we find only a wide lane, which gives the deep minimum of $C_\theta(x)$ at $x = L$.

2.2.4 Defect dynamics

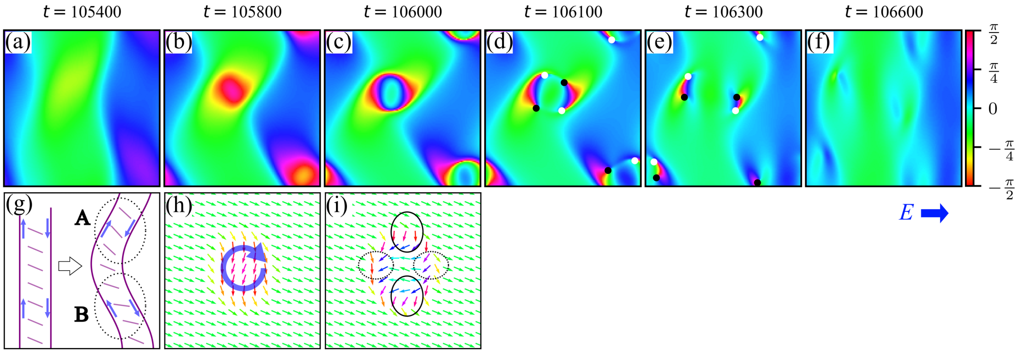

Figure 2.7: (a)-(f) Snapshots of the defects creation and annihilation process at $\alpha = 0.2$ and $E = 0.23$; (a) the director has small tilt angle in the center region; (b) an island of large tilt angle appears; (c) further rotation of the director inside the island; (d) the island breaks up into two crescent-like shapes and two pairs of defects are created; (e) the crescent-shape regions shrink; (f) defects annihilate by collision. (g)-(i) Schematic pictures of the defect creation process; (g) a straight lane undergoes a buckling instability and form the oppositely tilted regions A and B. The active flow along the lane boundary (arrows) generates a torque that enhances the clockwise tilt in A, while it suppresses the anti-clockwise tilt in B. (h) The resultant deformation of the director field induces further rotation in the center region; (i) Bend deformation in the top and bottom regions (solid lines) and splay deformation on the left and right hand sides (dotted lines). The former is transformed to splay deformation by creating two pairs of defects.

In the anisotropic turbulence state, we observe characteristic dynamics of topological defects. A typical time series of defect creation and annihilation is shown in Fig.2.7. Starting from a weakly deformed director configuration [Fig.2.7(a)], flow-induced instability generates an island of large tilt angle [Fig.2.7(b)]. Large curvature of the director field further enhances rotation of the director in the island [Fig.2.7(c)], and two pairs of $\pm 1/2$ defects are created at the periphery of the island [Fig.2.7(d)]. The island is broken by creation of defects into two parts of crescent-shape with a pair of defects at their ends. As they shrink, the defects approach each other and annihilate by collision [Fig.2.7(e)(f)]. To illustrate the mechanism of defect creation, we show schematic pictures of the lanes and director field in Fig.2.7(g)(h)(i). An initially straight lane undergoes a buckling instability due to the active stress along the lane boundary, forming oppositely tilted regions shown as A and B in Fig.2.7(g). The director in A and B are tilted clockwise and anticlockwise, respectively. On the other hand, the active flow at the lane boundaries (arrows) generates a clockwise hydrodynamic torque at the center of the lane, and enhances (suppresses) the tilt in the region A (B). It causes a rotation of the director in the center of A, forming the patterns in Fig.2.7(b)(h). The deformation generates active flow shown by the thick arrow in Fig.2.7(h) and further rotates the director field. as in Fig.2.7(i), where bend deformation is found in the encircled regions in the top and bottom (solid lines), while splay deformation is found on the left and right hand side (dotted lines). Then, following the scenario of defect creation [42], bend deformation is transformed to splay deformation by creating a pair of defects at each of the top and bottom regions.

2.3 Discussion

We studied the effects of an electric field on the flow and defect patterns of active nematics in two dimensions. The anisotropic active turbulence under an electric field is characterized by flow anisotropy. The magnitude and degree of anisotropy of the flow are both maximized at an intermediate field strength. The decrease of defects with increased field strength is in agreement with the previous numerical result for three-dimensional active nematics [45]. We find that vortices are localized in the anisotropic active turbulence, which is reflected in the long tail in the probability distribution of vorticity. As each localized vortex is isolated, topological defects are created and annihilated in each vortex region. This is in contrast with the isotropic active turbulence state where defects are created at walls and move along them [42].

A strong electric field stabilizes the uniform aligned state, and we determined the threshold by a linear stability analysis. The most unstable wavevector is parallel to the unperturbed director along the electric field, which corresponds to a bend deformation. This is interpreted as a buckling of the director or the filament due to the extensile active stress [39, 94, 95]. In the three-dimensional numerical simulation [45], the electric field induced a direct transition between active turbulence and uniformly aligned states. The transition threshold was estimated in the unit of $E_0 = \sqrt{K/(\varepsilon_a \xi^2)}$ as $E_c/E_0 \simeq 0.7$ for the activity strength $\alpha = 0.13(K/\xi^2)$, where the notations are translated to those of our model and ξ is the correlation length for a passive nematic. Using the expression $\xi = \sqrt{K/|A|}$ for our two-dimensional model, the threshold field strength obtained by the linear stability analysis reads $E_c/E_0 \simeq 0.19$ for the same activity strength $\alpha = 0.13(K/\xi^2) \simeq 0.0195$. The threshold is lower than in the previous study, which might be explained by the difference in the flow-aligning parameter λ. We used $\lambda = 0.1$, which locates our system deep in the flow-tumbling regime, while the value $\lambda = 1$ assumed in Ref. [45] corresponds to the threshold between the flow-aligning and tumbling regimes [30]. The smaller value of λ in our study means that the active flow induced by a director undulation has less positive feedback to amplify the deformation, and that it is suppressed by a weaker electric field. On the other hand, the space dimension would not affect the stability threshold, because the bend deformation takes place in a plane containing the director and thus is essentially two-dimensional.

A more significant difference from the previous study [45] is the emergence of the laning state in two dimensions, which we found between the anisotropic turbulence and uniformly aligned state. We interpret it as the result of confinement of the director in a plane. The absence of lanes in the three-dimensional case suggests that a sinusoidal director undulation might be unstable for out-of-plane deformations, and the secondary instability could set in at the same threshold as the first (linear) instability. A weakly nonlinear stability analysis of the laning state in three dimensions would be useful in verifying this picture. We also find a temporal oscillation between the active turbulence and laning states. A lane undergoes a buckling instability due to the extensile active stress along the lane boundary. The resultant hydrodynamic torque explains local rotation of the director field and simultaneous creation of two pairs of defects.

Experimentally, confinement of the active nematics in a quasi-two channel causes friction between the fluid and walls. Friction also induces transitions from anisotropic turbulence to a laning state, as shown both experimentally [60] and numerically [52, 53, 55]. In the experiment [60], anisotropic friction was realized by a contacting smectic liquid crystal, and a periodic switching between a laning state and a disordered flow pattern was observed. The oscillatory behavior resembles our finding, but it should be noted that the laning state in the experiment contains arrays of defects and is not equivalent to the defectless laning state found in our simulation. In the numerical simulations, laning states were induced by isotropic [52, 55] or anisotropic [53] friction with a substrate. For isotropic friction, the lane orientation is selected by spontaneous symmetry breaking in contrast to the present model. For anisotropic friction, a non-monotonic dependence of the flow anisotropy on the strength of friction and temporal fluctuations of the lane speed are reported [53], which are qualitatively similar to our findings. However, it should be stressed that friction in the previous works did not produce the uniformly aligned state. We showed for the first time that active nematics can exhibit the three states (active turbulence, laning and uniform states) by tuning a single parameter. If we simultaneously impose anisotropic friction and an electric field in different orientations, their competition may give rise to more complex patterns, which we leave for future study.

The present study assumed constant and static dielectric anisotropy. A microtubule (MT) is a highly negatively charged biopolymer, and has both a permanent dipole moment due to that of tubulin dimers and an induced dipole moment due to motion of couterions along its long axis [97, 98]. As a result, MTs are aligned by both AC [73] and DC electric field [69, 71]. In an AC electric field, MTs obtain high conductivity due to the couterion motion, which plays a key role in determining their polarization [73]. Electroorientation in a DC electric field is observed for MTs adsorbed onto a substrate [69] and in kinesin gliding assays [70–72]. Alignment was achieved by field strengths $E \leq 50$ kV/m in the kinesin gliding assays, while the speed of microtubule was unchanged up to 110 kV/m [70] or had no anisotropy due to the field [99], suggesting that steps in the kinesin ATP cycle are not affected by the electric field [99]. However, surface-coated kinesins hinder the alignment of MTs depending on their density [71]. Motion of MTs in a suspension is also affected by counterion convection [73], electro-osmotic, and electro-thermal flow [100]. A recent experimental study on the response of a dense network of MTs reported accumulation of MT bundles under a pulse electric field [101]. A microscopic model of an active suspension of microtubules and motors would be useful in elucidating the dynamic effects of an electric field. In an AC electric field, the intrinsic molecular polarity of MTs is irrelevant in determining the electric polarity and not sorted by the electric field. Therefore, it would be legitimate to use the nematic order parameter in describing the alignment. Also, the timescale of electroorientation of individual MTs (~ 0.1 s) is much larger than the alternating period of induced electric dipoles [73], while it is smaller than the characteristic timescale of active vortices (~ 10 s [38]). Therefore, the present model could be straightforwardly generalized to a model of MT-kinesin suspensions under an AC electric field on a slow timescale, although experimental knowledge on filament-motor interaction under an AC field is lacking. On the other hand, in a DC field or a low-frequency AC field, the electric polarity of MTs is determined by the intrinsic polarity and their electrophoretic motion could dominate active flow, which is presumably weakened due to field-induced polarity sorting. The combined effects of confinement [41, 50] and an electric field on active turbulence are also an interesting topic left for future work.

Chapter 3

Active nematics with quenched random field

The content of this chapter is adapted from Ref. [75] (Y. Kinoshita and N. Uchida, “Active nematic liquid crystals under a quenched random field”, arXiv:2404.08524.).

Coupling between flow and orientation is a central issue in understanding the collective dynamics of active biofilaments and cells. Active stress generated by motor activity destroy (quasi-)long-range orientational order and induce chaotic vortex flows. In cellular and subcellular environments, alignment is also hindered by heterogeneous filamentous structures in extracellular matrix and various organelles in a cell. Here we address the effects of a quenched random field on the flow patterns and orientational order in two-dimensional active nematic liquid crystals. We found that the director dynamics is frozen above a critical disorder strength. For sufficiently strong randomness, the orientational correlation function decays exponentially with the distance, reproducing the behavior of passive random-field nematics. In contrast, the flow velocity decreases only gradually as the randomness is increased, and develops a logarithmic spatial correlation for strong disorder. The threshold between the activity- and disorder-dominated regimes is specified and its dependence on the activity parameter is discussed.

This chapter is structured as follows: in Sec. 3.1, the theoretical models are presented, and effective disorder parameters are introduced. In Sec. 3.2, an analytical calculation of spatial correlation in a disordered state is conducted. In Sec. 3.3, the conditions for numerical calculations are provided. in Sec. 3.4, the change of patterns as the increase of the field strength is explained. in Sec. 3.5, the correlation functions are shown. Section 3.6 is devoted to conclusions and perspectives.

3.1 Model

The orientational order of a two-dimensional nematic liquid crystal is described by the symmetric and traceless tensor $Q_{ij} = S\left(n_i n_j - \frac{1}{2}\delta_{ij}\right)$, where S is the scalar order parameter and $\boldsymbol{n} = (\cos\theta, \sin\theta)$ is the director. The dynamical equations of active nematics in the dimensionless form read [17]

$$(\partial_t + \boldsymbol{v}\cdot\boldsymbol{\nabla})\,\boldsymbol{v} = \frac{1}{\mathrm{Re}}\nabla^2\boldsymbol{v} - \boldsymbol{\nabla}p + \boldsymbol{\nabla}\cdot\underline{\boldsymbol{\sigma}} \tag{3.1}$$

and

$$(\partial_t + \boldsymbol{v}\cdot\boldsymbol{\nabla})\,\underline{\boldsymbol{Q}} = \lambda S\underline{\boldsymbol{u}} + \underline{\boldsymbol{Q}}\cdot\underline{\boldsymbol{\omega}} - \underline{\boldsymbol{\omega}}\cdot\underline{\boldsymbol{Q}} + \gamma^{-1}\underline{\boldsymbol{H}}. \tag{3.2}$$

Here, $\boldsymbol{v}$ is the normalized flow velocity which satisfies the incompressibility condition $\boldsymbol{\nabla} \cdot \boldsymbol{v} = 0$, p is the pressure and $\underline{\boldsymbol{\sigma}}$ is the stress tensor. The flow properties are characterized by the Reynolds number Re, the flow alignment parameter λ, and the rotational viscosity γ, and $u_{ij} = (\partial_i v_j + \partial_j v_i)/2$ and $\omega_{ij} = (\partial_i v_j - \partial_j v_i)/2$ are the symmetric and antisymmetric parts of velocity gradient tensor, respectively. Hereafter we call $\omega = \omega_{xy}$ the vorticity. We assume $0 < \lambda < 1$; a positive value of λ corresponds to elongated or rod-like elements and $|\lambda| < 1$ to the flow-tumbling regime where no stable director orientation exists in a uniform shear flow [30, 41]. The molecular field H_{ij} is the symmetric and traceless part of $-\delta F/\delta Q_{ij}$, and is obtained from the Landau-de Gennes free energy [30]

$$F = \int f \mathrm{d}^2 r, \tag{3.3}$$

$$f = \frac{A}{2}\mathrm{Tr}\left(\underline{\boldsymbol{Q}} : \underline{\boldsymbol{Q}}\right) + \frac{C}{4}\left(\mathrm{Tr}\left(\underline{\boldsymbol{Q}} : \underline{\boldsymbol{Q}}\right)\right)^2 + \frac{K}{2}\left(\nabla \underline{\boldsymbol{Q}}\right)^2 - \frac{1}{2}\boldsymbol{E} \cdot \underline{\boldsymbol{Q}} \cdot \boldsymbol{E}. \tag{3.4}$$

The first two terms of the free energy density control the magnitude of the scalar order parameter S. Note that the term proportional to $\mathrm{Tr}\,\underline{\boldsymbol{Q}}^3$ identically vanishes for the two-dimensional nematic order parameter. The third term is the Frank elastic energy under the one-constant approximation, and the fourth term describes the coupling to the quenched random field $\boldsymbol{E}$. The molecular field is obtained as

$$H_{xx} = -\left(2A + CS^2\right) Q_{xx} + 2K\nabla^2 Q_{xx} + \frac{1}{2}\left(E_x^2 - E_y^2\right). \tag{3.5}$$

$$H_{xy} = -\left(2A + CS^2\right) Q_{xy} + 2K\nabla^2 Q_{xy} + E_x E_y. \tag{3.6}$$

The stress tensor is the sum of the passive stress

$$\underline{\boldsymbol{\sigma}}^{\mathrm{e}} = -\lambda S \underline{\boldsymbol{H}} + \underline{\boldsymbol{Q}} \cdot \underline{\boldsymbol{H}} - \underline{\boldsymbol{H}} \cdot \underline{\boldsymbol{Q}}, \tag{3.7}$$

and the active stress

$$\underline{\boldsymbol{\sigma}}^{\mathrm{a}} = -\alpha \underline{\boldsymbol{Q}}. \tag{3.8}$$

We assume an extensile active stress and hence the activity parameter α is positive.

We model the quenched random field to be of the form

$$\underline{\boldsymbol{E}} = E_0 \boldsymbol{e}(\boldsymbol{r}) \tag{3.9}$$

where $\boldsymbol{e}(\boldsymbol{r}) = (\cos\theta_e, \sin\theta_e)$ is a random unit vector with its angle θ_e being a uniformly random number in $[0, 2\pi)$. We implement the random field on a square lattice with the grid size ξ_e, and choose the angle θ_e randomly at each grid point. Therefore, it satisfies

$$\langle \boldsymbol{e}(\boldsymbol{r}) \boldsymbol{e}(\boldsymbol{r}') \rangle = \frac{1}{2} \underline{\boldsymbol{I}}\, \delta_{\boldsymbol{r},\boldsymbol{r}'}, \tag{3.10}$$

where $\delta_{\boldsymbol{r},\boldsymbol{r}'}$ is the Kronecker delta for a lattice. For continuum description at a typical lengthscale much larger than ξ_e, it is convenient to replace it with the expression

$$\langle \boldsymbol{e}(\boldsymbol{r}) \boldsymbol{e}(\boldsymbol{r}') \rangle = \frac{1}{2} \xi_e^2 \delta(\boldsymbol{r} - \boldsymbol{r}'). \tag{3.11}$$

Note that both expressions give ξ_e^2 over the grid containing $\boldsymbol{r} = \boldsymbol{r}'$. We will call ξ_e the correlation length of the random field. The contributions of the random field and Frank elasticity to the free energy are estimated as $E_0^2 S_0$ and KS_0^2/l_Q^2, respectively, where S_0 is the typical magnitude of the scalar order parameter and l_Q is the correlation length of $\underline{\boldsymbol{Q}}$. The orientational correlation length becomes smaller for a stronger random field, and its lower bound is given by $l_Q \sim \xi_e$. Therefore, we define the effective disorder strength as

$$D_K = \frac{E_0^2 \xi_e^2}{K S_0}. \tag{3.12}$$

On the other hand, the contributions to the molecular field by the random field and the active stress are estimated as E_0^2 and α, respectively. Thus we are led to the other definition of the dimensionless disorder strength,

$$D_\alpha = \frac{E_0^2}{\alpha}. \tag{3.13}$$

3.2 Disorder-dominated regime

In the disorder dominated regime with $D_K \gg 1$ and $D_\alpha \gg 1$, the director will align with the local director and get frozen. In this case, we have approximately $\boldsymbol{n}(\boldsymbol{r}) = \boldsymbol{e}(\boldsymbol{r})$, $\underline{\boldsymbol{H}} = \boldsymbol{0}$ and $\underline{\boldsymbol{\sigma}}^{\mathrm{e}} = \boldsymbol{0}$ in the stationary state, and the Frank elastic term in the molecular field is negligible. Thus, from Eqs.(3.5),(3.6), the scalar order parameter satisfies

$$-S\left(2A + CS^2\right) + E_0^2 = 0, \tag{3.14}$$

the solution of which is identified with S_0. The nematic order parameter is given by

$$\underline{\boldsymbol{Q}}(\boldsymbol{r}, t) = S_0 \left[\boldsymbol{e}(\boldsymbol{r})\boldsymbol{e}(\boldsymbol{r}) - \frac{1}{2}\underline{\boldsymbol{I}}\right]. \tag{3.15}$$

Since the molecular field is balanced and vanishes in the steady state, the flow velocity is determined solely by the active stress. For Re $\ll 1$, the velocity field is obtained by dropping the terms on the left hand side of Eq.(3.1) as

$$0 = \frac{1}{\mathrm{Re}}\nabla^2 \boldsymbol{v} - \nabla p + \nabla \cdot \underline{\boldsymbol{\sigma}}^{\mathrm{a}}. \tag{3.16}$$

Solving (3.16) under the incompressibility condition and with (3.8), we obtain the velocity field in the Fourier representation,

$$\boldsymbol{v}^{\boldsymbol{k}} = -\alpha \mathrm{Re}\, \frac{\underline{\boldsymbol{I}} - \hat{\boldsymbol{k}}\hat{\boldsymbol{k}}}{k^2} \cdot \left(i\boldsymbol{k} \cdot \underline{\boldsymbol{Q}}^{\boldsymbol{k}}\right), \tag{3.17}$$

which gives the velocity structure factor

$$\begin{aligned} \Sigma_v(\boldsymbol{k}) &= \left\langle \left|\boldsymbol{v}^{\boldsymbol{k}}\right|^2 \right\rangle \\ &= \frac{(\alpha \mathrm{Re})^2}{k^2} \left(\left\langle \left|\hat{\boldsymbol{k}} \cdot \underline{\boldsymbol{Q}}^{\boldsymbol{k}}\right|^2 \right\rangle - \left\langle \left|\hat{\boldsymbol{k}} \cdot \underline{\boldsymbol{Q}}^{\boldsymbol{k}} \cdot \hat{\boldsymbol{k}}\right|^2 \right\rangle \right). \end{aligned} \tag{3.18}$$

The correlation function of the nematic order parameter reads from Eqs.(3.11,3.15) as

$$\left\langle Q_{ij}(\boldsymbol{r}) Q_{lm}(\boldsymbol{r}')\right\rangle = \frac{1}{4} S_0^2 \xi_e^2 \left(\delta_{il}\delta_{jm} + \delta_{im}\delta_{jl}\right) \delta(\boldsymbol{r} - \boldsymbol{r}'), \tag{3.19}$$

and accordingly

$$\left\langle Q_{ij}^{\boldsymbol{k}} Q_{lm}^{-\boldsymbol{k}} \right\rangle = \frac{1}{4} S_0^2 \xi_e^2 \left(\delta_{il}\delta_{jm} + \delta_{im}\delta_{jl} \right). \tag{3.20}$$

Substituting this into Eq.(3.18), we obtain

$$\Sigma_v(\boldsymbol{k}) = \frac{(\alpha \mathrm{Re} S_0 \xi_e)^2}{4k^2}. \tag{3.21}$$

The velocity correlation function in the real space is given by the inverse Fourier transform of $\Sigma_v(\boldsymbol{k})$ as

$$\langle \boldsymbol{v}(\boldsymbol{r}) \cdot \boldsymbol{v}(\boldsymbol{r}') \rangle = -\frac{(\alpha \mathrm{Re} S_0 \xi_e)^2}{8\pi} \ln|\boldsymbol{r} - \boldsymbol{r}'|. \tag{3.22}$$

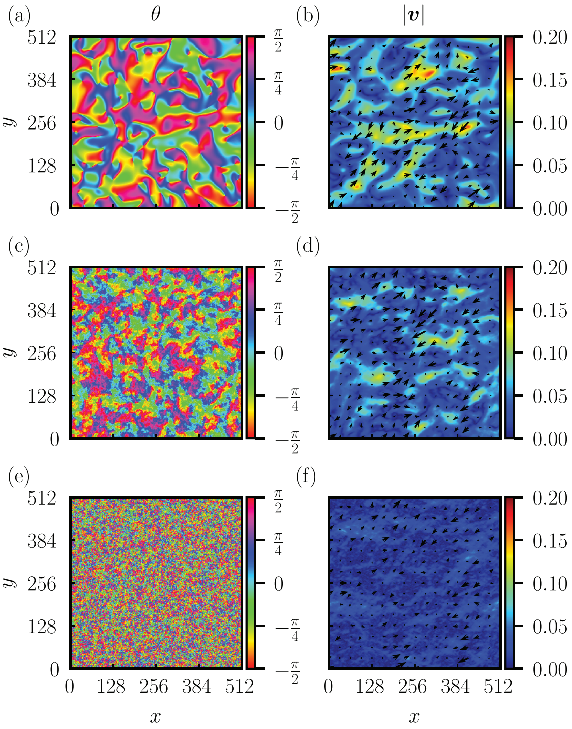

Figure 3.1: Snapshots of the director angle $\theta(x, y)$ in the first column and velocity $\boldsymbol{v}(x, y)$ (color map: magnitude, black arrows: vector field) in the second column, for the activity $\alpha = 0.2$ and the field strength (a)(b) $E_0 = 0$, (c)(d) $E_0 = 0.4$, and (e)(f) $E_0 = 0.7$.

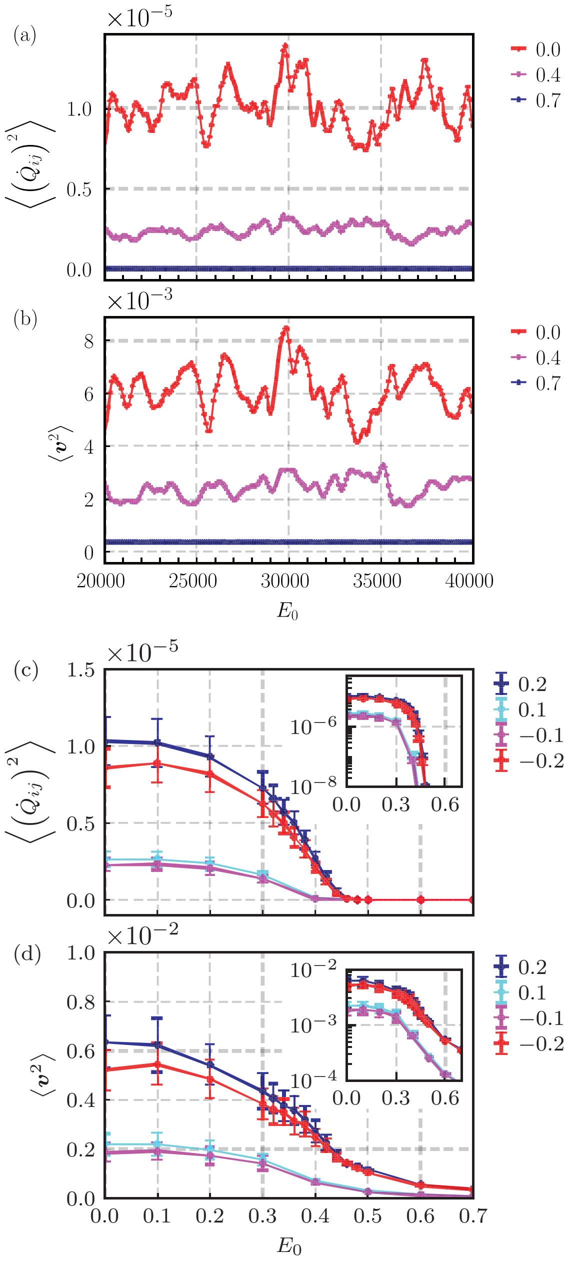

Figure 3.2: Mean square of the time-derivative of Q_{ij} and flow velocity $\boldsymbol{v}$ for $\alpha = 0.2$. (a),(b) Time evolution for a single sample, for $E_0 = 0.0, 0.4, 0.7$. (c),(d) Averages over time and 8 samples plotted versus the field strength E_0 and for $\alpha = 0.2, 0.1, -0.1, -0.2$. Error bars show the standard deviation. Insets: semi-log plots.

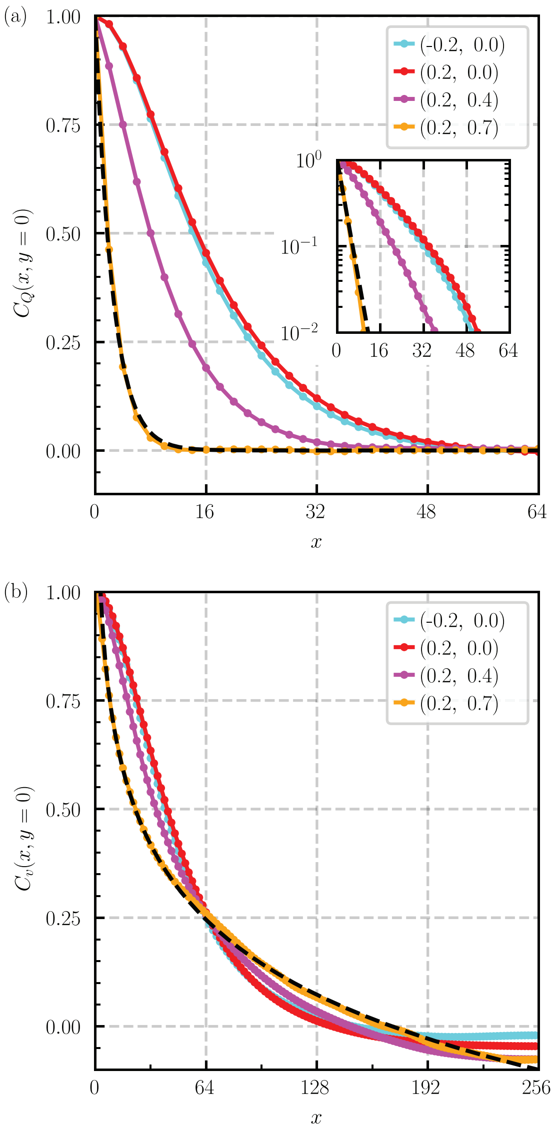

Figure 3.3: Correlation functions for $(\alpha, E_0) = (-0.2, 0.0)$,$(0.2, 0.0)$, $(0.2, 0.4)$, and $(0.2, 0.7)$. (a) Orientational correlation function $C_Q(r)$ (inset: semi-log plots). The dashed lines show the exponential function $\exp(-r/r_Q)$ with $r_Q = 2.5$. (b) Velocity correlation function. The dashed line shows the logarithmic function $-A\ln(r/r_v)$ with $A = 0.25$ and $r_v = 171$.

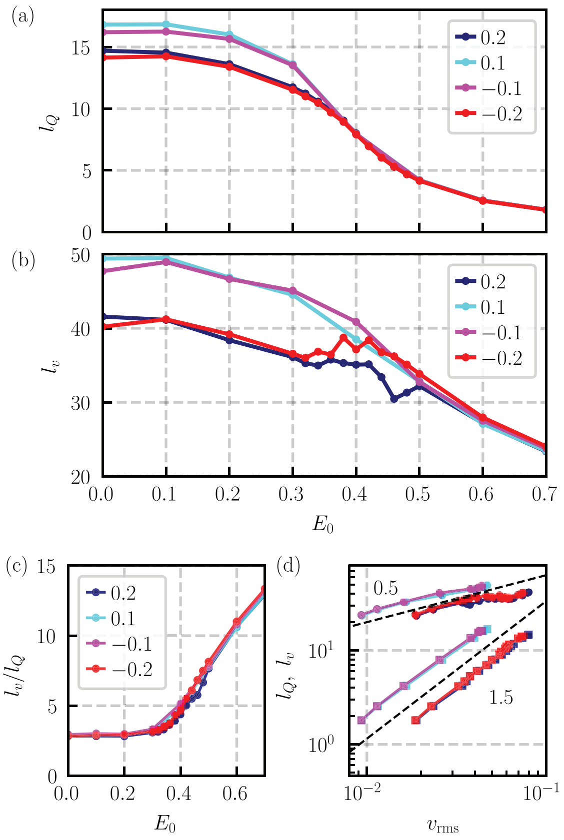

Figure 3.4: (a) The orientational correlation length l_Q and (b) velocity correlation length l_v as functions of E_0. (c) The ratio l_v/l_Q versus E_0.

3.3 Numerical simulation

We solved Eqs.(3.1,3.2) numerically on a square lattice with the fourth-order Runge–Kutta method. The incompressibility condition is handled by the simplified MAC method on a staggered lattice [96]. The main sublattice is used for the field variables $\underline{\boldsymbol{Q}}$, p, $\underline{\boldsymbol{\sigma}}$, $\underline{\boldsymbol{u}}$, $\underline{\boldsymbol{\omega}}$ and $\underline{\boldsymbol{H}}$, and the other two sublattices are assigned to v_x and v_y. The calculation is performed on a $N_x \times N_y$ lattice with the grid size $\Delta x = \Delta y = 2$ and the step time increment $\Delta t = 0.01$. We assumed periodic boundary conditions and used Fast Fourier Transform to solve the Laplace equation for the pressure at each time step. For the numerical analysis, we used the parameter values

$$A = -0.16,\ C = 0.89,\ K = 1, \tag{3.23}$$

$$\lambda = 0.1,\ \mathrm{Re} = 0.1,\ \gamma = 10. \tag{3.24}$$

We varied the activity parameter α from -0.2 to 0.2 to study both extensile and contractile systems. The direction $\boldsymbol{e}(\boldsymbol{r})$ of the random field is randomly chosen at each grid point, which means $\xi_e = 2$. The field strength is varied in the range $0 \leq E_0 \leq 0.7$. The scalar order parameter in the passive ($\alpha = 0$) and stationary system is obtained from Eq.(3.14) as $S_0 \simeq 0.60$ for $E_0 = 0$ and increases with E_0. We confirmed that S does not increase above unity for the strongest random field studied ($E_0 = 0.7$). The defect core radius is given by $\xi = \sqrt{K/|A|} \simeq 2.5$. The balance between the activity and Frank elasticity defines the lengthscale $l_\alpha = \sqrt{K/|\alpha|}$, which reads $l_\alpha \simeq 2.2$ for $|\alpha| = 0.2$ and $l_\alpha \simeq 3.2$ for $|\alpha| = 0.1$. The system size is fixed to $N_x = N_y = 256$ so that $L = N_x \Delta x = N_y \Delta y = 512$. For the initial conditions, we set the velocity to zero and assumed small random fluctuations around zero for $\underline{\boldsymbol{Q}}(\boldsymbol{r}, 0)$, assuming a quench from the isotropic quiescent state. To be precise, the scalar order parameter and the director angle at each grid point are randomly chosen in the ranges $[0, 0.1]$ and $[0, 2\pi]$, respectively. We observed the total kinetic energy as a function of time to confirm that the system reached dynamical steady states, typically by $t = 10000$ for active turbulence states. We calculated the data over the time window $20000 < t \leq 40000$ with the time interval $t_0 = 100$, and took the ensemble average over 8 independent samples.

3.4 Spatial patterns and orientational freezing

In Fig. 3.1, we show the snapshots of the director angle $\theta(\boldsymbol{r}, t)$ and the vorticity $\omega(\boldsymbol{r}, t)$ in the dynamical steady states for $\alpha = 0.2$. For $E_0 = 0$, active turbulence containing topological defects and vortices are reproduced [Fig.3.1(a)(b)]. For $E_0 = 0.4$, the director pattern becomes jaggy while maintaining the characteristic large-scale structure of nematic defects. The velocity field is smoother but wiggly streams appear [Fig.3.1(c)(d)]. For $E = 0.7$, the director orientation becomes completely random, and the flow pattern obtains fibrous structures of various size and magnitude [Fig.3.1(e)(f)].

The dynamics slows down as we increase the field strength. In Fig. 3.2, we show the mean square of the time-derivative of the order parameter $\dot{Q}_{ij}$ and flow velocity. The time evolution of these quantities for $20000 < t \leq 40000$ is shown in Fig. 3.2(a),(b), for $\alpha = 0.2$ fixed and $E_0 = 0, 0.4$ and 0.7. They show large fluctuations around their mean values with a typical timescale $\sim 10^3$ for $E_0 = 0.0$. Both the mean values and fluctuations get smaller as E_0 is increased. For $E_0 = 0.7$, $\langle \dot{Q}_{ij}^2 \rangle$ vanishes while the velocity has a small and constant magnitude. These data justify the use of statistical data taken over the same time window to be shown in the rest of this paper. In Fig. 3.2(c),(d), we show the time-averaged values for $\alpha = 0.2$, 0.1, -0.1 and -0.2 as functions of E_0. We find that the extensile ($\alpha > 0$) and contractile ($\alpha < 0$) cases behave qualitatively similarly. Quantitatively, the extensile cases show $\sim 10-20\%$ larger values than the contractile cases with the same magnitude of $|\alpha|$, for both $\dot{Q}_{ij}^2$ and v^2 and for $E_0 \leq 0.4$. For $E_0 \geq 0.5$, the differences between them become very small. The ratio of these quantities between $\alpha = 0.2$ and $\alpha = 0.1$ are about 4 for $\dot{Q}_{ij}^2$ and 3 for v^2 at $E_0 = 0$. For $\alpha = 0.2$, $\dot{Q}_{ij}^2$ shows a sharp drop to below 10^{-6} at $E_0 = 0.44$, while a similar drop is observed at a smaller value of E_0 for $\alpha = 0.1$; see the semi-log plots in the inset of Fig. 2(c). Hereafter, we will focus on the extensile case $\alpha = 0.2$. The director dynamics completely freezes at $E_0 \approx 0.5$. On the other hand, the mean square velocity decreases only gradually as we increase the randomness. Its decay above $E_0 = 0.44$ is slower than that of the orientational order parameter. For $E_0 = 0.7$, the strongest field we studied, the mean square velocity still remains at about 6 percent of its value at $E_0 = 0$. Note that the effective disorder strengths are $D_K \simeq 0.97$ and $D_\alpha \simeq 0.96$ for $E_0 = 0.44$, which are both close to unity. Therefore, it would be reasonable to discriminate the medium and strong disorder regimes at this value of E_0.

3.5 Spatial correlation functions and correlation lengths

In Fig. 3.3, we show the spatial correlation functions for the orientational order parameter and flow velocity, which are defined by

$$C_Q(\boldsymbol{r}) = \frac{\langle \underline{\boldsymbol{Q}}(\boldsymbol{r}+\boldsymbol{r}',t) : \underline{\boldsymbol{Q}}(\boldsymbol{r}',t)\rangle}{\langle \underline{\boldsymbol{Q}}(\boldsymbol{r}',t)^2\rangle} \tag{3.25}$$

and

$$C_v(\boldsymbol{r}) = \frac{\langle \boldsymbol{v}(\boldsymbol{r}+\boldsymbol{r}',t) \cdot \boldsymbol{v}(\boldsymbol{r}',t)\rangle}{\langle \boldsymbol{v}(\boldsymbol{r}',t)^2\rangle}, \tag{3.26}$$

respectively, where $\langle\cdots\rangle$ indicates averages over $\boldsymbol{r}'$ and t, and 8 independent samples. By symmetry, the correlation functions are functions of the distance only. We show their profiles along the x-axis in Fig. 3.3. Confirming again that the extensile case ($\alpha = 0.2$) and contractile case ($\alpha = -0.2$) show similar behaviors for $E_0 = 0.0$, we will focus on the extensile case in the following, and vary the field strength as $E_0 = 0.0$, 0.4, and 0.7. The orientational correlation function $C_Q(r)$ is a monotonically decreasing function with a positive curvature [Fig. 3.3(a)]. For $E_0 = 0.7$, it is fitted by the exponential function $C_Q(r) = \exp(-r/r_Q)$ with $r_Q = 2.5$. The semi-logarithmic plot in the inset of Fig. 3.3(a) shows that the exponential decay also holds for the medium disorder case $E_0 = 0.4$, up to $r \approx 30$, while the decay is faster than exponential for $E_0 = 0$ as seen from the upper-convex curve in the semi-log plot. Furthermore, for $E_0 = 0.7$, we confirmed that the orientational correlation functions for $-0.2 \le \alpha \le 0.2$ closely match with each other; the data are not shown as they are not distinguishable at the scale of Fig. 3.3(a).

The velocity correlation function decays more slowly than the orientational one, and turns negative at $r \sim L/4$ for $E_0 = 0$ and at $r \sim L/3$ for $E_0 = 0.7$ [Fig. 3.3(b)]. It is monotonically decreasing up to $r = 0.5L$, but should converge to zero for $r \to \infty$. The function has a negative curvature in a narrow range near $r = 0$, which becomes narrower for a larger field strength. For $E_0 = 0.7$, it is nicely fitted by the logarithmic function $C_v(r) = -A\ln(r/r_v)$ with $A = 0.25$ and $r_v = 171$, in the range $2 < r < r_v$. In addition, for the system size $L = 256$ system, we found that the same fitting gives $r_v = 78$, which suggests that r_v is determined by and proportional to system size.

We define the correlation lengths l_Q and l_v by $C_Q(l_Q)= 1/2$ and $C_v(l_v) = 1/2$, respectively. They are plotted in Fig. 3.4(a)(b) as functions of the field strength. The orientational correlation length shows a rapid decay between $E_0 = 0.2$ and 0.5. The decay of the velocity correlation length is slower, and shows large fluctuations in the transition region $0.3 < E_0 < 0.5$ due to sample dependence. The ratio l_v/l_Q plotted in Fig. 3.4(c) increases to 13 at $E_0 = 0.7$ from 2.8 at $E_0 = 0$.

3.6 Discussion

We found a marked contrast between the orientational and flow properties, which are summarized as follows: (i) Dynamics of the orientational order parameter is completely frozen at and above a critical random field strength, while the flow velocity only gradually decreases as the randomness is increased and remains finite in the strong disorder limit. (ii) The spatial correlation of the orientational order parameter is short-ranged and exhibits exponential decay for strong disorder, while the flow velocity has a long-range correlation with a logarithmic decay for strong disorder. We have also compared the extensile and contractile systems, and found only a small difference between the two if the magnitude of activity $|\alpha|$ is the same. The difference becomes negligible for strong disorder.

The exponential decay of the orientational correlation function $C_Q(r)$ in the strong disorder regimes [Fig. 3.3(a)] is in agreement with the previous result on 2D random-field nematics [83]. This suggests that the director texture is determined by balance between the random field and Frank elasticity, and is little affected by the active flow. This is supported by the fact that $C_Q(r)$ for $-0.2 \leq \alpha \leq 0.2$ are not indistinguishable from each other for $E_0 = 0.7$. Earlier studies on the random-field XY model found correlation decay faster than exponential in two dimensions [102, 103]. The difference is attributed to the different symmetry of random anisotropy in nematics and the XY model [83]. Without the randomness, the orientational correlation function decays faster than exponential as seen in Fig. 3.3(a). In this case, the correlation functions are characterized by the vortex size [47], and the velocity correlation function $C_v(r)$ has a negative curvature at short distances, as seen in Fig. 3.3(b) and in agreement with the analytical result [47]. As we increase the random field, the range with a negative curvature shrinks and the velocity correlation function is better approximated by the logarithmic function. This is in agreement with the analytical result for the strong disorder [Eq.(3.22)], and reflects the structure of the Green function of the Stokes equation in two dimensions. In three dimensions, the velocity correlation function should decay as $1/r$ in the strong disorder limit. Note also that the effective disorder strengths are $D_K \simeq 2.0$ and $D_\alpha \simeq 2.5$ for $E_0 = 0.7$ and $\alpha = 0.2$, and are not large enough to ensure the constantness of the scalar order parameter. However, the orientational correlation length $r_Q = 2.5$ obtained at the strongest disorder is close to the random field correlation length ξ_e. The logarithmic function for the velocity correlation also fits to the numerical results with errors within ±6% over the range $4 \leq r \leq 110$, where $C_v(r) \geq 0.1$. The error increases to 16% at $r = \xi_e = 2$ due to the discreteness of the lattice. These results confirm the validity of the analytical results obtained by the continuum approximation over a wide distance range.

The dependences of the orientational and velocity correlation lengths on the field strength are also in marked contrast. For weak disorder, both lengths are proportional to the vortex size and the ratio l_v/l_Q is small. For strong disorder, the velocity correlation decays monotonically even when the orientational correlation length is converging to constant, and thus l_v/l_Q diverges in the strong disorder limit. The slowing down of the increase of l_v/l_Q in the strong disorder regime [Fig. 3.4(b)] is explained by facts that the l_Q has a lower bound determined by the defect core size, and that l_v has a upper bound determined by the system size. (Note that l_v cannot exceed $L/2$ due to the periodic boundary condition.)

Finally, we consider the competition between the active flow and random field. The flow-aligning effect on the nematic order parameter is represented by the term $\lambda S\underline{\boldsymbol{u}}$ in Eq. (3.2), the magnitude of which is estimated as $\lambda S_0 v_{\mathrm{rms}}/l_v$. The contribution of the random field in the term $\gamma^{-1}\underline{\boldsymbol{H}}$ is estimated as $\gamma^{-1}E_0^2 S_0$. Averaging it over the area l_Q^2 of an orientationally correlated region, which contains $N \sim (l_Q/\xi_e)^2$ sites, we get $\gamma^{-1}E_0^2 S_0/\sqrt{N} \sim \gamma^{-1}E_0^2 S_0 \xi_e/l_Q$. Thus the ratio between the flow-aligning and random-field terms is estimated as $\gamma\lambda v_{\mathrm{rms}} l_Q/(E_0^2 l_v \xi_e)$. In our simulation, this ratio becomes 0.33 for $E_0 = 0.2$ and $\alpha = 0.2$, which confirms the observation that the active flow has a minor effect in the medium ($0.2 < E_0 < 0.44$) and strong ($E_0 > 0.44$) disorder regimes. It is also consistent with the fact that the mean flow velocity and correlation lengths start to decrease around $E_0 = 0.2$.

In summary, quenched disorder introduces unique twists into the physics of active nematics. For strong disorder, the director texture is frozen and determined by the balance between the randomness and Frank elasticity, while active flow with long-range correlation remains and facilitates material transport. We hope that the present work stimulates experimental studies on the flow properties of cellular and subcellular systems with orientational order.

Chapter 4

Active solids with alignment interaction

The content of this chapter is adapted from [86] (Y. Kinoshita, N. Uchida, and A. M. Menzel, “Collective excitations in active solids featuring alignment interactions”, The Journal of Chemical Physics 162, 054906 (2025)), with the permission of AIP Publishing. © (2025) AIP Publishing.

With increasing emphasis on the study of active solids, the features of these classes of nonequilibrium systems and materials beyond their mere existence shift into focus. One concept of active solids addresses them as active, self-propelled units that are elastically linked to each other. The emergence of orientationally ordered, collectively moving states in such systems has been demonstrated. We here Y. Kinoshita, N. Uchida, and A. M. Menzel, “Collective excitations in active solids featuring alignment interactions”, The Journal of Chemical Physics 162, 054906 (2025)analyze the excitability of such collectively moving elastic states. To this end, we determine corresponding fluctuation spectra. They indicate that collectively excitable modes exist in the migrating solid. Differences arise when compared to those of corresponding passive solids. We provide evidence that the modes of excitation associated with the intrinsic fluctuations are related to corresponding modes of entropy production. Overall, by our investigation, we hope to stimulate future experimental studies that focus on excitations in active solids.

The remaining parts are structured as follows. In Sec. 4.1, we introduce the model for active Brownian objects and the alignment interaction resulting from the action of the connecting elastic springs. We derive the fluctuation spectrum in the moving state from the linearized equations of motion in Sec. 4.2. Next, we calculate the rate of entropy production in Sec. 4.3 based on the results obtained in Sec. 4.2. Afterwards, in Sec. 4.4, we report our results from numerical simulations of the original equations of motion introduced in Sec. 4.1, which match well with the analytical solutions. Finally, our conclusions are stated in Sec. 4.5.

4.1 Theoretical description

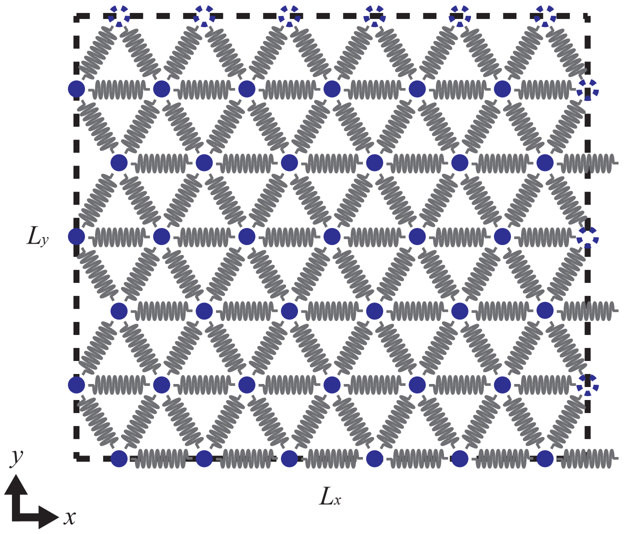

Figure 4.1: Schematic illustration of the system in its undeformed rest state. We impose periodic boundary conditions at each boundary. Colored objects are connected by springs. White objects are identical to the ones on the opposite side of the calculation box due to the boundary conditions.

To set up the active elastic solid, we consider N identical active Brownian objects, each of mass m, pairwise connected by linear springs to form a two-dimensional hexagonal lattice; see Fig 4.1. The time evolution of the position $\boldsymbol{r}_i(t)$ and velocity $\boldsymbol{v}_i(t)$ of the ith object ($i = 1, ..., N$) is quantified by the translational equations of motion

$$\dot{\boldsymbol{r}}_i(t) = \boldsymbol{v}_i(t), \tag{4.1}$$

$$\begin{aligned} m\dot{\boldsymbol{v}}_i(t) = &- \gamma_r \boldsymbol{v}_i(t) - \boldsymbol{\nabla}_{\boldsymbol{r}_i} U(\{\boldsymbol{r}\}) + F_0 \boldsymbol{e}_i \\ &+ \sqrt{2\gamma_r k_B T_r}\, \boldsymbol{\eta}_i(t). \end{aligned} \tag{4.2}$$

In these expressions, dots mark time derivatives, and γ_r is the coefficient of translational friction. T_r is an effective temperature and k_B represents Boltzmann's constant. $U(\{\boldsymbol{r}\})$ includes the overall potential due to the Hookean springs introduced between neighboring objects in the undeformed ground state of the lattice. We assume periodic boundary conditions so that each object is permanently linked by elastic springs to its six surrounding initially nearest neighbors in our two-dimensional hexagonal lattice. $\{\boldsymbol{r}\}$ is a short notation for the tuple of all positional vectors $\boldsymbol{r}_i$ ($i = 1, ..., N$). In our case, the potential reads

$$U(\{\boldsymbol{r}\}) = \frac{1}{2} K \sum_{(i,j)} \left(\left| \boldsymbol{r}_i - \boldsymbol{r}_j \right| - a \right)^2 . \tag{4.3}$$

Here, K quantifies the identical elastic stiffness of each spring, a denotes the natural length of each spring in the ground state, and (i, j) denotes all pairs of objects permanently linked by springs, without double-counting. Moreover, each object self-propels with the identical strength of active driving F_0 into the individual direction of the active driving force $\boldsymbol{e}_i = (\cos\theta_i, \sin\theta_i)^T$, where ^{T} marks the transpose. θ_i is an angle in the two-dimensional x-y-plane measured from the x-axis. Finally, $\boldsymbol{\eta}_i(t)$

represents the influence of a Gaussian-distributed white stochastic force. It has zero mean and satisfies $\langle \eta_{i,\alpha}(t)\eta_{j,\beta}(t')\rangle = \delta_{ij}\delta_{\alpha\beta}\delta(t-t')$, $\alpha,\beta \in \{x,y\}$ in two dimensions. δ_{ij} marks the Kronecker delta and $\delta(t-t')$ marks the Dirac delta function.

Equations (4.1) and (4.2) for translational motion are supplemented by the equations of rotational motion for the direction of self-propulsion $\boldsymbol{e}_i$ of each object i ($i = 1, ..., N$). Introducing the angular frequency ω_i of each object i, these equations read

$$\dot{\theta}_i = \omega_i, \tag{4.4}$$

$$\begin{aligned} I\dot{\omega}_i =& -\gamma_\theta\omega_i + \zeta|\boldsymbol{v}_i|\sin(\phi_i-\theta_i) \\ &+ \sqrt{2\gamma_\theta k_B T_\theta}\,\eta_{\theta,i}(t). \end{aligned} \tag{4.5}$$

Here, I plays the role of the identical moment of inertia of each object, γ_θ is an identical coefficient of rotational friction of each object, while ζ sets the identical strength of orientational alignment between the orientational angle θ_i of the direction of self-propulsion $\boldsymbol{e}_i$ of the object i and the orientational angle ϕ_i of the velocity [61, 63]. ϕ_i is not only affected by active driving but also by the elastic forces. We consider ζ to be positive, which means the direction of self-driving tends to orient along the direction of the elastic force. $\eta_{\theta,i}(t)$ includes the effect of a white Gaussian stochastic torque with the effective temperature T_θ. Its mean vanishes and it satisfies $\langle \eta_{\theta,i}(t)\eta_{\theta,j}(t')\rangle = \delta_{ij}\delta(t-t')$.

We rescale lengths according to $\boldsymbol{r} = a\hat{\boldsymbol{r}}$ and times according to $t = \gamma_r\hat{t}/K$. Hats denote dimensionless quantities. Thus, we arrive at the dimensionless coupled equations of motion

$$\dot{\hat{\boldsymbol{r}}}_i = \hat{\boldsymbol{v}}_i, \tag{4.6}$$

$$\begin{aligned} \tau_v\dot{\hat{\boldsymbol{v}}}_i =& -\hat{\boldsymbol{v}}_i - \sum_{j\in(i,j)} \left(|\hat{\boldsymbol{r}}_i-\hat{\boldsymbol{r}}_j|-1\right)\frac{\hat{\boldsymbol{r}}_i-\hat{\boldsymbol{r}}_j}{|\hat{\boldsymbol{r}}_i-\hat{\boldsymbol{r}}_j|} \\ &+ \alpha\boldsymbol{e}_i + \sqrt{2D_r}\hat{\boldsymbol{\eta}}_i(\hat{t}), \end{aligned} \tag{4.7}$$

$$\dot{\theta}_i = \hat{\omega}_i, \tag{4.8}$$

$$\tau_\theta\dot{\hat{\omega}}_i = -\hat{\omega}_i + \xi\hat{v}_i\sin(\phi_i-\theta_i) + \sqrt{2D_\theta}\hat{\eta}_{\theta,i}(\hat{t}). \tag{4.9}$$

In these expressions, we define $\tau_v = mK/\gamma_r^2$, $D_r = k_BT_r/a^2K$, $\alpha = F_0/Ka$, $\tau_\theta = IK/\gamma_r\gamma_\theta$, $\xi = \zeta a/\gamma_\theta$, and $D_\theta = k_BT_\theta\gamma_r/K\gamma_\theta$.

$\hat{\eta}_{\theta,i}(t)$ is a white Gaussian stochastic process of zero mean and unit variance. Moreover, we omit the hat to simplify notation. We set $\tau_v = \tau_\theta = 0$ because we only consider the overdamped situation for simplicity, in line with experiments and considerations on a colloidal scale. In addition, from now on when evaluating the formulas, we set $D_r = 0.001$ and $D_\theta = 0.001$.

4.2 Fluctuation spectra in the collectively migrating state

As demonstrated earlier [66], the system shows an ordered state of all objects moving collectively on average in the same direction, while maintaining a hexagonal lattice structure. Let us denote the angle of the global direction of migration as θ_0 and the overall speed of the lattice structure as V. We relate

V and θ_0 to the polar order parameter

$$\boldsymbol{P} = \frac{1}{N}\sum_{i}^{N} \boldsymbol{e}(\theta_i) \tag{4.10}$$

through the equation $V\boldsymbol{e}(\theta_0) = \alpha\boldsymbol{P}$. For vanishing noise, the global speed V in the perfectly ordered state matches the speed of self-propulsion of each object. In this case, $V = \alpha$ because $|\boldsymbol{P}| = 1$. The speed V decreases with increasing diffusion constants, accompanied by a decreasing degree of polar orientational order $|\boldsymbol{P}|$. According to the large-number theorem, the fluctuations of both the speed and the angle of collective motion tend to zero in the limit of large system sizes. In this limit, the global velocity of the system is the same as the averaged velocity of each object, $\langle \dot{\boldsymbol{r}}_i \rangle = V\boldsymbol{e}(\theta_0)$ for all $i = 1, ..., N$. Similarly, we register for the angles θ_i that $\langle \theta_i \rangle = \theta_0$.

Next, we denote each reference position as $\boldsymbol{x}_i^{(0)}(t) = (x_i^{(0)}(t), y_i^{(0)}(t))^T$ for $i = 1, ..., N$. It is obtained from the starting position in the perfect hexagonal lattice structure $\boldsymbol{x}_i^{(0)}(t = 0) = \boldsymbol{x}_i^{(0)}$ via $\boldsymbol{x}_i^{(0)}(t) = \boldsymbol{x}_i^{(0)} + V\boldsymbol{e}(\theta_0)t$.

We assume that the deviations from this idealized situation induced by stochastic fluctuations as quantified by the diffusion constants are small. In other words, the diffusion constants D_r and D_θ are low in magnitude. To this end, we introduce the displacements $\boldsymbol{u}_i(t) = \boldsymbol{r}_i(t) - \boldsymbol{x}_i^{(0)}(t)$ and the deviations in the individual angles of self-propulsion $\delta\theta_i(t) = \theta_i(t) - \theta_0$. Therefore,

$$\boldsymbol{r}_i(t) = \boldsymbol{x}_i^{(0)} + V\boldsymbol{e}(\theta_0)t + \boldsymbol{u}_i(t), \tag{4.11a}$$

$$\theta_i(t) = \theta_0 + \delta\theta_i(t). \tag{4.11b}$$

The elastic potential $\hat{U}(\{\boldsymbol{u}\})$, where $\{\boldsymbol{u}\}$ summarizes all $\boldsymbol{u}_i$ ($i = 1, ..., N$) and $\boldsymbol{x}_{ij}^{(0)} = \boldsymbol{x}_i^{(0)} - \boldsymbol{x}_j^{(0)}$, is approximated to second order in $\boldsymbol{u}_{ij} = \boldsymbol{u}_i - \boldsymbol{u}_j$,

$$\begin{aligned} \hat{U}(\{\boldsymbol{u}\}) &= \frac{1}{2}\sum_{(i,j)} \left(|\boldsymbol{x}_{ij}^{(0)} + \boldsymbol{u}_{ij}| - 1\right)^2 \\ &\approx \frac{1}{2}\sum_{(i,j)} \left(\boldsymbol{x}_{ij}^{(0)} \cdot \boldsymbol{u}_{ij}\right)^2 . \end{aligned} \tag{4.12}$$

Thus, the elastic forces are approximated to first order in $\boldsymbol{u}$ as

$$\boldsymbol{F}_i \approx -\sum_{j\in(i,j)} \left(\boldsymbol{x}_{ij}^{(0)} \cdot \boldsymbol{u}_{ij}\right)\boldsymbol{x}_{ij}^{(0)} = -\sum_{j\in(i,j)} \underline{\boldsymbol{M}}_{ij} \cdot \boldsymbol{u}_{ij}, \tag{4.13}$$

where, together with the parameterization $\boldsymbol{x}_{ij}^{(0)} = \left(x_{ij}^{(0)}, y_{ij}^{(0)}\right)^T$, the matrix $\underline{\boldsymbol{M}}_{ij}$ is given by

$$\underline{\boldsymbol{M}}_{ij} = \begin{pmatrix} \left(x_{ij}^{(0)}\right)^2 & x_{ij}^{(0)} y_{ij}^{(0)} \\ x_{ij}^{(0)} y_{ij}^{(0)} & \left(y_{ij}^{(0)}\right)^2 . \end{pmatrix}. \tag{4.14}$$

Using these abbreviations, the linearized equation for translational motion following from Eq. (4.7) becomes

$$\begin{aligned}\dot{\boldsymbol{u}}_i = &- \sum_{j\in(i,j)} \underline{\boldsymbol{M}}_{ij} \cdot \boldsymbol{u}_{ij} + (\alpha - V)\, \boldsymbol{e}(\theta_0) \\ &+ \alpha \begin{pmatrix} -\sin\theta_0 \\ \cos\theta_0 \end{pmatrix} \delta\theta_i + \boldsymbol{\eta}_i(t). \end{aligned} \tag{4.15}$$

We may conclude that this equation simplifies in the limit of large numbers of linked objects N. For demonstration, we expand the polar orientational order parameter as

$$\begin{aligned}\boldsymbol{P} =& \frac{1}{N} \sum_{i=1}^{N} \boldsymbol{e}\,(\theta_0 + \delta\theta_i) \\ \approx& \frac{1}{N} \sum_{i=1}^{N} \left(\boldsymbol{e}\,(\theta_0) + \boldsymbol{e}'(\theta_0)\,\delta\theta_i\right) \\ =& \frac{1}{N} \sum_{i=1}^{N} \boldsymbol{e}\,(\theta_0) + \boldsymbol{e}'(\theta_0)\,\frac{1}{N} \sum_{i=1}^{N} \delta\theta_i \\ =& 1 + \boldsymbol{e}'(\theta_0)\,\frac{1}{N} \sum_{i=1}^{N} \delta\theta_i. \end{aligned}$$

The second term of the last expression becomes zero in the limit of large numbers of linked objects $N \longrightarrow \infty$. Then, assuming that the globally orientationally ordered state exists, $\boldsymbol{P}$ satisfies the equality $|\boldsymbol{P}| = 1$ to linear order. We numerically confirm the validity of this approximation for the considered scenario in Sec 4.4. As a consequence, $V\boldsymbol{e}(\theta_0) = \alpha \boldsymbol{P}$ for $N \longrightarrow \infty$ implies $V = \alpha$. Accordingly, the second term on the right-hand side of Eq. (4.15) becomes zero.

Thus, the coupled linearized equations of motion are derived from Eqs. (4.7) and (4.9) as

$$\begin{aligned}\dot{\boldsymbol{u}}_i =& - \sum_{j\in(i,j)} \underline{\boldsymbol{M}}_{ij} \cdot \boldsymbol{u}_{ij} + \alpha \begin{pmatrix} -\sin\theta_0 \\ \cos\theta_0 \end{pmatrix} \delta\theta_i \\ &+ \sqrt{2D_r}\boldsymbol{\eta}_i(t), \end{aligned} \tag{4.16}$$

$$\begin{aligned}\delta\dot{\theta}_i =& -\xi \sum_{j\in(i,j)} \left[\cos\theta_0 (\underline{\boldsymbol{M}}_{ij} \cdot \boldsymbol{u}_{ij})_y - \sin\theta_0 (\underline{\boldsymbol{M}}_{ij} \cdot \boldsymbol{u}_{ij})_x\right] \\ & - \xi \sin\theta_0 \sqrt{2D_r}\eta_{x,i}(t) + \xi \cos\theta_0 \sqrt{2D_r}\eta_{y,i}(t) \\ & + \sqrt{2D_\theta}\eta_{\theta,i}(t). \end{aligned} \tag{4.17}$$

We apply the Fourier series in space and combine Eqs. (4.16) and (4.17) into one equation as

$$\dot{\boldsymbol{y}}_{\boldsymbol{k}} = - \underline{\boldsymbol{\Gamma}}_{\boldsymbol{k}}^{(xy)} \cdot \boldsymbol{y}_{\boldsymbol{k}} + \underline{\boldsymbol{D}}^{(xy)} \cdot \boldsymbol{\eta}_{\boldsymbol{k}}(t). \tag{4.18}$$

Here, the stochastic variables are combined into one vector $\boldsymbol{y}_{\boldsymbol{k}} = (u_{x,\boldsymbol{k}}, u_{y,\boldsymbol{k}}, \delta\theta_{\boldsymbol{k}})^T$. In Appendix C, we include the conventions that we employ for Fourier transformation in time and Fourier series in space. The coefficients on the right-hand sides of the equations are summarized by the matrices

$$\underline{\boldsymbol{\Gamma}}_{\boldsymbol{k}}^{(xy)} = \begin{pmatrix} M_{xx,\boldsymbol{k}} & M_{xy,\boldsymbol{k}} & \alpha \sin\theta_0 \\ M_{yx,\boldsymbol{k}} & M_{yy,\boldsymbol{k}} & -\alpha\cos\theta_0 \\ \xi(M_{yx,\boldsymbol{k}}\cos\theta_0 - M_{xx,\boldsymbol{k}}\sin\theta_0) & \xi(M_{yy,\boldsymbol{k}}\cos\theta_0 - M_{xy,\boldsymbol{k}}\sin\theta_0) & 0 \end{pmatrix}, \tag{4.19}$$

and

$$\underline{\boldsymbol{D}}^{(xy)} = \begin{pmatrix} \sqrt{2D_r} & 0 & 0 \\ 0 & \sqrt{2D_r} & 0 \\ -\xi\sin\theta_0\sqrt{2D_r} & \xi\cos\theta_0\sqrt{2D_r} & \sqrt{2D_\theta} \end{pmatrix}. \tag{4.20}$$

We define these expressions $\boldsymbol{\eta}_{\boldsymbol{k}}(t) = (\eta_{x,\boldsymbol{k}}(t), \eta_{y,\boldsymbol{k}}(t), \eta_{\theta,\boldsymbol{k}}(t))^T$ as the vector of the stochastic contributions. The definition of the matrix $\underline{\boldsymbol{M}}_{\boldsymbol{k}}$ is elucidated in Appendix D. Explicitly, its components read

$$\underline{\boldsymbol{M}}_{\boldsymbol{k}} = \begin{pmatrix} M_{xx,\boldsymbol{k}} & M_{xy,\boldsymbol{k}} \\ M_{xy,\boldsymbol{k}} & M_{yy,\boldsymbol{k}} \end{pmatrix}, \tag{4.21}$$

where

$$M_{xx,\boldsymbol{k}} = 3 - 2\cos(k_x) - \frac{1}{2}\cos\left(\frac{1}{2}k_x + \frac{\sqrt{3}}{2}k_y\right) - \frac{1}{2}\cos\left(\frac{1}{2}k_x - \frac{\sqrt{3}}{2}k_y\right) \tag{4.22a}$$

$$M_{xy,\boldsymbol{k}} = -\frac{\sqrt{3}}{2}\cos\left(\frac{1}{2}k_x + \frac{\sqrt{3}}{2}k_y\right) + \frac{\sqrt{3}}{2}\cos\left(\frac{1}{2}k_x - \frac{\sqrt{3}}{2}k_y\right) \tag{4.22b}$$

$$M_{yy,\boldsymbol{k}} = 3 - \frac{3}{2}\cos\left(\frac{1}{2}k_x + \frac{\sqrt{3}}{2}k_y\right) - \frac{3}{2}\cos\left(\frac{1}{2}k_x - \frac{\sqrt{3}}{2}k_y\right) \tag{4.22c}$$

From the symmetry of the cosine function, we infer $\underline{\boldsymbol{M}}_{\boldsymbol{k}} = \underline{\boldsymbol{M}}_{-\boldsymbol{k}}$, which reflects the inversion symmetry of the system. In addition, $\underline{\boldsymbol{M}}_{\boldsymbol{k}}$ itself is symmetric.

To simplify our considerations, we rotate the coordinate frame in Eq. (4.18) by θ_0. The rotation matrix is defined by

$$\underline{\boldsymbol{R}}(\theta) = \begin{pmatrix} \cos\theta & -\sin\theta & 0 \\ \sin\theta & \cos\theta & 0 \\ 0 & 0 & 1 \end{pmatrix}. \tag{4.23}$$

Through rotation by θ_0 in an anticlockwise direction, we obtain $\boldsymbol{z}_{\boldsymbol{k}} = (u_{\parallel,\boldsymbol{k}}, u_{\perp,\boldsymbol{k}}, \delta\theta_{\boldsymbol{k}})^T$ and $\boldsymbol{\eta}_{\boldsymbol{k}}^{(\theta_0)} = (\eta_{\parallel,\boldsymbol{k}}(t), \eta_{\perp,\boldsymbol{k}}(t), \eta_{\theta,\boldsymbol{k}}(t))^T$ via

$$\boldsymbol{y}_{\boldsymbol{k}} = \underline{\boldsymbol{R}}(\theta_0)\cdot\boldsymbol{z}_{\boldsymbol{k}}, \qquad \boldsymbol{\eta}_{\boldsymbol{k}} = \underline{\boldsymbol{R}}(\theta_0)\cdot\boldsymbol{\eta}_{\boldsymbol{k}}^{(\theta_0)}. \tag{4.24}$$

Hereafter, we set $\boldsymbol{\eta}_{\boldsymbol{k}}(t) \equiv \boldsymbol{\eta}_{\boldsymbol{k}}^{(\theta_0)}(t)$, because the properties are the same. Our equation in the rotated coordinate frame becomes

$$\dot{\boldsymbol{z}}_{\boldsymbol{k}} + \underline{\boldsymbol{\Gamma}}_{\boldsymbol{k}}^{(\theta_0)}\cdot\boldsymbol{z}_{\boldsymbol{k}} = \underline{\boldsymbol{D}}^{(\theta_0)}\cdot\boldsymbol{\eta}_{\boldsymbol{k}}(t), \tag{4.25}$$

where

$$\begin{aligned} \underline{\boldsymbol{D}}^{(\theta_0)} &= \underline{\boldsymbol{R}}(-\theta_0)\cdot\underline{\boldsymbol{D}}^{(xy)}\cdot\underline{\boldsymbol{R}}(\theta_0) \\ &= \begin{pmatrix} \sqrt{2D_r} & 0 & 0 \\ 0 & \sqrt{2D_r} & 0 \\ 0 & \xi\sqrt{2D_r} & \sqrt{2D_\theta} \end{pmatrix} \end{aligned} \tag{4.26}$$

and

$$\begin{aligned}\underline{\boldsymbol{\Gamma}}_{\boldsymbol{k}}^{(\theta_0)} &= \underline{\boldsymbol{R}}(-\theta_0)\cdot\underline{\boldsymbol{\Gamma}}_{\boldsymbol{k}}^{(xy)}\cdot\underline{\boldsymbol{R}}(\theta_0)\\ &= \begin{pmatrix} A_{\boldsymbol{k}}+B_{\boldsymbol{k}} & C_{\boldsymbol{k}} & 0\\ C_{\boldsymbol{k}} & A_{\boldsymbol{k}}-B_{\boldsymbol{k}} & -\alpha\\ \xi C_{\boldsymbol{k}} & \xi\left(A_{\boldsymbol{k}}-B_{\boldsymbol{k}}\right) & 0\end{pmatrix}.\end{aligned} \tag{4.27}$$

In this way, we introduced the abbreviations

$$A_{\boldsymbol{k}} = \frac{M_{xx,\boldsymbol{k}}+M_{yy,\boldsymbol{k}}}{2}, \tag{4.28a}$$

$$B_{\boldsymbol{k}} = \frac{M_{xx,\boldsymbol{k}}-M_{yy,\boldsymbol{k}}}{2}\cos 2\theta_0 + M_{xy,\boldsymbol{k}}\sin 2\theta_0, \tag{4.28b}$$

$$C_{\boldsymbol{k}} = -\frac{M_{xx,\boldsymbol{k}}-M_{yy,\boldsymbol{k}}}{2}\sin 2\theta_0 + M_{xy,\boldsymbol{k}}\cos 2\theta_0. \tag{4.28c}$$

We solve Eq. (4.25) using the method of Green's functions [104]. Firstly, we perform the Fourier transformation in time, and the formal solution $\tilde{\boldsymbol{z}}_{\boldsymbol{k}}(\omega) = \mathcal{F}\left[\boldsymbol{z}_{\boldsymbol{k}}(t)\right]$ is expressed via

$$-i\omega\tilde{\boldsymbol{z}}_{\boldsymbol{k}} + \underline{\boldsymbol{\Gamma}}_{\boldsymbol{k}}^{(\theta_0)}\cdot\tilde{\boldsymbol{z}}_{\boldsymbol{k}} = \underline{\boldsymbol{D}}^{(\theta_0)}\cdot\tilde{\boldsymbol{\eta}}_{\boldsymbol{k}}(\omega) \tag{4.29}$$

as

$$\tilde{\boldsymbol{z}}_{\boldsymbol{k}}(\omega) = \left[-i\omega\underline{\boldsymbol{I}} + \underline{\boldsymbol{\Gamma}}_{\boldsymbol{k}}^{(\theta_0)}\right]^{-1}\cdot\underline{\boldsymbol{D}}^{(\theta_0)}\cdot\tilde{\boldsymbol{\eta}}_{\boldsymbol{k}}(\omega). \tag{4.30}$$

The stochastic contributions in Fourier space satisfy the relations

$$\langle\tilde{\boldsymbol{\eta}}_{\boldsymbol{k}}(\omega)\rangle = \boldsymbol{0} \tag{4.31a}$$

and

$$\langle\tilde{\eta}_{\alpha,\boldsymbol{k}}(\omega)\tilde{\eta}_{\beta,\boldsymbol{k}'}(\omega')\rangle = 2\pi N\delta_{\alpha,\beta}\delta_{\boldsymbol{k},-\boldsymbol{k}'}\delta(\omega+\omega'), \tag{4.31b}$$

$$\langle\tilde{\eta}_{\alpha,\boldsymbol{k}}(\omega)\tilde{\eta}^{*}_{\beta,\boldsymbol{k}'}(\omega')\rangle = 2\pi N\delta_{\alpha,\beta}\delta_{\boldsymbol{k},\boldsymbol{k}'}\delta(\omega-\omega') \tag{4.31c}$$

for $\alpha,\beta\in\{x,y,\theta\}$.

Next, introducing the abbreviation

$$\underline{\boldsymbol{\lambda}}_{\boldsymbol{k}}(\omega) := \left[-i\omega\underline{\boldsymbol{I}} + \underline{\boldsymbol{\Gamma}}_{\boldsymbol{k}}^{(\theta_0)}\right]^{-1}, \tag{4.32}$$

the autocorrelation matrix is defined as

$$\begin{aligned}\underline{\boldsymbol{S}}_{\boldsymbol{k},\boldsymbol{k}'}(\omega,\omega') &:= \langle\tilde{\boldsymbol{z}}_{\boldsymbol{k}}(\omega)\otimes\tilde{\boldsymbol{z}}^{*}_{\boldsymbol{k}'}(\omega')\rangle\\ &= \begin{pmatrix} \langle\tilde{u}_{\parallel,\boldsymbol{k}}(\omega)\tilde{u}^{*}_{\parallel,\boldsymbol{k}'}(\omega')\rangle & \langle\tilde{u}_{\parallel,\boldsymbol{k}}(\omega)\tilde{u}^{*}_{\perp,\boldsymbol{k}'}(\omega')\rangle & \langle\tilde{u}_{\parallel,\boldsymbol{k}}(\omega)\tilde{\theta}^{*}_{\boldsymbol{k}'}(\omega')\rangle\\ \langle\tilde{u}_{\perp,\boldsymbol{k}}(\omega)\tilde{u}^{*}_{\parallel,\boldsymbol{k}'}(\omega')\rangle & \langle\tilde{u}_{\perp,\boldsymbol{k}}(\omega)\tilde{u}^{*}_{\perp,\boldsymbol{k}'}(\omega')\rangle & \langle\tilde{u}_{\perp,\boldsymbol{k}}(\omega)\tilde{\theta}^{*}_{\boldsymbol{k}'}(\omega')\rangle\\ \langle\tilde{\theta}_{\boldsymbol{k}}(\omega)\tilde{u}^{*}_{\parallel,\boldsymbol{k}'}(\omega')\rangle & \langle\tilde{\theta}_{\boldsymbol{k}}(\omega)\tilde{u}^{*}_{\perp,\boldsymbol{k}'}(\omega')\rangle & \langle\tilde{\theta}_{\boldsymbol{k}}(\omega)\tilde{\theta}^{*}_{\boldsymbol{k}'}(\omega')\rangle\end{pmatrix}\end{aligned} \tag{4.33}$$

where $\otimes$ denotes the dyadic product. We may rewrite this expression as

$$\begin{aligned}\tilde{\underline{\boldsymbol{S}}}_{\boldsymbol{k},\boldsymbol{k}'}(\omega,\omega') &= \langle\tilde{\boldsymbol{z}}_{\boldsymbol{k}}(\omega)\otimes\tilde{\boldsymbol{z}}^{*}_{\boldsymbol{k}'}(\omega')\rangle\\ &= \langle\tilde{\boldsymbol{z}}_{\boldsymbol{k}}(\omega)\otimes\tilde{\boldsymbol{z}}_{-\boldsymbol{k}'}(-\omega')\rangle\\ &= 2\pi N\underline{\boldsymbol{S}}_{\boldsymbol{k}}(\omega)\,\delta_{\boldsymbol{k},\boldsymbol{k}'}\,\delta(\omega-\omega'),\end{aligned} \tag{4.34}$$

where in the last step we introduced the matrix of equal-frequency and equal-wavevector fluctuation spectra $\underline{\boldsymbol{S}}_{\boldsymbol{k}}(\omega)$ with components

$$S_{\alpha\beta,\boldsymbol{k}}(\omega) = \lambda_{\alpha\gamma,\boldsymbol{k}}(\omega) D^{(\theta_0)}_{\gamma\eta} D^{(\theta_0)T}_{\eta\zeta} \lambda^{T}_{\zeta\beta,\boldsymbol{k}}(-\omega). \tag{4.35}$$

To derive this equation, we used the relation $\underline{\boldsymbol{\lambda}}_{\boldsymbol{k}}(\omega) = \underline{\boldsymbol{\lambda}}_{-\boldsymbol{k}}(\omega)$, the formal solution Eq. (4.30), and we applied Eqs. (4.31). Explicitly, we list the components as

$$S_{\alpha\beta,\boldsymbol{k}}(\omega) = \frac{W^{(r)}_{\alpha\beta,\boldsymbol{k}}(\omega) 2D_r + W^{(\theta)}_{\alpha\beta,\boldsymbol{k}}(\omega) 2D_\theta}{(\text{denom.})}, \tag{4.36}$$

where we introduce the following abbreviations

$$\begin{aligned}(\text{denom.}) =& \omega^2 \left(\omega^2 + A_{\boldsymbol{k}}^2 + B_{\boldsymbol{k}}^2 + C_{\boldsymbol{k}}^2 + 2A_{\boldsymbol{k}}\sqrt{B_{\boldsymbol{k}}^2 + C_{\boldsymbol{k}}^2}\right)\left(\omega^2 + A_{\boldsymbol{k}}^2 + B_{\boldsymbol{k}}^2 + C_{\boldsymbol{k}}^2 - 2A_{\boldsymbol{k}}\sqrt{B_{\boldsymbol{k}}^2 + C_{\boldsymbol{k}}^2}\right) \\ &- 2\alpha\xi\omega^2 \left[(A_{\boldsymbol{k}} - B_{\boldsymbol{k}})\omega^2 + (A_{\boldsymbol{k}} + B_{\boldsymbol{k}})(A_{\boldsymbol{k}}^2 - B_{\boldsymbol{k}}^2 - C_{\boldsymbol{k}}^2)\right] \\ &+ \alpha^2\xi^2 \left[(A_{\boldsymbol{k}} - B_{\boldsymbol{k}})^2\omega^2 + \left(A_{\boldsymbol{k}}^2 - B_{\boldsymbol{k}}^2 - C_{\boldsymbol{k}}^2\right)^2\right],\end{aligned} \tag{4.37}$$

$$\begin{aligned}W^{(r)}_{\parallel\parallel,\boldsymbol{k}}(\omega) =& \omega^4 + \left((A_{\boldsymbol{k}} - B_{\boldsymbol{k}})(A_{\boldsymbol{k}} - B_{\boldsymbol{k}} - 2\alpha\xi) + C_{\boldsymbol{k}}^2\right)\omega^2 \\ &+ \alpha^2\xi^2 \left((A_{\boldsymbol{k}} - B_{\boldsymbol{k}})^2 + C_{\boldsymbol{k}}^2\right),\end{aligned} \tag{4.38a}$$

$$W^{(r)}_{\perp\perp,\boldsymbol{k}}(\omega) = \left(\alpha^2\xi^2 + \omega^2\right)\left(A_{\boldsymbol{k}}^2 + 2A_{\boldsymbol{k}}B_{\boldsymbol{k}} + B_{\boldsymbol{k}}^2 + C_{\boldsymbol{k}}^2 + \omega^2\right), \tag{4.38b}$$

$$W^{(r)}_{\theta\theta,\boldsymbol{k}}(\omega) = \xi^2\omega^2 \left[\omega^2 + (A_{\boldsymbol{k}} + B_{\boldsymbol{k}})^2 + C_{\boldsymbol{k}}^2\right], \tag{4.38c}$$

$$W^{(r)}_{\perp\parallel,\boldsymbol{k}}(\omega) = C_{\boldsymbol{k}} \left[(\alpha\xi - 2A_{\boldsymbol{k}})\omega^2 - 2\alpha^2\xi^2 A_{\boldsymbol{k}} + i\alpha^2\xi^2\omega\right], \tag{4.38d}$$

$$W^{(r)}_{\theta\parallel,\boldsymbol{k}}(\omega) = C_{\boldsymbol{k}} \left(\left(\alpha\xi^2 - 2\xi A_{\boldsymbol{k}}\right)\omega^2 + 2i\alpha A_{\boldsymbol{k}}\xi^2\omega\right), \tag{4.38e}$$

$$W^{(r)}_{\theta\perp,\boldsymbol{k}}(\omega) = \left(\xi\omega^2 - i\alpha\xi^2\omega\right)\left[\omega^2 + (A_{\boldsymbol{k}} + B_{\boldsymbol{k}})^2 + C_{\boldsymbol{k}}^2\right], \tag{4.38f}$$

$$W^{(\theta)}_{\parallel\parallel,\boldsymbol{k}}(\omega) = \alpha^2 C_{\boldsymbol{k}}^2, \tag{4.38g}$$

$$W^{(\theta)}_{\perp\perp,\boldsymbol{k}}(\omega) = \alpha^2 \left(\omega^2 + (A_{\boldsymbol{k}} + B_{\boldsymbol{k}})^2\right), \tag{4.38h}$$

$$W^{(\theta)}_{\theta\theta,\boldsymbol{k}}(\omega) = \omega^4 + 2(A_{\boldsymbol{k}}^2 + B_{\boldsymbol{k}}^2 + C_{\boldsymbol{k}}^2)\omega^2 + (A_{\boldsymbol{k}}^2 - B_{\boldsymbol{k}}^2 - C_{\boldsymbol{k}}^2)^2, \tag{4.38i}$$

$$W^{(\theta)}_{\perp\parallel,\boldsymbol{k}}(\omega) = -C_{\boldsymbol{k}}\alpha^2 \left(A_{\boldsymbol{k}} + B_{\boldsymbol{k}} - i\omega\right), \tag{4.38j}$$

$$W^{(\theta)}_{\theta\parallel,\boldsymbol{k}}(\omega) = -C_{\boldsymbol{k}}\alpha \left(A_{\boldsymbol{k}}^2 - 2iA_{\boldsymbol{k}}\omega - B_{\boldsymbol{k}}^2 - C_{\boldsymbol{k}}^2 - \omega^2\right), \tag{4.38k}$$

$$\begin{aligned}W^{(\theta)}_{\theta\perp,\boldsymbol{k}}(\omega) =& \alpha \left[\omega^2 (A_{\boldsymbol{k}} - B_{\boldsymbol{k}}) + (A_{\boldsymbol{k}} + B_{\boldsymbol{k}})\left(A_{\boldsymbol{k}}^2 - B_{\boldsymbol{k}}^2 - C_{\boldsymbol{k}}^2\right)\right] \\ &- i\alpha\omega \left[\omega^2 + (A_{\boldsymbol{k}} + B_{\boldsymbol{k}})^2 + C_{\boldsymbol{k}}^2\right],\end{aligned} \tag{4.38l}$$

noting that the matrix $\underline{\boldsymbol{W}}^{r,\theta}_{\boldsymbol{k}}$ is Hermitean: $W^{(r,\theta)}_{\beta\alpha,\boldsymbol{k}}(\omega) = W^{*(r,\theta)}_{\alpha\beta,\boldsymbol{k}}(\omega)$.

For reference, we include the results for a passive solid composed of elastically linked passive Brownian objects as well. This system does not exhibit migrating motion. Its constituents do not self-propel. Since we cannot define an angle of self-propulsion θ_i in this case, only the fluctuations of two stochastic variables $u_{x,\boldsymbol{k}}$ and $u_{y,\boldsymbol{k}}$ need to be considered. In this case, the corresponding expressions

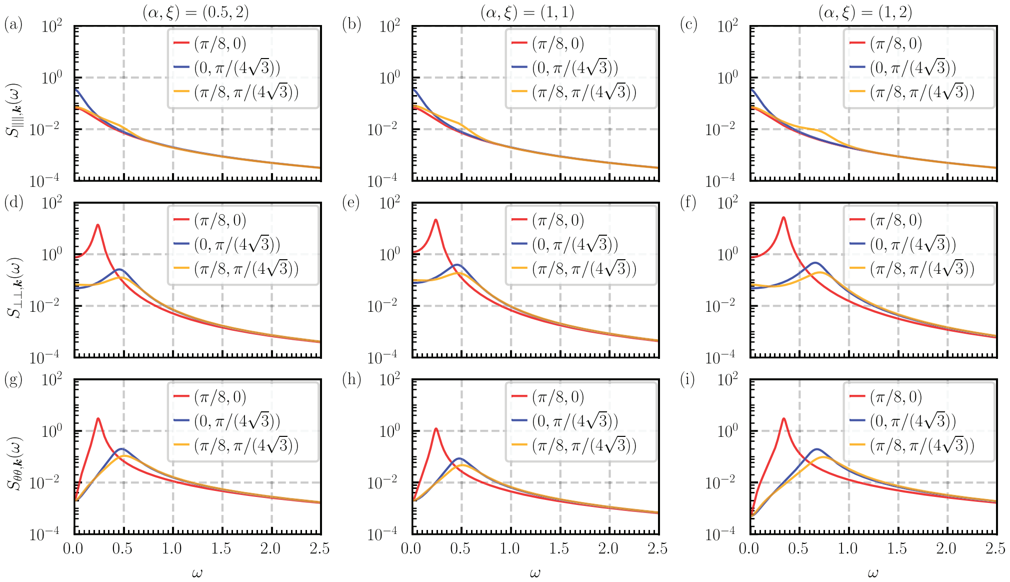

Figure 4.2: Diagonal components of the matrix of fluctuation spectra $S_{\alpha\alpha,\boldsymbol{k}}(\omega)$ as functions of angular frequency ω for some fixed wavevectors $\boldsymbol{k}=(k_x,k_y)$ as indicated by the legends and colors of the lines. From the top row, $S_{\parallel\parallel,\boldsymbol{k}}(\omega)$, $S_{\perp\perp,\boldsymbol{k}}(\omega)$, and $S_{\theta\theta,\boldsymbol{k}}(\omega)$ are plotted. Since in our case the solid migrates along the x-axis, that is, $\theta_0=0$, we here imply $S_{\parallel\parallel,\boldsymbol{k}}(\omega)=S_{xx,\boldsymbol{k}}(\omega)$ and $S_{\perp\perp,\boldsymbol{k}}(\omega)=S_{yy,\boldsymbol{k}}(\omega)$. (a), (d), and (g) Data for $(\alpha,\xi)=(0.5,2)$; (b), (e), and (h) Data for $(\alpha,\xi)=(1,1)$; and (c), (f), and (i) Data for $(\alpha,\xi)=(1,2)$.

read

$$\begin{aligned}
S_{xx,\boldsymbol{k}}(\omega)=&\frac{2D_r\left(\omega^2+M_{xy,\boldsymbol{k}}^2+M_{yy,\boldsymbol{k}}^2\right)}{\text{(denom.passive)}},\\
S_{yy,\boldsymbol{k}}(\omega)=&\frac{2D_r\left(\omega^2+M_{xx,\boldsymbol{k}}^2+M_{xy,\boldsymbol{k}}^2\right)}{\text{(denom.passive)}},\\
S_{xy,\boldsymbol{k}}(\omega)=&S_{yx,\boldsymbol{k}}(\omega)\\
=&-\frac{2D_r\left(M_{xx,\boldsymbol{k}}+M_{yy,\boldsymbol{k}}\right)M_{xy,\boldsymbol{k}}}{\text{(denom.passive)}},\\
\text{(denom.passive)}=&\omega^4+\left[M_{xx,\boldsymbol{k}}^2+2M_{xy,\boldsymbol{k}}^2+M_{yy,\boldsymbol{k}}^2\right]\omega^2\\
&+\left(M_{xx,\boldsymbol{k}}M_{yy,\boldsymbol{k}}-M_{xy,\boldsymbol{k}}^2\right)^2.
\end{aligned}\tag{4.39}$$

Both $S_{xx,\boldsymbol{k}}(\omega)$ and $S_{yy,\boldsymbol{k}}(\omega)$ are maximized at $\omega=0$ for any wavevector $\boldsymbol{k}$.

We can compare the analytical forms of these expressions for the passive solid to those of our active case in the limit of small wavenumbers k. It turns out that, in this regime, the results for the diagonal elements of the passive solid become identical to the one of the active solid along the migration direction. We obtain both from Eq. (4.36), marked by indices $\alpha=\beta=\parallel$, and from Eqs. (4.39)

$$S_{\parallel\parallel,\boldsymbol{k}}(\omega)\sim S_{xx,\boldsymbol{k}}^{\text{pas}}(\omega)\sim S_{yy,\boldsymbol{k}}^{\text{pas}}(\omega)=\frac{2D_r}{\omega^2}+O\left(k^4\right).\tag{4.40}$$

In contrast to that, the diagonal components associated with the axis perpendicular to the migration direction and with angular fluctuations obtained from Eq. (4.36) setting $\alpha=\beta=\perp,\theta$ for the active

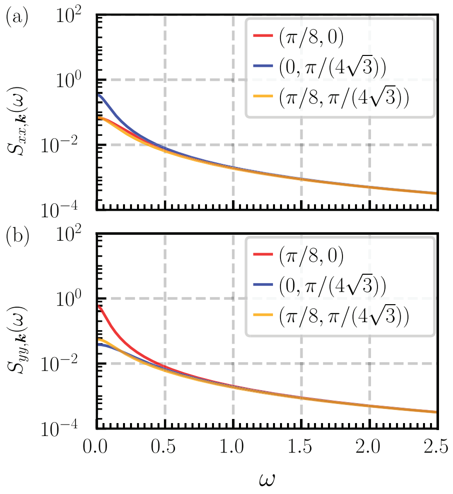

Figure 4.3: Fluctuation spectra (a) $S_{xx,\boldsymbol{k}}(\omega)$ and (b) $S_{yy,\boldsymbol{k}}(\omega)$ of a corresponding passive solid for comparison. Each colored line includes the data for a given wavevector $\boldsymbol{k} = (k_x, k_y)$ as indicated by the legend.

solid deviate and become

$$S_{\perp\perp,\boldsymbol{k}}(\omega) = \frac{2D_r\omega^2 + 2\alpha^2\left(\xi^2 D_r + D_\theta\right)}{\omega^2\left(\omega^2 - 2\alpha\xi(A_{\boldsymbol{k}} - B_{\boldsymbol{k}})\right)} + O\left(k^4\right), \tag{4.41}$$

$$S_{\theta\theta,\boldsymbol{k}}(\omega) = \frac{2\left(\xi^2 D_r + D_\theta\right)}{\omega^2 - 2\alpha\xi(A_{\boldsymbol{k}} - B_{\boldsymbol{k}})} + O\left(k^4\right), \tag{4.42}$$

where

$$\begin{aligned} A_{\boldsymbol{k}} - B_{\boldsymbol{k}} \quad = \quad & \frac{3}{8}\Big(2\left(k_x^2 + k_y^2\right) - \left(k_x^2 - k_y^2\right)\cos 2\theta_0 \\ & - 2k_x k_y \sin 2\theta_0\Big) + O\left(k^4\right). \end{aligned} \tag{4.43}$$

The additional divergences in these expressions for $S_{\perp\perp,\boldsymbol{k}}(\omega)$ and $S_{\theta\theta,\boldsymbol{k}}(\omega)$ at frequencies $\omega = \pm\sqrt{2\alpha\xi(A_{\boldsymbol{k}} - B_{\boldsymbol{k}})}$ are in line with our observations of a maximum at nonvanishing frequencies in Fig. 4.2(d)–(i). Quantitative differences and the regularization for $\omega \to 0$ in Fig. 4.2(d)–(i) can be explained by the nonvanishing wavenumbers in that case as indicated by the legends.

Hereafter we choose the direction of collective motion as $\theta_0 = 0$. For this configuration, we plot in Fig. 4.2 the diagonal components of the matrix of fluctuation spectra $S_{\alpha\alpha,\boldsymbol{k}}(\omega)$, see Eqs. (4.36), for $\alpha = \parallel, \perp, \theta$ as functions of the angular frequency ω for some fixed wavevectors $\boldsymbol{k}$. For comparison, corresponding fluctuation spectra for the situation of a passive solid, see Eqs. (4.39), are plotted in Fig. 4.3. Since $S_{\alpha\alpha,\boldsymbol{k}}(\omega)$ for $\alpha = \parallel, \perp, \theta$ are even functions in ω, we only focus on the region of $\omega \geq 0$. While the fluctuation spectra of a passive solid show maxima at $\omega = 0$ for all considered wavevectors, the ones of an active solid feature maxima at a nonvanishing ω for $\alpha = \perp, \theta$. These maxima are thus associated with the activity-induced excitability inside the active solid.

Next, we consider the nonvanishing values of angular frequencies at which the maxima of the fluctuation spectrum are located for $\alpha = \perp, \theta$. Figure 4.2 indicates that these values increase together with the strength of self-propulsion α [compare (a) and (c)] and the strength of alignment ξ [compare

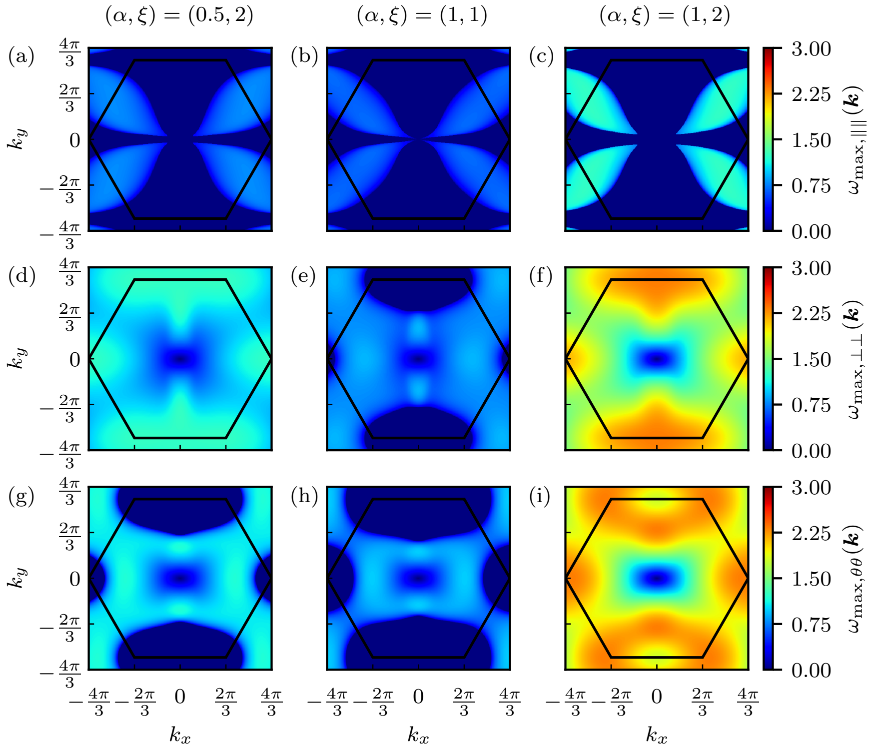

Figure 4.4: Angular frequencies $\omega_{\mathrm{max},\alpha\alpha}(\boldsymbol{k})$ that maximize the associated fluctuations $S_{\alpha\alpha,\boldsymbol{k}}(\omega)$ [$\max(S_{\alpha\alpha,\boldsymbol{k}}(\omega)) = S_{\alpha\alpha,\boldsymbol{k}}(\omega_{\mathrm{max},\alpha\alpha})$], $\alpha = \|, \perp, \theta$, as a function of the wavevector $\boldsymbol{k}$. The strengths of self-propulsion α and alignment ξ are (a), (d), and (g) $(\alpha,\xi) = (0.5, 2)$; (b), (e), and (h) $(\alpha,\xi) = (1, 1)$; (c), (f), and (i) $(\alpha,\xi) = (1, 2)$. We here set the angle of unperturbed collective migration to $\theta_0 = 0$. Dark hexagonal lines indicate the first Brillouin zone.

(b) and (c)].

Regarding the spatial dependence and anisotropy of the fluctuation spectra, we infer from Figs. 4.2 and 4.3 that both active and passive systems feature larger maximal values for $S_{\|\|,\boldsymbol{k}}(\omega)$ along the k_y-direction than along the k_x-direction. For $S_{\perp\perp,\boldsymbol{k}}(\omega)$, it is the other way around. Thus, we infer that fluctuations in displacements are enhanced along the directions perpendicular to the wavevector. $S_{\theta\theta,\boldsymbol{k}}(\omega)$ behaves similarly to $S_{\perp\perp,\boldsymbol{k}}(\omega)$ in terms of the spatial anisotropy. In our equations of motion, Eqs. (4.8) and (4.9), angular deviations are induced by perpendicular displacements $u_{\perp,\boldsymbol{k}}$.

For further reference, we denote the angular frequency at the maximum of each diagonal component $S_{\alpha\alpha,\boldsymbol{k}}(\omega)$ as $\omega_{\mathrm{max},\alpha\alpha}(\boldsymbol{k})$ for $\alpha = \|, \perp, \theta$. The corresponding maximal value for $\alpha = \|, \perp, \theta$ is obtained via

$$S_{\mathrm{max},\alpha\alpha}(\boldsymbol{k}) := \max\left(S_{\alpha\alpha,\boldsymbol{k}}(\omega)\right) = S\left(\omega_{\mathrm{max},\alpha\alpha}(\boldsymbol{k})\right). \tag{4.44}$$

$\omega_{\mathrm{max},\alpha\alpha}(\boldsymbol{k})$ and $S_{\mathrm{max},\alpha\alpha}(\boldsymbol{k})$ are plotted in Figs. 4.4 and 4.5, respectively.

According to Fig. 4.4, $\omega_{\mathrm{max},\alpha\alpha}(\boldsymbol{k})$ increases from $\boldsymbol{k} = \boldsymbol{0}$ anisotropically within the k_x-k_y-plane. In fact, the considered situation is not isotropic because of the set direction of collective migration and the discrete elastic interactions introduced by the springs. For elevated wavenumbers, we observe in Fig. 4.4 maxima of $\omega_{\mathrm{max},\theta\theta}(\boldsymbol{k})$ along each direction of $\boldsymbol{k}$. The positions of these maxima shift

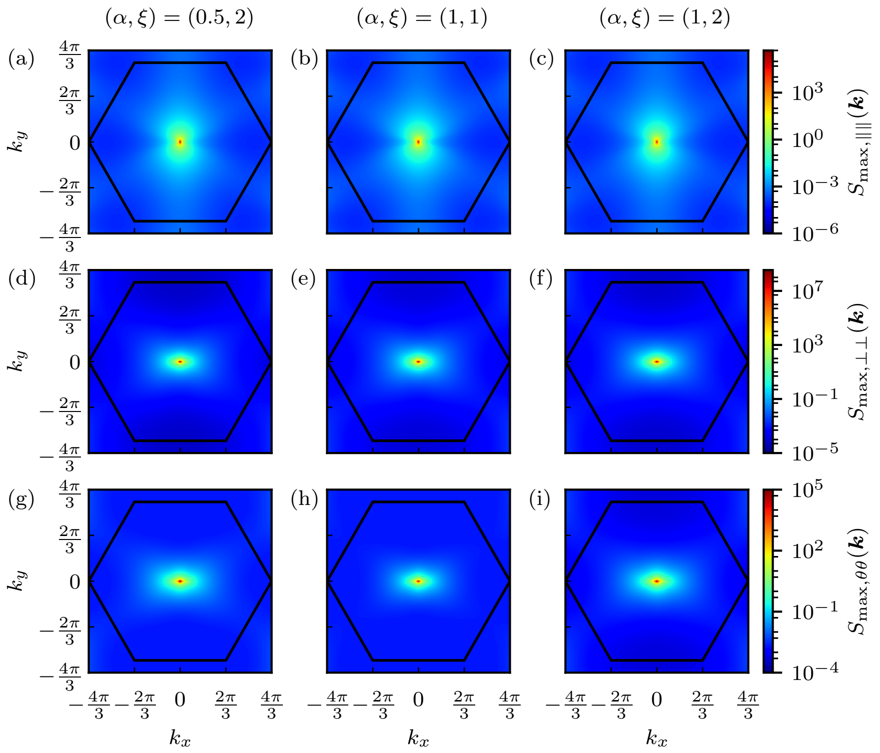

Figure 4.5: Maximum values of the fluctuation spectra $S_{\max,\alpha\alpha}(\boldsymbol{k})$ for $\alpha = \|, \perp, \theta$ as a function of the wavevector $\boldsymbol{k}$. The illustration is analogous to the one in Fig. 4.4; see the caption there for details. Again, dark hexagonal lines indicate the first Brillouin zone.

toward higher wavenumbers as α [compare (a) and (c)] or ξ [compare (b) and (c)] increase. Interestingly, therefore, fluctuations of finite nonvanishing angular frequency show maxima in the considered overdamped systems where classical phonons do not appear by construction. Thus, in contrast to the corresponding passive case, a significant fraction of fluctuations propagates through the system with characteristic nonvanishing angular frequencies.

Finally, we focus on the dependence of the maxima of the fluctuation spectra on the wavevector $\boldsymbol{k}$; see Fig. 4.5. The magnitudes in the spectra show maxima at zero wavenumber and then rapidly decay, suggesting that the fluctuations in this system mainly feature long-wavelength components. In both active and passive systems, $\omega_{\max,\alpha\alpha}(\boldsymbol{k} = \boldsymbol{0}) = 0$ is due to the presence of Goldstone modes; see Fig. 4.4. In fact, the mode $\boldsymbol{k} = \boldsymbol{0}$ does not imply any elastic deformation of the springs and thus there is no restoring force.

4.3 Rate of entropy production

We characterize the collective excitation with respect to the energy dissipation as in Ref. [89]. The rate of entropy production [92, 105, 106] is defined as

$$\dot{s} = \lim_{T\to\infty} \frac{1}{T} \left\langle \ln \frac{\mathcal{P}(T)}{\mathcal{P}_r(T)} \right\rangle, \tag{4.45}$$

where $\langle \cdots \rangle$ is the ensemble average. P and P_r are the forward and backward trajectories, respectively, scaling as

$$\begin{aligned} \mathcal{P}(T) &\sim \mathrm{e}^{-\mathcal{A}(T)}, \\ \mathcal{P}_r(T) &\sim \mathrm{e}^{-\mathcal{A}_r(T)}, \end{aligned} \tag{4.46}$$

where $\mathcal{A}$ and $\mathcal{A}_r$ represent the forward and backward actions, respectively. They are calculated via

$$\begin{aligned} \mathcal{A}(T) =& \frac{1}{2}\sum_{\boldsymbol{k}} \int_{-\infty}^{\infty} dt\, W_T(t)\, |\boldsymbol{L}_{\boldsymbol{k}}(t)|^2, \\ \mathcal{A}_r(T) =& \frac{1}{2}\sum_{\boldsymbol{k}} \int_{-\infty}^{\infty} dt\, W_T(t) \left|\boldsymbol{L}_{r,\boldsymbol{k}}(t)\right|^2. \end{aligned} \tag{4.47}$$

The summation over $\boldsymbol{k}$ implies that all modes contribute to the total entropy production. $W_T(t)$ is a rectangular window function defined by

$$W_T(t) = \begin{cases} 1 & \text{if } -T \le t \le T, \\ 0 & \text{otherwise}, \end{cases} \tag{4.48}$$

and $\boldsymbol{L}_{(r),\boldsymbol{k}}(t)$ represent the inverse Fourier transformations of $\boldsymbol{L}_{(r),\boldsymbol{k}}(\omega; T)$, obtained by solving for the stochastic contributions in the formal solutions of the equation of motion, Eq. (4.29), via

$$\boldsymbol{L}_{\boldsymbol{k}}(\omega; T) = \underline{\boldsymbol{D}}^{(\theta_0)^{-1}} \cdot \left[-i\omega\underline{\boldsymbol{I}} + \underline{\boldsymbol{\Gamma}}_{\boldsymbol{k}}^{(\theta_0)}\right] \cdot \tilde{\boldsymbol{z}}_{\boldsymbol{k}}(\omega; T), \tag{4.49}$$

$$\begin{aligned} \boldsymbol{L}_{r,\boldsymbol{k}}(\omega; T) &= \mathcal{T} \boldsymbol{L}_{\boldsymbol{k}}(\omega; T) \\ &= \underline{\boldsymbol{D}}^{(\theta_0)^{-1}} \cdot \left[i\omega\underline{\boldsymbol{I}} + \underline{\boldsymbol{\Gamma}}_{\boldsymbol{k}}^{(\theta_0)}\right] \cdot \tilde{\boldsymbol{z}}_{\boldsymbol{k}}(\omega; T). \end{aligned} \tag{4.50}$$

In the latter equation, $\mathcal{T}$ is the time-reversal operator. We here consider the dynamics within the finite time window $[-T, T]$ as indicated by the additional parameter T in the arguments of the functions.

Combining the above expressions and applying the Wiener–Khinchin theorem, see Appendix E, we find the spectral decomposition of the entropy production $\sigma(\omega, \boldsymbol{k})$, defined via

$$\dot{s} = \int_{-\infty}^{\infty} \frac{d\omega}{2\pi} \sum_{\boldsymbol{k}} \sigma_{\boldsymbol{k}}(\omega), \tag{4.51}$$

as

$$\begin{aligned} \sigma_{\boldsymbol{k}}(\omega) &= \lim_{T\to\infty} \frac{1}{2T} \left\langle \left|\boldsymbol{L}_{r,\boldsymbol{k}}(\omega; T)\right|^2 - |\boldsymbol{L}_{\boldsymbol{k}}(\omega; T)|^2 \right\rangle \\ &= \lim_{T\to\infty} \frac{1}{2T} 2i\omega \left\langle \tilde{\boldsymbol{z}}_{\boldsymbol{k}}^T(\omega; T) \cdot \left[\left(\underline{\boldsymbol{B}} \cdot \underline{\boldsymbol{\Gamma}}_{\boldsymbol{k}}^{(s)} - \underline{\boldsymbol{\Gamma}}_{\boldsymbol{k}}^{(s)} \cdot \underline{\boldsymbol{B}} \right) \right.\right. \\ &\quad \left.\left. + \left(\underline{\boldsymbol{B}} \cdot \underline{\boldsymbol{\Gamma}}_{\boldsymbol{k}}^{(a)} + \underline{\boldsymbol{\Gamma}}_{\boldsymbol{k}}^{(a)} \cdot \underline{\boldsymbol{B}} \right) \right] \cdot \tilde{\boldsymbol{z}}_{-\boldsymbol{k}}(-\omega; T) \right\rangle \\ &= -2\pi N \frac{2\omega\alpha\left(\xi^2 D_r + D_\theta\right)}{D_r D_\theta} \mathrm{Im}\left[S_{\theta\perp,\boldsymbol{k}}(\omega)\right] \\ &= 2\pi N \frac{4\alpha^2\omega^2 \left(\omega^2 + (A_{\boldsymbol{k}} + B_{\boldsymbol{k}})^2 + C_{\boldsymbol{k}}^2\right)}{(\text{denom.})} \\ &\qquad \times \frac{\left(\xi^2 D_r + D_\theta\right)^2}{D_r D_\theta}. \end{aligned} \tag{4.52}$$

We here used Eq. (4.36). Moreover, we denote by $\underline{\boldsymbol{\Gamma}}_{\boldsymbol{k}}^{(s)}$ and $\underline{\boldsymbol{\Gamma}}_{\boldsymbol{k}}^{(a)}$ the symmetric and antisymmetric parts of the matrix $\underline{\boldsymbol{\Gamma}}_{\boldsymbol{k}}^{(\theta_0)}$, respectively, defined via

$$\underline{\boldsymbol{\Gamma}}_{\boldsymbol{k}}^{(s)} = \frac{1}{2}\left(\underline{\boldsymbol{\Gamma}}_{\boldsymbol{k}}^{(\theta_0)} + \underline{\boldsymbol{\Gamma}}_{\boldsymbol{k}}^{(\theta_0)T}\right), \tag{4.53}$$

$$\underline{\boldsymbol{\Gamma}}_{\boldsymbol{k}}^{(a)} = \frac{1}{2}\left(\underline{\boldsymbol{\Gamma}}_{\boldsymbol{k}}^{(\theta_0)} - \underline{\boldsymbol{\Gamma}}_{\boldsymbol{k}}^{(\theta_0)T}\right). \tag{4.54}$$

In addition, we introduced the abbreviation

$$\begin{aligned}\underline{\boldsymbol{B}} &= \left(\underline{\boldsymbol{D}}^{(\theta_0)-1}\right)^T \cdot \underline{\boldsymbol{D}}^{(\theta_0)-1} \\ &= \begin{pmatrix} \frac{1}{2D_r} & 0 & 0 \\ 0 & \frac{1}{2D_r} + \frac{\xi^2}{2D_\theta} & -\frac{\xi}{2D_\theta} \\ 0 & -\frac{\xi}{2D_\theta} & \frac{1}{2D_\theta} \end{pmatrix}\end{aligned} \tag{4.55}$$

We plot in Fig. 4.6 the spectral entropy production $\sigma_{\boldsymbol{k}}(\omega)$ as a function of angular frequency ω for different wavevectors $\boldsymbol{k}$. Obviously, $\sigma_{\boldsymbol{k}}(\omega)$ features maxima at nonvanishing angular frequency ω similarly to the fluctuation spectra, see Fig. 4.2. We denote the angular frequency of the maximum for a given wavevector $\boldsymbol{k}$ as $\omega_{\max,\sigma}(\boldsymbol{k})$. For the considered wavevectors $\boldsymbol{k}$, the positions of $\omega_{\max,\sigma}(\boldsymbol{k})$ are closer to the ones of $\omega_{\max,\perp\perp}(\boldsymbol{k})$ and $\omega_{\max,\theta\theta}(\boldsymbol{k})$ than $\omega_{\max,\|\|}(\boldsymbol{k})$, see Fig. 4.2. These relations are conceivable because the coupling between $u_\perp$ and $\delta\theta$ significantly contributes to the spectral entropy production. The coupling becomes apparent from the emergence of $S_{\theta\perp,\boldsymbol{k}}(\omega)$ in Eq. (4.52).

For small wavenumbers, the rate of entropy production can be expanded as

$$\begin{aligned}\sigma_{\boldsymbol{k}}(\omega) =& 2\pi N \frac{4\alpha^2}{\omega^2 - 2\alpha\xi\left(A_{\boldsymbol{k}} - B_{\boldsymbol{k}}\right)} \\ &\times \frac{\left(\xi^2 D_r + D_\theta\right)^2}{D_r D_\theta}\left(1 + O\left(k^4\right)\right),\end{aligned} \tag{4.56}$$

where the wavevector dependence of $A_{\boldsymbol{k}} - B_{\boldsymbol{k}}$ is shown in Eq. (4.43). In the square brackets, the parameter ξ quantifies the strength of alignment of the direction of self-propulsion with velocity, which is affected by the forces due to the elastic springs. In this way, the corresponding term involves elasticity.

We note that $\sigma_{\boldsymbol{k}}(\omega)$ in Eq. (4.56) diverges at frequencies

$$\begin{aligned}\omega(\boldsymbol{k}) &= \pm\sqrt{2\alpha\xi\left(A_{\boldsymbol{k}} - B_{\boldsymbol{k}}\right)} \\ &= \pm\frac{1}{2}\Big[3\alpha\xi\Big(2\left(k_x^2 + k_y^2\right) \\ &\quad - \left(k_x^2 - k_y^2\right)\cos 2\theta_0 - 2k_x k_y \sin 2\theta_0\Big)\Big]^{\frac{1}{2}} \\ &\quad + O\left(k^4\right).\end{aligned} \tag{4.57}$$

This expression well reproduces the positions of the maxima in Fig. 4.6 relative to each other, that is, their order from left to right. For $\theta_0 = 0$, $\alpha = 1$, and $\xi = 2$, we find for the wavevectors listed in the legend of Fig. 4.6 for the frequencies in Eq. (4.57) ~ 0.48, 0.96, and 1.08, while the exact values are 0.34, 0.68, and 0.74, respectively. Quantitative deviations are expected in view of our approximation for small wavenumbers.

Next, the spectral entropy production $\sigma_{\boldsymbol{k}}(\omega)$ is integrated over ω, $\int \sigma_{\boldsymbol{k}}(\omega)\, d\omega/2\pi$, to obtain the

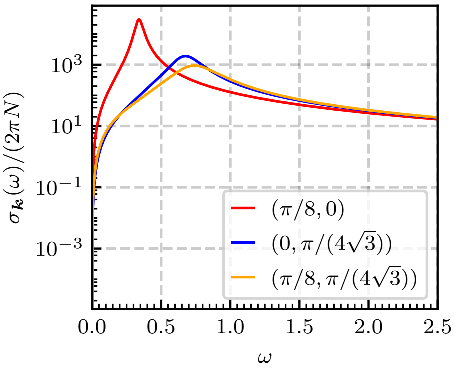

Figure 4.6: Spectral entropy production $\sigma_{\boldsymbol{k}}(\omega)$ for fixed wavevectors $\boldsymbol{k} = (k_x, k_y)$ as indicated by the color of the lines and in the legend. Again, the direction of collective migration is set along the x-direction, that is, $\theta_0 = 0$. Strengths of self-propulsion and alignment are chosen as $\alpha = 1$ and $\xi = 2$, respectively.

contributions per wavevector $\boldsymbol{k}$ to the rate of entropy production $\dot{s}$; see Eq. (4.51). It is plotted in Fig. 4.7(a), while $\omega_{\max,\sigma}(\boldsymbol{k})$ is included in Fig. 4.7(b). We infer from Fig. 4.7(a) that the integrated spectral entropy production sharply decreases as the wavenumber $|\boldsymbol{k}|$ increases. Moreover, it decays faster in the k_y-direction than in the k_x-direction. In addition, Fig. 4.7(b) shows that fluctuations of larger angular frequency ω tend to contribute more significantly to the entropy production with increasing $|\boldsymbol{k}|$.

4.4 Numerical evaluation

At the beginning of the calculation of the fluctuation spectrum in Sec. 4.2, we assumed that the fluctuations are small enough to linearize the equations and that $V = \alpha$. To check whether these assumptions are correct, we numerically implemented the original equations, Eqs. (4.6)–(4.9), in rectangular calculation boxes. The number of self-propelled objects is set to $N = 256 \times 256$. We employ a Cartesian coordinate system and denote the dimensions of the system by box lengths $L_x = 256$ and $L_y = 256 \times \sqrt{3}/2$; see Fig. 4.1. Periodic boundary conditions are imposed along all edges of the rectangular calculation box. The self-migrating objects are initially arranged on regular spring-lattice structures of perfect hexagonal symmetry. Moreover, initially, the directions $\boldsymbol{e}_i$ ($i = 1, ..., N$) of self-propulsion head towards the $+\hat{\mathbf{x}}$-direction. The equations of motion, Eqs. (4.6)–(4.9) are numerically integrated forward in time using the Euler–Maruyama method. We use a time step of $dt = 0.001$ and the parameter values in the rescaled Eqs. (4.6)–(4.9) as listed in Table 4.1.

Time evolutions of appropriate parameters are employed to check when the system has reached a steady state. For later discussion, we define the current polar order parameter

$$\boldsymbol{p}(t) = \frac{1}{N} \sum_{i=1}^{N} \boldsymbol{e}(\theta_i(t)) \tag{4.58}$$

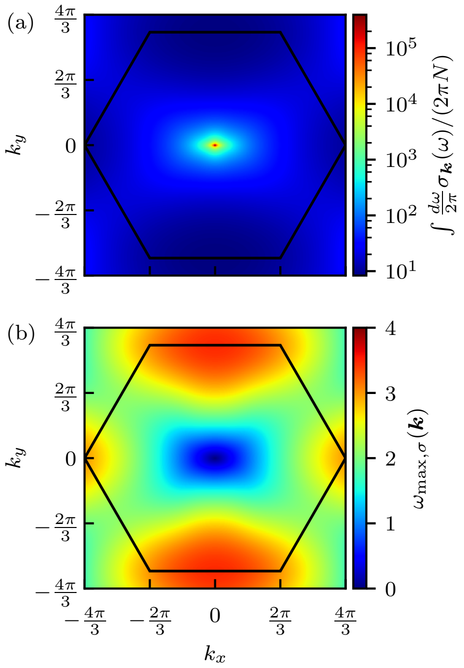

Figure 4.7: (a) Spectral entropy production $\sigma_{\boldsymbol{k}}(\omega)$ integrated over angular frequency ω to yield the contributions to the rate of entropy production $\dot{s}$; see Eq. (4.51). (b) Angular frequency $\omega_{\mathrm{max},\boldsymbol{k}}(\omega)$ that maximizes $\sigma_{\boldsymbol{k}}(\omega)$. Both are displayed in the k_x–k_y-plane of the components of the wavevector $\boldsymbol{k}$. Dark hexagonal lines indicate the first Brillouin zone.

and the current velocity of the center of mass

$$\boldsymbol{v}_c(t) = \frac{1}{N}\sum_{i=1}^{N} \boldsymbol{v}_i(t). \tag{4.59}$$

The angular orientation of $\boldsymbol{p}(t)$, denoted as $\mathrm{ang}(\boldsymbol{p}(t))$, and the relative deviation of the magnitude of $\boldsymbol{v}_c$ from the parameter α, that is, $(|\boldsymbol{v}_c(t)| - \alpha)/\alpha$, see Eqs. (4.10) and (4.15), are plotted in Fig. 4.8 as a function of time for 16 different numerical realizations. Since the numerical system is finite-sized, the fluctuations of $\mathrm{ang}(\boldsymbol{p})$ remain finite (nonzero), yet within a small range of $[-0.025, 0.025]$ within the considered time window, see Fig. 4.8(a). Moreover, in our simulations, the maximum fluctuations of the relative speeds of the centers of the mass $(|\boldsymbol{v}_c(t)| - \alpha)/\alpha$ stay within 2.5 % for all samples within the considered time window, see Fig. 4.8(b). Thus, we may conclude that they remain small enough for our approximations to be valid.

Statistically, the degree of overall orientational order and the speed of the center of the mass are then calculated as

$$\boldsymbol{P} = \langle \boldsymbol{p} \rangle_t, \tag{4.60}$$

and

$$\boldsymbol{V} = \langle \boldsymbol{v}_c \rangle_t, \tag{4.61}$$

respectively, where we use the subscript $_t$ to mark numerical ensemble and time average. These

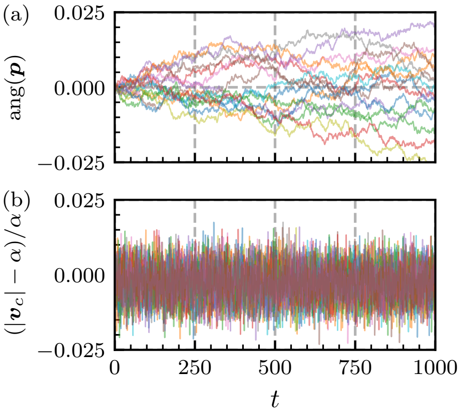

Figure 4.8: Time series of (a) the angle of the temporal polar order parameter and (b) the speed of the center of the mass. There are 16 lines obtained from different seeds for stochastic forces.

averages are taken over the 16 considered numerical realizations iterated from different seeds for the stochastic forces and over the time window $(500, 1000]$, when the system has reached a steady state. Within this time window, data are used for averaging from all integer times $t = 501, 502, ..., 1000$. The resulting values are $|\boldsymbol{P}| = 0.997315 \pm 0.000254$ and $(|\boldsymbol{V}| - \alpha)/\alpha = (-2.647 \pm 5.574) \times 10^{-3}$.

Table 4.1: Values of the rescaled parameters set in our numerical simulation.

Parameter	Description	Value(s)
N	Number of objects	256×256
α	Strength of self-propulsion	1
ξ	Strength of self-alignment	2
D_r	Translational diffusion coefficient	0.001
D_θ	Rotational diffusion coefficient	0.001

In addition, we numerically confirmed that the distribution of $\delta\theta_i(t) = \theta_i(t) - \mathrm{ang}(\boldsymbol{p}(t))$ is steady after $t = 500$. It fits well with a Gaussian curve of standard deviation 7.5×10^{-2}, indicating on average only moderate angular deviations of the individual migrating objects from the common migration direction.

Numerically, $z_i(t)$ for $i = 1, ..., N$ are obtained in the following way. We determine the reference positions that correspond to an undeformed state, in which the induced deformations of the mesh of springs vanish. From there, the positional displacements are determined. Moreover, the angular deviations are measured as deviations from the direction of $\mathrm{ang}(\boldsymbol{p}(t))$. These evaluations are performed for each instance of time t of numerical measurement.

From the prescribed time window of width $2T$, the resulting functions $S_{\alpha\alpha,\boldsymbol{k}}(\omega; T)$ corresponding to the fluctuation spectra are determined, where $\alpha \in \{\|, \perp, \theta\}$. To this end, we first transform the discrete time series of numerical measurement data $z_{\alpha,i}(t)$ confined to the time window of width $2T$ to Fourier space, yielding $\tilde{z}_{\alpha,\boldsymbol{k}}(\omega; T)$. We list the general definitions of functions of arguments $(\omega; T)$ and of the discrete Fourier series in Appendix C. The expressions $S_{\alpha\alpha,\boldsymbol{k}}(\omega; T)$ are found from ensemble averages $\langle ... \rangle_{\mathrm{ens}}$ as

$$S_{\alpha\alpha,\boldsymbol{k}}(\omega; T) = \frac{\left\langle \tilde{z}_{\alpha,\boldsymbol{k}}(\omega; T)\tilde{z}_{\alpha,-\boldsymbol{k}}(-\omega; T) \right\rangle_{\mathrm{ens}}}{2TN}. \tag{4.62}$$

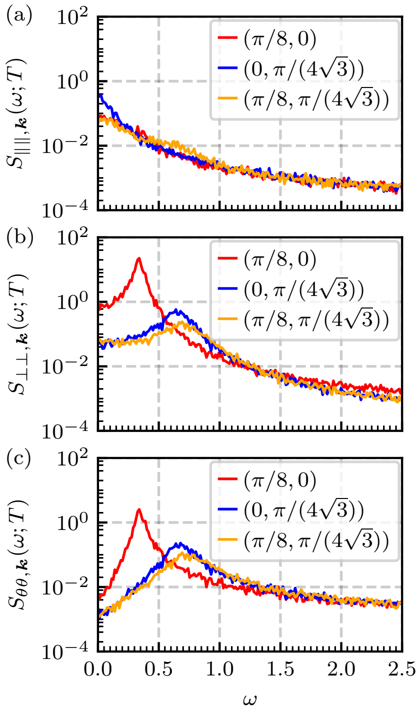

Figure 4.9: Numerically calculated fluctuation spectra $S_{\beta\beta,\boldsymbol{k}}(\omega;T)$, see Eq. (4.62), where $\beta \in \{\|, \perp, \theta\}$, for strengths of self-propulsion and angular alignment $(\alpha, \xi) = (1, 2)$. Results are obatained from numerical measurements on $N = 256 \times 256$ objects, see Table 4.1, sampling over 16 numerical realizations and a time window of width $2T = 500$. Different wavevectors $\boldsymbol{k} = (k_x, k_y)$ are selected as indicated in the legends and by the different line colors. The resulting curves match well in shape with the analytically calculated ones in Fig. 4.2(c,f,i).

Corresponding results are plotted in Fig. 4.9 and match well in shape with the analytical ones, see Fig. 4.2.

4.5 Conclusions

In summary, we analyze the excitability of the orientationally ordered, collectively moving state of active solids consisting of self-propelling objects that are elastically linked to each other. To this end, the fluctuation spectra for the elastic displacements $\boldsymbol{u}$ and deviations in the angle of self-propulsion θ are calculated from the underlying equations.

The self-correlations, apparent in the diagonal components of the matrix representing the fluctuation spectra, contain the spatiotemporal information on these excitations. In the case of passive solids, they decay monotonically as functions of frequency. In contrast to that, the fluctuation spectra for our collectively migrating active solids feature maxima for nonvanishing wavenumbers at nonvanishing frequencies.

We find that entropy production is related to the off-diagonal entries of the matrix representing the fluctuation spectra. Similarly, previous analysis demonstrates the relation between entropy production in steady states and the nonreciprocal components of the underlying dynamic equations [104]. The rate of entropy production for the considered orientationally ordered, collectively migrating active solids is maximized at vanishing wavenumber. However, for fixed nonvanishing wavenumbers, the rate of entropy production is maximized at nonvanishing frequency. Our analysis indicates that both the strength of active driving α and the strength of alignment ξ of the driving direction with the current velocity determine this effect. It further indicates that for small wavenumbers the frequency of the maximum rate of entropy production scales as $(\alpha\xi)^{1/2}$.

Summarizing, we address the effects of coupling between elastic forces on individual self-propelling objects and their direction of active migration. Some previous studies considered excitations of active solids in the absence of such migrational alignment [89, 93, 107, 108]. Moreover, we focus on excitations in the collectively moving, orientationally ordered state, while previous work addressed static correlation functions [66].

Overall, by our study, we hope to stimulate corresponding experimental realizations and observations. A challenge is certainly to produce large enough systems for quantitative matching, particularly in terms of associated HEXBUG® experiments [61, 63, 65], although we are confident that basic features can be reproduced qualitatively by focusing on the inner parts of larger collections. Generally, in theoretical studies, it is straightforward to consider continuous motion in one direction by introducing periodic boundary conditions. In contrast to that, any experimental system is of finite size. One solution could be to provide a large enough arena in experiments for directed migration over longer times. Yet, recording may be difficult. Another, more practical option might be to prepare the system on a treadmill or conveyor belt to keep it fixed in the lab frame.

The parameter values we selected in our work correspond to possible realizations in previously reported HEXBUG® experiments [61]. There, cylindrical rings contain the HEXBUGs® and are linked by elastic springs. We suggest for these experiments [61] a value for the there-introduced dimensionless control parameter of $\pi = 2$, which can be achieved by connecting the cylindrical rings containing the HEXBUGs® by springs of a spring constant around 0.86 mN/mm. The experimental study has shown for the employed components a typical time scale, on which the effects of translational inertia appear, of 0.12 s. In other words, for dynamics occurring on time scales longer than this, the effects of translational inertia are low. (Rotational inertia was neglected in the evaluation of the experiments [61].) Since our time unit obtained from the suggested spring constant is 0.25 s, we expect that the characteristics reported in our work for dimensionless frequencies $\omega \lesssim 1$ can be observed in the experiment. For example, we report in Secs. 4.2–4.4 several characteristic peaks in the corresponding frequency regime $\omega \lesssim 1$. They are observable already in our $N = 16 \times 16$ system. Furthermore, to compare our parameter values for α and ξ, we need to assume a certain length for the undeformed springs. This is indirect, because in the experiments [61] the springs are not attached to the centers of the nodes but to the rings containing the HEXBUGs®. Nevertheless, inferring from the snapshots a length of approximately $a \approx 7.5$ cm, we find $\alpha \approx 0.67$ for the strength of active driving, which is of the order of the value of $\alpha = 1$ that we mainly use for our calculations. The strength of alignment is found as $\xi \approx 3$, which is close to the value of 2 that we focus on in Figs. 4.2(c), (f), (i), and 4.6. In the experiments, this parameter could possibly be modified by additionally loading the HEXBUGs® with small asymmetric weights.

It is possible that our effects are masked by the different boundary conditions in the experiments, as our theory uses periodic boundary conditions. Our unit of length was rescaled by the length of the undeformed springs, so the distance between two HEXBUGs® in the undeformed state would correspond to our unit length. That is, in order to observe dynamic bulk phenomena away from any free boundary in the experimental system on time scales $\omega^{-1} \gtrsim 1$, let us say, $\omega^{-1} \approx 5$, we must ensure that boundary effects cannot propagate into the system on these time scales. Roughly, to be able to address inner bulk effects, the distance from the boundaries should be at least as large as the length scale of the observed effects. That is, for a focus area of $N = n \times n$ active objects, we then suggest a system of size of at least $N = (3n) \times (3n)$ active objects for observation.

Still, if direct comparison is not possible due to a dominating role of boundaries, one strategy may consist of employing programmable self-propelling robots [109]. By tracking their migration and controlling them from outside to mimic and apply mutual elastic interactions between them and adjusting their motion accordingly, periodic boundary conditions could be imposed at the same time.

In the end, we remark that our theory is based on the analysis of fluctuations around the highly orientationally ordered, collectively migrating state. Therefore, in general, we are leaving the regime of quantitative validity of our assumptions at some point when we reduce the strength of active driving. In this case, orientational fluctuations become larger and the system finally transitions towards the orientationally disordered state [20–22, 65, 66]. It is a challenging task for the future to develop a theoretical analysis that additionally covers this transitional regime.

Chapter 5

Conclusion

In this study, we examined spatiotemporal patterns and correlation structures in the condensed states of self-propelled particles with alignment interactions. We investigated correlation functions and fluctuation spectra of active matter in both liquid and solid states, using both continuum and molecular models, and using both analytical and numerical methods. The findings are summarized as follows:

- **Flow patterns and defect dynamics of active nematic liquid crystals under an electric field (Chap. 2)**
  This study on the flow patterns and defect dynamics of active nematic liquid crystals under an electric field demonstrates that an external electric field can significantly alter the system's flow structures and defect dynamics. By increasing the electric field strength, the active turbulence state transitions sequentially into the laning state and then into the uniformly aligned state. The transition point between the uniformly aligned state and the laning state can be understood through linear stability analysis. Instabilities of the uniform state always occur in the direction parallel to the electric field. Furthermore, in the intermediate state between the active turbulence state and the laning state, an oscillatory pattern involving the local generation and annihilation of vortices was observed. During the annihilation of these vortices, two pairs of topological defects are generated. The generated defects rearrange into new pairs and annihilate each other.

- **Active nematic liquid crystals under a quenched random field (Chap. 3)**
  When a random external field, simulating the heterogeneous environment inside and outside of cells, is applied, the flow and defect motion becomes slower, and above a critical field strength, the director pattern is frozen. On the other hand, the flow velocity only gradually decreases as we increase the randomness, and remains finite in the director-frozen state. This frozen state exhibits short-range orientational correlations that exponentially decay inheriting the property of passive random nematics while the flow field retains long-range logarithmic correlations. The correlation function of flow velocity is proportional to the Green function of Stokes equation. This is explained by the fact that the director field has become spatially uncorrelated, almost matching with the orientation of the random field. We studied both extensile and contractile active nematics and found no significant difference between them if the magnitude of the activity parameter is the same.

- **Collective excitations in active solids featuring alignment interactions (Chap. 4)**
  We investigated the fluctuation spectra in the uniformly aligned state of active solids characterized by alignment interactions. Unlike passive solid systems, this system reveals unique excitations arising from the interplay between activity and alignment forces. As both the activity and the strength of alignment interactions increase, the system amplifies excitations at higher wavenumbers and frequencies, indicating a direct relationship between these parameters and the vibrational dynamics. The inclusion of alignment interactions distinguishes these fluctuations from those in active solids that lack such interactions. Furthermore, we quantitatively examined the connection between these enhanced fluctuations and the rate of entropy production, providing insights into the non-equilibrium nature of the system. The coupling between fluctuations perpendicular to the migration direction and the self-propelling angle contributes to the entropy production. This analysis reveals fundamental differences from the behavior of phonon excitations observed in equilibrium solid-state systems.

These studies collectively demonstrate that active matter exhibits diverse collective motion and dynamics depending on external fields (such as electric and random fields) and internal alignment interactions. While activity serves as a means for taking the system into a non-equilibrium state, intrinsic alignment interactions have unique effects on the dynamics. This research provides essential insights into understanding the effects of activity and alignment interaction on active matter, establishing a theoretical foundation for future applications, including comprehension of living matters and the development of bio-inspired systems.

Appendix A

Details of the linear stability analysis

The content of this appendix is adapted from Ref. [68] (Y. Kinoshita and N. Uchida, “Flow patterns and defect dynamics of active nematic liquid crystals under an electric field”, Phys. Rev. E **108**, 014605 (2023)) © (2023) American Physical Society.

The eigenvalues of the matrix $\mathcal{M}$ in Eq.(2.27) are given by

$$-\mathrm{i}\omega_{\pm}^{\boldsymbol{k}} = \frac{1}{2}\left[-\left(\frac{k^2}{\mathrm{Re}} + \frac{D}{\gamma S_0}\right)\right.$$
$$\left.\pm\sqrt{\left(\frac{k^2}{\mathrm{Re}} - \frac{D}{\gamma S_0}\right)^2 + 2k^2 S_0(\lambda c+1)\left[-(\lambda c+1)D + \alpha c\right]}\right]. \tag{A1}$$

where we introduced the abbreviation $c = \cos 2\phi$. The linear growth rate $\mathrm{Im}\,\omega_{+}^{\boldsymbol{k}}$ is positive if and only if

$$\alpha c(\lambda c+1) > \left[(\lambda c+1)^2 + \frac{2}{\gamma S_0^2 \mathrm{Re}}\right]\left(\varepsilon_a E^2 + 2KS_0k^2\right). \tag{A2}$$

where we recalled $D = \varepsilon_a E^2 + 2KS_0k^2$. It is easily seen that the condition is most easily satisfied in the long-wavelength limit ($k \to 0$). To examine the ϕ-dependence, we rewrite (A2) as

$$\alpha f(c) - D g(c) > 0, \tag{A3}$$

$$f(c) = c(\lambda c+1), \tag{A4}$$

$$g(c) = (\lambda c+1)^2 + B, \tag{A5}$$

$$B = \frac{2}{\gamma S_0^2 \mathrm{Re}}. \tag{A6}$$

Since $\alpha > 0$ by assumption and $D > 0$, $g(c) > 0$, the condition (A3) is satisfied if and only if $f(c) > 0$ and

$$\frac{\alpha}{D} > h(c) \equiv \frac{g(c)}{f(c)}. \tag{A7}$$

Since we also assume $0 < \lambda < 1$, the condition $f(c) > 0$ is equivalent to $c > 0$. To find the minimum of $h(c)$, we use

$$h'(c) = -\frac{1+B}{c^2} + \frac{B}{(c+1/\lambda)^2}. \tag{A8}$$

We see that $h(c)$ is a motonotically decreasing function in the range $0 < c \leq 1$. Therefore, the stability threshold α_c is determined by substituting $k = 0$ and $\phi = 0$ into (A2), which gives Eq.(2.28).

Appendix B

Angle distribution for sinusoidal director undulation

The content of this appendix is adapted from Ref. [68] (Y. Kinoshita and N. Uchida, “Flow patterns and defect dynamics of active nematic liquid crystals under an electric field”, Phys. Rev. E **108**, 014605 (2023)) © (2023) American Physical Society.

Here we compute the distribution function $f(\theta)$ of the director angle for the sinusoidal profile $\theta(x) = \theta_0 \sin kx$. Without loss of generality, we consider the distribution in the range $-\pi/(2k) \leq x \leq \pi/(2k)$, where $\theta(x)$ is monotonically increasing with $-\theta_0 \leq \theta \leq \theta_0$ and there is one-to-one correspondence between θ and x. The probability to find the angle in the infinitesimal range $[\theta, \theta + d\theta]$ is given by $f(\theta)d\theta = dx/(\pi/k)$, where $dx = d\theta/\theta'(x)$ is the corresponding range of the x-coordinate. Therefore, we obtain

$$f(\theta) = \frac{k}{\pi}\frac{dx}{d\theta} = \frac{1}{\pi\theta_0 \cos kx} = \frac{1}{\pi\sqrt{\theta_0^2 - \theta^2}} \tag{B1}$$

for $|\theta| \leq \theta_0$. Note that $f(\theta)$ is trivially zero for $|\theta| > \theta_0$.

Appendix C

Fourier transformation

The content of this appendix is adapted from [86] (Y. Kinoshita, N. Uchida, and A. M. Menzel, “Collective excitations in active solids featuring alignment interactions”, The Journal of Chemical Physics 162, 054906 (2025)), with the permission of AIP Publishing. © (2025) AIP Publishing.

In this appendix, we list the conventions that we use to perform our Fourier transformations.

C.1 Fourier transformation in time

The Fourier transformation of the function $\boldsymbol{f} = \boldsymbol{f}(t)$ in time is defined in the form

$$\tilde{\boldsymbol{f}}(\omega) := \mathcal{F}\{\boldsymbol{f}\}(\omega) = \int_{-\infty}^{\infty} dt \boldsymbol{f}(t) \mathrm{e}^{i\omega t}, \tag{C.1a}$$

and its inverse via

$$\boldsymbol{f}(t) = \mathcal{F}^{-1}\{\tilde{\boldsymbol{f}}\}(t) = \frac{1}{2\pi} \int_{-\infty}^{\infty} d\omega \tilde{\boldsymbol{f}}(\omega) \mathrm{e}^{-i\omega t}. \tag{C.1b}$$

For our purpose, we further define the Fourier transformation of $\boldsymbol{f}(t)$ confined to the time window $[-T, T]$ as

$$\tilde{\boldsymbol{f}}(\omega; T) := \mathcal{F}\{W_T(t)\boldsymbol{f}\}(\omega) = \int_{-\infty}^{\infty} dt\, W_T(t) \boldsymbol{f}(t) \mathrm{e}^{i\omega t}, \tag{C.2}$$

where $W_T(t)$ is given by

$$W_T(t) = \begin{cases} 1 & \text{if} -T \le t \le T, \\ 0 & \text{otherwise.} \end{cases} \tag{C.3}$$

In the discrete case of a time series of measurement data $\{a_m\} = a_0, ..., a_{n-1}$, sampled at n equally distanced instances in time as indexed by $m \in \{0, 1, ..., n-1\}$, the Fourier series is written in the form

$$\tilde{a}_k := \sum_{m=0}^{n-1} a_m \mathrm{e}^{2\pi i \frac{mk}{n}} \tag{C.4a}$$

for $k = 0, ..., n-1$. Similarly, its inverse results via

$$a_m = \frac{1}{n} \sum_{k=0}^{n-1} \tilde{a}_k \mathrm{e}^{-2\pi i \frac{mk}{n}} \tag{C.4b}$$

for $m = 0, ..., n-1$.

C.2 Fourier series in space

When introducing the discrete Fourier series, two possibilities come into our mind that both have their justification. First, when assuming periodic boundary conditions in a rectangular calculation box, we may use the discrete wavevectors defined by standing waves within the calculation box. Second, we may work with the discrete lattice vectors determined by the hexagonal lattice in its undeformed state. In the following, we adopt the latter point of view.

The arbitrary lattice points are expressed in terms of a linear combination of two unit lattice vectors,

$$\boldsymbol{R} = m_1 \boldsymbol{a}_1 + m_2 \boldsymbol{a}_2 \ , \tag{C.5}$$

where $m_1 = 1, ..., N_1$ and $m_2 = 1, ..., N_2$. We choose

$$\boldsymbol{a}_1 = (1,0)^T \ , \ \boldsymbol{a}_2 = \left(\frac{1}{2}, \frac{\sqrt{3}}{2}\right)^T \ .$$

Our inverse unit lattice vectors are defined as

$$\begin{aligned} \boldsymbol{b}_1 =& 2\pi \frac{\boldsymbol{a}_2 \times \boldsymbol{a}_3}{\boldsymbol{a}_1 \cdot (\boldsymbol{a}_2 \times \boldsymbol{a}_3)} = 2\pi \left(1, -\frac{1}{\sqrt{3}}\right)^T , & \text{(C.6)} \\ \boldsymbol{b}_2 =& 2\pi \frac{\boldsymbol{a}_3 \times \boldsymbol{a}_1}{\boldsymbol{a}_2 \cdot (\boldsymbol{a}_3 \times \boldsymbol{a}_1)} = 2\pi \left(0, \frac{2}{\sqrt{3}}\right)^T , & \text{(C.7)} \end{aligned}$$

where for the ease of derivation we considered an additional third dimension introducing $\boldsymbol{a}_3 = (0,0,1)^T$.

The arbitrary inverse lattice points are expressed via

$$\boldsymbol{G} = \frac{n_1}{N_1} \boldsymbol{b}_1 + \frac{n_2}{N_2} \boldsymbol{b}_2, \tag{C.8}$$

$n_1 = 1, ..., N_1$ and $n_2 = 1, ..., N_2$. Then, the discrete Fourier transformation of $f(m_1, m_2)$ is defined as

$$\begin{aligned} \tilde{f}(n_1, n_2) :=& \mathcal{F}\left[f(m_1, m_2)\right] \\ =& \sum_{m_1=1}^{N_1} \sum_{m_2=1}^{N_2} \mathrm{e}^{-i\boldsymbol{R}\cdot\boldsymbol{G}} f(m_1, m_2) \\ =& \sum_{m_1=1}^{N_1} \sum_{m_2=1}^{N_2} \mathrm{e}^{-i\left(\frac{m_1 n_1}{N_1} \boldsymbol{a}_1 \cdot \boldsymbol{b}_1 + \frac{m_2 n_2}{N_2} \boldsymbol{a}_2 \cdot \boldsymbol{b}_2\right)} \\ & \qquad \times f(m_1, m_2) \\ =& \sum_{m_1=1}^{N_1} \sum_{m_2=1}^{N_2} \mathrm{e}^{-2\pi i\left(\frac{m_1 n_1}{N_1} + \frac{m_2 n_2}{N_2}\right)} f(m_1, m_2), \end{aligned} \tag{C.9}$$

and its inverse as

$$\begin{aligned} f(m_1,m_2) =& \mathcal{F}^{-1}\left[\tilde{f}(n_1,n_2)\right] \\ =& \frac{\sum_{n_1=1}^{N_1}\sum_{n_2=1}^{N_2}}{N_1N_2}\mathrm{e}^{i\boldsymbol{R}\cdot\boldsymbol{G}}\tilde{f}(n_1,n_2) \\ =& \frac{\sum_{n_1=1}^{N_1}\sum_{n_2=1}^{N_2}}{N_1N_2}\mathrm{e}^{i\left(\frac{m_1n_1}{N_1}\boldsymbol{a}_1\cdot\boldsymbol{b}_1+\frac{m_2n_2}{N_2}\boldsymbol{a}_2\cdot\boldsymbol{b}_2\right)} \\ & \times\tilde{f}(n_1,n_2) \\ =& \frac{\sum_{n_1=1}^{N_1}\sum_{n_2=1}^{N_2}}{N_1N_2}\mathrm{e}^{2\pi i\left(\frac{m_1n_1}{N_1}+\frac{m_2n_2}{N_2}\right)}\tilde{f}(n_1,n_2). \end{aligned} \tag{C.10}$$

A convenient relation is given by

$$\begin{aligned} & \frac{\sum_{m_1=1}^{N_1}\sum_{m_2=1}^{N_2}}{N_1N_2}\mathrm{e}^{-2\pi i\left(\frac{m_1(n_1-n_1')}{N_1}+\frac{m_2(n_2-n_2')}{N_2}\right)} \\ & = \delta_{n_1,n_1'}\delta_{n_2,n_2'}, \end{aligned} \tag{C.11}$$

where δ represents the Kronecker delta.

In a slight variation of notation, we express the Fourier series, here for the displacements $\boldsymbol{u}_i$ ($i = 1, ..., N$), as

$$\boldsymbol{u}_{\boldsymbol{k}} = \sum_{i=1}^{N}\mathrm{e}^{-\mathrm{i}\boldsymbol{k}\cdot\boldsymbol{x}_i^{(0)}}\boldsymbol{u}_i, \tag{C.12}$$

where $\boldsymbol{x}_i^{(0)}$ is the position vector of the i th object in the undeformed state of the lattice. Its inverse follows as

$$\boldsymbol{u}_i = \frac{1}{N}\sum_{\boldsymbol{k}}\mathrm{e}^{\mathrm{i}\boldsymbol{k}\cdot\boldsymbol{x}_i^{(0)}}\boldsymbol{u}_{\boldsymbol{k}}, \tag{C.13}$$

where the summation runs over the wavevectors $\boldsymbol{k}$.

A convenient relation is given by

$$\delta_{\boldsymbol{k},\boldsymbol{k}'} = \frac{1}{N}\sum_{i=1}^{N}\mathrm{e}^{-i(\boldsymbol{k}-\boldsymbol{k}')\cdot\boldsymbol{x}_i^{(0)}}, \tag{C.14}$$

where δ represents the Kronecker delta.

Appendix D

Definition and derivation of the elasticity matrix in Fourier space

The content of this appendix is adapted from [86] (Y. Kinoshita, N. Uchida, and A. M. Menzel, “Collective excitations in active solids featuring alignment interactions”, The Journal of Chemical Physics 162, 054906 (2025)), with the permission of AIP Publishing. © (2025) AIP Publishing.

The elastic force acting on the object i is

$$\boldsymbol{F}_i = -\sum_{j\in(i,j)} \underline{\boldsymbol{M}}_{ij}\cdot\boldsymbol{u}_{ij}, \tag{D.1}$$

where

$$\underline{\boldsymbol{M}}_{ij} = \begin{pmatrix} \left(x_{ij}^{(0)}\right)^2 & x_{ij}^{(0)}y_{ij}^{(0)} \\ x_{ij}^{(0)}y_{ij}^{(0)} & \left(y_{ij}^{(0)}\right)^2 . \end{pmatrix}, \tag{D.2}$$

see Eqs. (4.13) and (4.14). Multiplying Eq. (D.1) by the factor $\mathrm{e}^{-i\boldsymbol{k}\cdot\boldsymbol{x}_i^{(0)}}$ and summing over $i = 1, ..., N$, we obtain the Fourier transformed expression of $\boldsymbol{F}_i$,

$$\begin{aligned}
\boldsymbol{F}_{\boldsymbol{k}} &= -\sum_{i=1}^{N}\sum_{j\in(i,j)} \mathrm{e}^{-i\boldsymbol{k}\cdot\boldsymbol{x}_i^{(0)}}\underline{\boldsymbol{M}}_{ij}\cdot\boldsymbol{u}_{ij} \\
&= -\sum_{i=1}^{N}\sum_{j\in(i,j)} \mathrm{e}^{-i\boldsymbol{k}\cdot\boldsymbol{x}_i^{(0)}}\underline{\boldsymbol{M}}_{ij}\cdot\left[\frac{1}{N}\sum_{\boldsymbol{k}_1}\mathrm{e}^{i\boldsymbol{k}_1\cdot\boldsymbol{x}_i^{(0)}}\boldsymbol{u}_{\boldsymbol{k}_1}\right. \\
&\qquad\qquad \left.-\frac{1}{N}\sum_{\boldsymbol{k}_2}\mathrm{e}^{i\boldsymbol{k}_2\cdot\boldsymbol{x}_j^{(0)}}\boldsymbol{u}_{\boldsymbol{k}_2}\right] \\
&= -\sum_{\boldsymbol{k}_1}\sum_{i=1}^{N}\sum_{j\in(i,j)}\underline{\boldsymbol{M}}_{ij}\cdot\frac{1}{N}\mathrm{e}^{-i(\boldsymbol{k}-\boldsymbol{k}_1)\cdot\boldsymbol{x}_i^{(0)}} \\
&\qquad\quad \times\left[1-\mathrm{e}^{-i\boldsymbol{k}_1\cdot\left(\boldsymbol{x}_i^{(0)}-\boldsymbol{x}_j^{(0)}\right)}\right]\boldsymbol{u}_{\boldsymbol{k}_1} \\
&= -\sum_{\boldsymbol{k}_1}\sum_{\boldsymbol{x}_{ij}^{(0)}\in\{\mathrm{N.N.}\}}\underline{\boldsymbol{M}}_{ij}\cdot\delta_{\boldsymbol{k},\boldsymbol{k}_1}\left[1-\mathrm{e}^{-i\boldsymbol{k}_1\cdot\boldsymbol{x}_{ij}^{(0)}}\right]\boldsymbol{u}_{\boldsymbol{k}_1} \\
&= -\sum_{\boldsymbol{x}_{ij}^{(0)}\in\{\mathrm{N.N.}\}}\underline{\boldsymbol{M}}_{ij}\cdot\left[1-\mathrm{e}^{-i\boldsymbol{k}\cdot\boldsymbol{x}_{ij}^{(0)}}\right]\boldsymbol{u}_{\boldsymbol{k}} \\
&=: -\underline{\boldsymbol{M}}_{\boldsymbol{k}}\cdot\boldsymbol{u}_{\boldsymbol{k}} .
\end{aligned} \tag{D.3}$$

We denote the set of all lattice vectors connecting nearest-neighboring objects in the undeformed

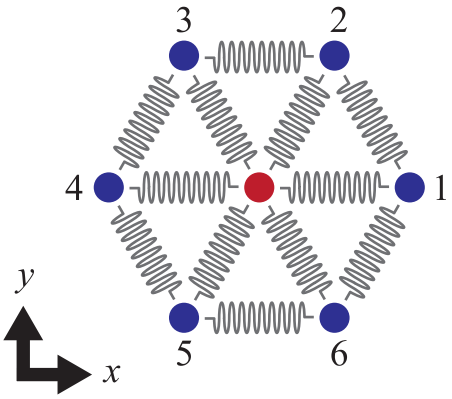

Figure D.1: Hexagonal lattice structure around one centered object (red) in the undeformed ground state of the lattice, together with the orientation of our two-dimensional Cartesian coordinate system. There are six nearest-neighboring objects (blue) surrounding the centered object. The situation is identical for each object in the undeformed hexagonal structure.

ground state by {N.N.}. In the fourth equality, we switch to the sum over all $\boldsymbol{x}_{ij}^{(0)} = \boldsymbol{x}_i^{(0)} - \boldsymbol{x}_j^{(0)} \in \{\text{N.N.}\}$. This is possible because both $\underline{\boldsymbol{M}}_{ij}$ and the exponent only depend on these relative distance vectors. Moreover, since $\boldsymbol{x}_{ij}^{(0)} = \boldsymbol{x}_i^{(0)} - \boldsymbol{x}_j^{(0)}$ refer to the relative distance vectors of the lattice in the undeformed state between nearest neighbors, they are identical for all lattice points, see also Fig. D.1. Therefore, the sum over $\boldsymbol{x}_{ij}^{(0)} \in \{\text{N.N.}\}$ can be decoupled from the sum over i. The resulting expression for $\underline{\boldsymbol{M}}_{\boldsymbol{k}}$ is the one entering Eq. (4.21).

Appendix E

Wiener–Khinchin theorem

The content of this appendix is adapted from [86] (Y. Kinoshita, N. Uchida, and A. M. Menzel, “Collective excitations in active solids featuring alignment interactions”, The Journal of Chemical Physics 162, 054906 (2025)), with the permission of AIP Publishing. © (2025) AIP Publishing.

First, we define the function $C_{\alpha\beta}(\tau;T)$ based on the real-valued stochastic variable $x_\alpha(t)$ via

$$C_{\alpha\beta}(\tau;T) = \frac{1}{2T}\int_{-\infty}^{\infty} dt\ \langle W_T(t+\tau)x_\alpha(t+\tau)W_T(t)x_\beta(t)\rangle\,, \tag{E.1}$$

where $W_T(t)$ is a rectangular window function defined in Appendix C. Moreover, we define the function $S_{\alpha\beta}(\omega;T)$ as

$$S_{\alpha\beta}(\omega;T) = \frac{1}{2T}\langle\tilde{x}_\alpha(\omega;T)\tilde{x}^*_\beta(\omega;T)\rangle\,. \tag{E.2}$$

Here, $\tilde{x}_\alpha(\omega;T)$ is the quantity obtained from $x_\alpha(t)$ via Fourier transformation in time. In fact, it can be demonstrated that $C_{\alpha\beta}(\tau;T)$ and $S_{\alpha\beta}(\omega;T)$ are connected to each other through Fourier transformations via

$$S_{\alpha\beta}(\omega;T) = \int_{-\infty}^{\infty} d\tau\, C_{\alpha\beta}(\tau;T)\mathrm{e}^{i\omega\tau}, \tag{E.3}$$

$$C_{\alpha\beta}(\tau;T) = \frac{1}{2\pi}\int_{-\infty}^{\infty} d\omega\, S_{\alpha\beta}(\omega;T)\mathrm{e}^{-i\omega\tau}. \tag{E.4}$$

Finally, in the limit of $T\to\infty$, the function $S_{\alpha\beta}(\omega;T)$ becomes the fluctuation spectrum $S_{\alpha\beta}(\omega)$, while $C_{\alpha\beta}(\omega;T)$ turns into the time correlation function $C_{\alpha\beta}(\tau)$. Therefore, these two functions satisfy

$$S_{\alpha\beta}(\omega) = \int_{-\infty}^{\infty} d\tau\, C_{\alpha\beta}(\tau)\mathrm{e}^{i\omega\tau}, \tag{E.5}$$

$$C_{\alpha\beta}(\tau) = \frac{1}{2\pi}\int_{-\infty}^{\infty} d\omega\, S_{\alpha\beta}(\omega)\mathrm{e}^{-i\omega\tau}. \tag{E.6}$$

These relations are expressed by the Wiener–Khinchin theorem [110].

References

[1] T. Vicsek and A. Zafeiris, “Collective motion”, Phys. Rep. **517**, 71–140 (2012).

[2] S. Ramaswamy, “The Mechanics and Statistics of Active Matter”, Annu. Rev. Condens. Matter Phys. **1**, 323–345 (2010).

[3] M. C. Marchetti, J. F. Joanny, S. Ramaswamy, T. B. Liverpool, J. Prost, M. Rao, and R. A. Simha, “Hydrodynamics of soft active matter”, Rev. Mod. Phys. **85**, 1143–1189 (2013).

[4] S. Ramaswamy, “Active matter”, J. Stat. Mech.: Theory Exp. **2017**, 054002 (2017).

[5] P. Romanczuk, M. Bär, W. Ebeling, B. Lindner, and L. Schimansky-Geier, “Active Brownian particles”, Eur. Phys. J. Spec. Top. **202**, 1–162 (2012).

[6] A. Cavagna and I. Giardina, “Bird Flocks as Condensed Matter”, Annu. Rev. Condens. Matter Phys. **5**, 183–207 (2014).

[7] U. Lopez, J. Gautrais, I. D. Couzin, and G. Theraulaz, “From behavioural analyses to models of collective motion in fish schools”, Interface Focus **2**, 693–707 (2012).

[8] T. B. Saw, A. Doostmohammadi, V. Nier, L. Kocgozlu, S. Thampi, Y. Toyama, P. Marcq, C. T. Lim, J. M. Yeomans, and B. Ladoux, “Topological defects in epithelia govern cell death and extrusion”, Nature **544**, 212–216 (2017).

[9] K. Kawaguchi, R. Kageyama, and M. Sano, “Topological defects control collective dynamics in neural progenitor cell cultures”, Nature **545**, 327–331 (2017).

[10] G. Duclos, C. Erlenkämper, J.-F. Joanny, and P. Silberzan, “Topological defects in confined populations of spindle-shaped cells”, Nat. Phys. **13**, 58–62 (2017).

[11] G. Duclos, C. Blanch-Mercader, V. Yashunsky, G. Salbreux, J.-F. Joanny, J. Prost, and P. Silberzan, “Spontaneous shear flow in confined cellular nematics”, Nat. Phys. **14**, 728–732 (2018).

[12] D. T. Tambe, C. Corey Hardin, T. E. Angelini, K. Rajendran, C. Y. Park, X. Serra-Picamal, E. H. Zhou, M. H. Zaman, J. P. Butler, D. A. Weitz, J. J. Fredberg, and X. Trepat, “Collective cell guidance by cooperative intercellular forces”, Nature Materials **10**, 469–475 (2011).

[13] M. A. A. Grant, B. Wacław, R. J. Allen, and P. Cicuta, “The role of mechanical forces in the planar-to-bulk transition in growing *Escherichia coli* microcolonies”, J. R. Soc. Interface **11**, 20140400 (2014).

[14] D. P. Lloyd and R. J. Allen, “Competition for space during bacterial colonization of a surface”, J. R. Soc. Interface **12**, 20150608 (2015).

[15] C. Bechinger, R. Di Leonardo, H. Löwen, C. Reichhardt, G. Volpe, and G. Volpe, “Active particles in complex and crowded environments”, Rev. Mod. Phys. **88**, 045006 (2016).

[16] D. Mandal, K. Klymko, and M. R. DeWeese, “Entropy Production and Fluctuation Theorems for Active Matter”, Phys. Rev. Lett. **119**, 258001 (2017).

[17] A. Doostmohammadi, J. Ignés-Mullol, J. M. Yeomans, and F. Sagués, “Active nematics”, Nat. Commun. **9**, 3246 (2018).

[18] A. Czirók, H. E. Stanley, and T. Vicsek, “Spontaneously ordered motion of self-propelled particles”, J. Phys. A: Math. Gen. **30**, 1375 (1997).

[19] H. Chaté, “Dry Aligning Dilute Active Matter”, Annu. Rev. Condens. Matter Phys. **11**, 189–212 (2020).

[20] E. Ferrante, A. E. Turgut, M. Dorigo, and C. Huepe, “Collective motion dynamics of active solids and active crystals”, New J. Phys. **15**, 095011 (2013).

[21] E. Ferrante, A. E. Turgut, M. Dorigo, and C. Huepe, “Elasticity-Based Mechanism for the Collective Motion of Self-Propelled Particles with Springlike Interactions: A Model System for Natural and Artificial Swarms”, Phys. Rev. Lett. **111**, 268302 (2013).

[22] T. Vicsek, A. Czirók, E. Ben-Jacob, I. Cohen, and O. Shochet, “Novel Type of Phase Transition in a System of Self-Driven Particles”, Phys. Rev. Lett. **75**, 1226–1229 (1995).

[23] F. Ginelli, “The Physics of the Vicsek model”, Eur. Phys. J. Spec. Top. **225**, 2099–2117 (2016).

[24] N. D. Mermin and H. Wagner, “Absence of Ferromagnetism or Antiferromagnetism in One- or Two-Dimensional Isotropic Heisenberg Models”, Phys. Rev. Lett. **17**, 1133–1136 (1966).

[25] G. Grégoire and H. Chaté, “Onset of Collective and Cohesive Motion”, Phys. Rev. Lett. **92**, 025702 (2004).

[26] H. Chaté, F. Ginelli, G. Grégoire, and F. Raynaud, “Collective motion of self-propelled particles interacting without cohesion”, Phys. Rev. E **77**, 046113 (2008).

[27] F. Ginelli, F. Peruani, M. Bär, and H. Chaté, “Large-Scale Collective Properties of Self-Propelled Rods”, Phys. Rev. Lett. **104**, 184502 (2010).

[28] H. Chaté, F. Ginelli, and R. Montagne, “Simple Model for Active Nematics: Quasi-Long-Range Order and Giant Fluctuations”, Phys. Rev. Lett. **96**, 180602 (2006).

[29] S. Ngo, A. Peshkov, I. S. Aranson, E. Bertin, F. Ginelli, and H. Chaté, “Large-Scale Chaos and Fluctuations in Active Nematics”, Phys. Rev. Lett. **113**, 038302 (2014).

[30] P. G. de Gennes and J. Prost, *The Physics of Liquid Crystals* (Oxford University Press, 1993).

[31] S. Chandrasekhar, *Liquid Crystals* (Cambridge University Press, 1992).

[32] M. Doi and S. F. Edwards, *The Theory of Polymer Dynamics*, International Series of Monographs on Physics (Clarendon Press, Oxford, 1988).

[33] 折原 宏, 液晶の物理 (内田老鶴圃, 2004).

[34] P. D. Olmsted, “Perspectives on shear banding in complex fluids”, Rheol. Acta **47**, 283–300 (2008).

[35] P. D. Olmsted and P. Goldbart, “Theory of the nonequilibrium phase transition for nematic liquid crystals under shear flow”, Phys. Rev. A **41**, 4578–4581 (1990).

[36] A. Doostmohammadi, S. P. Thampi, and J. M. Yeomans, “Defect-Mediated Morphologies in Growing Cell Colonies”, Phys. Rev. Lett. **117**, 048102 (2016).

[37] S. J. DeCamp, G. S. Redner, A. Baskaran, M. F. Hagan, and Z. Dogic, “Orientational order of motile defects in active nematics”, Nat. Mater. **14**, 1110–1115 (2015).

[38] T. Sanchez, D. T. N. Chen, S. J. DeCamp, M. Heymann, and Z. Dogic, “Spontaneous motion in hierarchically assembled active matter”, Nature **491**, 431–434 (2012).

[39] R. Aditi Simha and S. Ramaswamy, “Hydrodynamic Fluctuations and Instabilities in Ordered Suspensions of Self-Propelled Particles”, Phys. Rev. Lett. **89**, 058101 (2002).

[40] C. Blanch-Mercader, V. Yashunsky, S. Garcia, G. Duclos, L. Giomi, and P. Silberzan, “Turbulent Dynamics of Epithelial Cell Cultures”, Phys. Rev. Lett. **120**, 208101 (2018).

[41] S. A. Edwards and J. M. Yeomans, “Spontaneous flow states in active nematics: A unified picture”, Europhys. Lett. **85**, 18008 (2009).

[42] S. P. Thampi, R. Golestanian, and J. M. Yeomans, “Instabilities and topological defects in active nematics”, Europhys. Lett. **105**, 18001 (2014).

[43] L. Giomi, M. J. Bowick, X. Ma, and M. C. Marchetti, “Defect Annihilation and Proliferation in Active Nematics”, Phys. Rev. Lett. **110**, 228101 (2013).

[44] L. Giomi, M. J. Bowick, P. Mishra, R. Sknepnek, and M. Cristina Marchetti, “Defect dynamics in active nematics”, Philos. Trans. R. Soc. A: Math. Phys. Eng. Sci. **372**, 20130365 (2014).

[45] Ž. Krajnik, Ž. Kos, and M. Ravnik, “Spectral energy analysis of bulk three-dimensional active nematic turbulence”, Soft Matter **16**, 9059–9068 (2020).

[46] B. Martínez-Prat, R. Alert, F. Meng, J. Ignés-Mullol, J.-F. ç. Joanny, J. Casademunt, R. Golestanian, and F. Sagués, “Scaling Regimes of Active Turbulence with External Dissipation”, Phys. Rev. X **11**, 031065 (2021).

[47] L. Giomi, “Geometry and Topology of Turbulence in Active Nematics”, Phys. Rev. X **5**, 031003 (2015).

[48] R. Alert, J. Casademunt, and J.-F. Joanny, “Active Turbulence”, Annu. Rev. Condens. Matter Phys. **13**, 143–170 (2022).

[49] C. Rorai, F. Toschi, and I. Pagonabarraga, “Active nematic flows confined in a two-dimensional channel with hybrid alignment at the walls: A unified picture”, Phys. Rev. Fluids **6**, 113302 (2021).

[50] T. N. Shendruk, A. Doostmohammadi, K. Thijssen, and J. M. Yeomans, “Dancing disclinations in confined active nematics”, Soft Matter **13**, 3853–3862 (2017).

[51] E. J. Hemingway, P. Mishra, M. C. Marchetti, and S. M. Fielding, “Correlation lengths in hydrodynamic models of active nematics”, Soft Matter **12**, 7943–7952 (2016).

[52] S. P. Thampi, R. Golestanian, and J. M. Yeomans, “Active nematic materials with substrate friction”, Phys. Rev. E **90**, 062307 (2014).

[53] K. Thijssen, L. Metselaar, J. M. Yeomans, and A. Doostmohammadi, “Active nematics with anisotropic friction: the decisive role of the flow aligning parameter”, Soft Matter **16**, 2065–2074 (2020).

[54] R. C. V. Coelho, N. A. M. Araújo, and M. M. Telo da Gama, “Propagation of active nematic–isotropic interfaces on substrates”, Soft Matter **16**, 4256–4266 (2020).

[55] P. Srivastava, P. Mishra, and M. C. Marchetti, “Negative stiffness and modulated states in active nematics”, Soft Matter **12**, 8214–8225 (2016).

[56] A. Doostmohammadi, M. F. Adamer, S. P. Thampi, and J. M. Yeomans, “Stabilization of active matter by flow-vortex lattices and defect ordering”, Nat. Commun. **7**, 10557 (2016).

[57] D. J. G. Pearce, “Activity Driven Orientational Order in Active Nematic Liquid Crystals on an Anisotropic Substrate”, Phys. Rev. Lett. **122**, 227801 (2019).

[58] K. Thijssen, D. A. Khaladj, S. A. Aghvami, M. A. Gharbi, S. Fraden, J. M. Yeomans, L. S. Hirst, and T. N. Shendruk, “Submersed micropatterned structures control active nematic flow, topology, and concentration”, Proc. Natl. Acad. Sci. U. S. A. **118**, e2106038118 (2021).

[59] L. Giomi, L. Mahadevan, B. Chakraborty, and M. F. Hagan, “Banding, excitability and chaos in active nematic suspensions”, Nonlinearity **25**, 2245 (2012).

[60] P. Guillamat, J. Ignés-Mullol, and F. Sagués, “Control of active liquid crystals with a magnetic field”, Proc. Natl. Acad. Sci. U. S. A. **113**, 5498–5502 (2016).

[61] P. Baconnier, D. Shohat, C. H. López, C. Coulais, V. Démery, G. Düring, and O. Dauchot, “Selective and collective actuation in active solids”, Nat. Phys. **18**, 1234–1239 (2022).

[62] O. Dauchot and V. Démery, “Dynamics of a Self-Propelled Particle in a Harmonic Trap”, Phys. Rev. Lett. **122**, 068002 (2019).

[63] P. Baconnier, D. Shohat, and O. Dauchot, “Discontinuous Tension-Controlled Transition between Collective Actuations in Active Solids”, Phys. Rev. Lett. **130**, 028201 (2023).

[64] P. Baconnier, V. Démery, and O. Dauchot, “Noise-induced collective actuation in active solids”, Phys. Rev. E **109**, 024606 (2024).

[65] C. Hernández-López, P. Baconnier, C. Coulais, O. Dauchot, and G. Düring, “Model of Active Solids: Rigid Body Motion and Shape-Changing Mechanisms”, Phys. Rev. Lett. **132**, 238303 (2024).

[66] C. Huang, L. Chen, and X. Xing, “Alignment destabilizes crystal order in active systems”, Phys. Rev. E **104**, 064605 (2021).

[67] L. Caprini, U. M. B. Marconi, C. Maggi, M. Paoluzzi, and A. Puglisi, “Hidden velocity ordering in dense suspensions of self-propelled disks”, Phys. Rev. Res. **2**, 023321 (2020).

[68] Y. Kinoshita and N. Uchida, “Flow patterns and defect dynamics of active nematic liquid crystals under an electric field”, Phys. Rev. E **108**, 014605 (2023).

[69] R. Ramalho, H. Soares, and L. Melo, “Microtubule behavior under strong electromagnetic fields”, Mater. Sci. Eng. C **27**, 1207–1210 (2007).

[70] M. G. L. van den Heuvel, M. P. de Graaff, and C. Dekker, “Molecular Sorting by Electrical Steering of Microtubules in Kinesin-Coated Channels”, Science **312**, 910–914 (2006).

[71] T. Kim, M.-T. Kao, E. F. Hasselbrink, and E. Meyhöfer, “Active Alignment of Microtubules with Electric Fields”, Nano Lett. **7**, 211–217 (2007).

[72] N. Isozaki, S. Ando, T. Nakahara, H. Shintaku, H. Kotera, E. Meyhöfer, and R. Yokokawa, “Control of microtubule trajectory within an electric field by altering surface charge density”, Sci. Rep. **5**, 7669 (2015).

[73] I. Minoura and E. Muto, “Dielectric Measurement of Individual Microtubules Using the Electroorientation Method”, Biophys. J. **90**, 3739–3748 (2006).

[74] R. Green, J. Toner, and V. Vitelli, “Geometry of thresholdless active flow in nematic microfluidics”, Phys. Rev. Fluids **2**, 104201 (2017).

[75] Y. Kinoshita and N. Uchida, “Active nematic liquid crystals under a quenched random field”, arXiv:2404.08524.

[76] F. Vafa and L. Mahadevan, “Active Nematic Defects and Epithelial Morphogenesis”, Phys. Rev. Lett. **129**, 098102 (2022).

[77] J. Rønning, M. C. Marchetti, and L. Angheluta, “Defect self-propulsion in active nematic films with spatially varying activity”, R. Soc. Open Sci. Science **10**, 221229 (2023).

[78] A. Partovifard, J. Grawitter, and H. Stark, “Controlling active turbulence by activity patterns”, Soft Matter **20**, 1800–1814 (2024).

[79] R. Assante, D. Corbett, D. Marenduzzo, and A. Morozov, “Active turbulence and spontaneous phase separation in inhomogeneous extensile active gels”, Soft Matter **19**, 189–198 (2023).

[80] G. Thrivikraman, A. Jagiełło, V. K. Lai, S. L. Johnson, M. Keating, A. Nelson, B. Schultz, C. M. Wang, A. J. Levine, E. L. Botvinick, and R. T. Tranquillo, “Cell contact guidance via sensing anisotropy of network mechanical resistance”, Proc. Natl. Acad. Sci. U. S. A. **118**, e2024942118 (2021).

[81] L. J. Couvrette, K. L. A. Walker, T. V. Bui, and A. E. Pelling, “Plant Cellulose as a Substrate for 3D Neural Stem Cell Culture”, Bioengineering **10**, `10.3390/bioengineering10111309` (2023).

[82] A. S. Mikhailov and R. Kapral, “Hydrodynamic collective effects of active protein machines in solution and lipid bilayers”, Proc. Natl. Acad. Sci. U. S. A. **112**, E3639–E3644 (2015).

[83] Y.-K. Yu, P. L. Taylor, and E. M. Terentjev, “Exponential Decay of Correlations in a Model for Strongly Disordered 2D Nematic Elastomers”, Phys. Rev. Lett. **81**, 128–131 (1998).

[84] S. Kumar and S. Mishra, “Active nematics with quenched disorder”, Phys. Rev. E **102**, 052609 (2020).

[85] S. Kumar and S. Mishra, “Active nematic gel with quenched disorder”, Phys. Rev. E **106**, 044603 (2022).

[86] Y. Kinoshita, N. Uchida, and A. M. Menzel, “Collective excitations in active solids featuring alignment interactions”, J. Chem. Phys. **162**, 054906 (2025).

[87] K.-D. N. T. Lam, M. Schindler, and O. Dauchot, “Self-propelled hard disks: implicit alignment and transition to collective motion”, New J. Phys. **17**, 113056 (2015).

[88] L. Caprini and U. Marini Bettolo Marconi, “Spatial velocity correlations in inertial systems of active Brownian particles”, Soft Matter **17**, 4109–4121 (2021).

[89] L. Caprini, U. Marini Bettolo Marconi, A. Puglisi, and H. Löwen, “Entropons as collective excitations in active solids”, J. Chem. Phys. **159**, 041102 (2023).

[90] C. A. Weber, C. Bock, and E. Frey, “Defect-Mediated Phase Transitions in Active Soft Matter”, Phys. Rev. Lett. **112**, 168301 (2014).

[91] Q. Yang, M. Jiang, F. Picano, and L. Zhu, “Shaping active matter from crystalline solids to active turbulence”, Nat. Commun. **15**, 2874 (2024).

[92] U. Seifert, “Stochastic thermodynamics, fluctuation theorems and molecular machines”, Rep. Prog. Phys. **75**, 126001 (2012).

[93] U. M. B. Marconi, H. Löwen, and L. Caprini, “Active fluctuations in the harmonic chain: phonons, entropons and velocity correlations”, Mol. Phys. **122**, e2407009 (2024).

[94] A. Baskaran and M. C. Marchetti, “Statistical mechanics and hydrodynamics of bacterial suspensions”, Proc. Natl. Acad. Sci. U. S. A. **106**, 15567–15572 (2009).

[95] G. A. Vliegenthart, A. Ravichandran, M. Ripoll, T. Auth, and G. Gompper, “Filamentous active matter: Band formation, bending, buckling, and defects”, Sci. Adv. **6**, eaaw9975 (2020).

[96] A. A. Amsden and F. H. Harlow, “A simplified MAC technique for incompressible fluid flow calculations”, J. Comput. Phys. **6**, 322–325 (1970).

[97] R. Stracke, K. Böhm, L. Wollweber, J. Tuszynski, and E. Unger, “Analysis of the migration behaviour of single microtubules in electric fields”, Biochem. Biophys. Res. Commun. **293**, 602–609 (2002).

[98] A. P. Kalra, B. B. Eakins, S. D. Patel, G. Ciniero, V. Rezania, K. Shankar, and J. A. Tuszynski, “All Wired Up: An Exploration of the Electrical Properties of Microtubules and Tubulin”, ACS Nano **14**, 16301–16320 (2020).

[99] I. Dujovne, M. van den Heuvel, Y. Shen, M. de Graaff, and C. Dekker, “Velocity Modulation of Microtubules in Electric Fields”, Nano Lett. **8**, 4217–4220 (2008).

[100] M. Uppalapati, Y.-M. Huang, T. N. Jackson, and W. O. Hancock, “Microtubule Alignment and Manipulation Using AC Electrokinetics”, Small **4**, 1371–1381 (2008).

[101] D. Havelka, I. Zhernov, M. Teplan, Z. Lánský, D. E. Chafai, and M. Cifra, “Lab-on-chip microscope platform for electro-manipulation of a dense microtubules network”, Sci. Rep. **12**, 2462 (2022).

[102] B. Dieny and B. Barbara, “XY model with weak random anisotropy in a symmetry-breaking magnetic field”, Phys. Rev. B **41**, 11549–11556 (1990).

[103] M. J. P. Gingras and D. A. Huse, “Topological defects in the random-field XY model and the pinned vortex lattice to vortex glass transition in type-II superconductors”, Phys. Rev. B **53**, 15193–15200 (1996).

[104] S. A. M. Loos and S. H. L. Klapp, “Irreversibility, heat and information flows induced by non-reciprocal interactions”, New J. Phys. **22**, 123051 (2020).

[105] R. E. Spinney and I. J. Ford, “Nonequilibrium Thermodynamics of Stochastic Systems with Odd and Even Variables”, Phys. Rev. Lett. **108**, 170603 (2012).

[106] L. Dabelow, S. Bo, and R. Eichhorn, “Irreversibility in Active Matter Systems: Fluctuation Theorem and Mutual Information”, Phys. Rev. X **9**, 021009 (2019).

[107] L. Caprini, U. M. B. Marconi, A. Puglisi, and A. Vulpiani, “The entropy production of Ornstein–Uhlenbeck active particles: a path integral method for correlations”, J. Stat. Mech.: Theory Exp. **2019**, 053203 (2019).

[108] L. Caprini, U. M. B. Marconi, and H. Löwen, “Entropy production and collective excitations of crystals out of equilibrium: The concept of entropons”, Phys. Rev. E **108**, 044603 (2023).

[109] M. Rubenstein, A. Cornejo, and R. Nagpal, “Programmable self-assembly in a thousand-robot swarm”, Science **345**, 795–799 (2014).

[110] R. Kubo, M. Toda, and N. Hashitsume, *Statistical Physics II: Nonequilibrium Statistical Mechanics* (Springer, Berlin, Heidelberg, 1998).

Work List

PUBLICATIONS

1. Yutaka Kinoshita and Nariya Uchida, “Flow patterns and defect dynamics of active nematic liquid crystals under an electric field”, Phys. Rev. E **108**, 014605 (2023).
2. Y. Kinoshita, N. Uchida, and A. M. Menzel, “Collective excitations in active solids featuring alignment interactions”, J. Chem. Phys. **162**, 054906 (2025).

PREPRINT

1. Yutaka Kinoshita and Nariya Uchida, “Active nematic liquid crystals under a quenched random field”, arXiv:2404.08524.

PRESENTATIONS

Talks

1. Yutaka Kinoshita and Nariya Uchida, “電場下のアクティブネマティック液晶の流動特性と欠陥ダイナミクス” (Original) English Translation: “Flow properties and defects’ dynamics of active nematics under electric field”, The 11th conference of Japanese Soft Matter Society, Institute of Industrial Science, University of Tokyo, 18th – 20th December 2023.
2. Yutaka Kinoshita and Nariya Uchida, “Effect of an electric field on the dynamical steady states of active nematics”, The 6th Symposium for the Core Research Clusters for Materials Science and Spintronics, and the 5th Symposium on International Joint Graduate Program in Material Science, online (CRCs) and hybrid (GP-MS), 24th – 27th October 2022.
3. Yutaka Kinoshita and Nariya Uchida, “Flow and orientational properties of active nematic liquid crystals under an electric field”, The 87th Annual Conference of the DPG and DPG Spring Meeting, Technische Universität Berlin, 17th – 22nd March 2024.
4. Yutaka Kinoshita and Nariya Uchida, “Frozen patterns of active nematic liquid crystals under a quenched random field”, JPS 79th Annual Meeting, The Physical Society of Japan, Hokkaido University, 16th – 19th September 2024.

Posters

1. Yutaka Kinoshita, Yusuke Masaki, Sumio Ishihara, “局在スピンと結合した拡張イオン性ハバード模型の光学応答” (original) English Translation: “Optical response in extended ionic Hubbard model coupled with localized spins”, JPS 76th Annual Meeting, The Physical Society of Japan, online, 12th – 15th March 2021.
2. Yutaka Kinoshita, “Effect of confinement on flow properties of active nematics”, The 5th Symposium for The Core Research Clusters for Materials Science and Spintronics, and the 4th Symposium on International Joint Graduate Program in Materials Science, online, 25th – 28th October 2021.
3. Yutaka Kinoshita and Nariya Uchida, “Effect of a quenched random field on a two-dimensional active nematics”, 4th week of Long-term Workshop on Frontiers in Non-equilibrium Physics 2024, Yukawa Institute for Theoretical Physics, Kyoto University, Japan, 22nd – 26th July 2024.

Acknowledgements

I would like to express my heartfelt gratitude to everyone who has supported and guided me throughout my research journey. Their encouragement, insights, and assistance have been indispensable in the completion of this doctoral thesis.

First and foremost, I am profoundly grateful to my three academic advisors in graduate school. Prof. Sumio Ishihara, who supported me for approximately seven months, from the time I entered the Master's program until his passing, provided invaluable guidance during my undergraduate studies and the early stages of my Master's program, laying a strong foundation for my academic growth. Prof. Nariya Uchida has offered continuous encouragement and thoughtful advice throughout my Master's and doctoral programs since I changed labs in my first year of the Master's program. Prof. Andreas Menzel has guided me since I was at Otto-von-Guericke University Magdeburg. His expertise and support played a crucial role in advancing my work.

I would also like to extend my sincere appreciation to Prof. Toshihiro Kawakatsu, Prof. Nariya Uchida, Prof. Andreas Menzel, Prof. Masayuki Imai, and Prof. Makina Saito for taking the time to review my dissertation. Their constructive feedback and insights have greatly enhanced the depth and quality of this research.

In addition, I am deeply indebted to Prof. Yusuke Masaki, currently an assistant professor at the Department of Applied Physics, Graduate School of Engineering, Tohoku University, and Prof. Atsushi Ono for their invaluable advice and unwavering support during my time in Prof. Ishihara's group. Their mentorship and encouragement have been a source of strength throughout my academic journey.

I am also grateful for the guidance and support provided by Prof. Toshihiro Kawakatsu, Prof. Takahiro Murashima, and Mr. Youhei Morii. Their expertise and insights into soft matter physics have significantly enriched the content and direction of my research.

The daily interactions and intellectual exchanges with the members of the Theoretical Condensed Matter and Statistical Physics Group at Tohoku University, as well as those in the Department Theory of Soft Matter / Biophysics at Otto-von-Guericke University Magdeburg, have been a constant source of inspiration. Their camaraderie and input have made my research life both stimulating and rewarding, leaving a lasting impact on my academic and personal growth.

I would like to express my gratitude to the International Joint Graduate Program in Materials Science for their generous financial support and for offering a unique and enriching academic curriculum. The opportunities for overseas training, in particular, allowed me to gain invaluable experiences and skills that would not have been possible in a conventional doctoral program.

Finally, I gratefully acknowledge the support provided through JST SPRING under Grant Number JPMJSP2114.

February 2025
Yutaka Kinoshita
木下 豊